

INFORMATION TO USERS

This manuscript has been reproduced from the microfilm master. UMI films the text directly from the original or copy submitted. Thus, some thesis and dissertation copies are in typewriter face, while others may be from any type of computer printer.

The quality of this reproduction is dependent upon the quality of the copy submitted. Broken or indistinct print, colored or poor quality illustrations and photographs, print bleedthrough, substandard margins, and improper alignment can adversely affect reproduction..

In the unlikely event that the author did not send UMI a complete manuscript and there are missing pages, these will be noted. Also, if unauthorized copyright material had to be removed, a note will indicate the deletion.

Oversize materials (e.g., maps, drawings, charts) are reproduced by sectioning the original, beginning at the upper left-hand corner and continuing from left to right in equal sections with small overlaps.

Photographs included in the original manuscript have been reproduced xerographically in this copy. Higher quality 6" x 9" black and white photographic prints are available for any photographs or illustrations appearing in this copy for an additional charge. Contact UMI directly to order.

ProQuest Information and Learning
300 North Zeeb Road, Ann Arbor, MI 48106-1346 USA
800-521-0600

UMI[®]

University of Alberta

**An Elliptic Inclusion with Imperfect Interface
Embedded in an Infinite Elastic Medium**

by

Hongnian Shen ©

A thesis submitted to the Faculty of Graduate Studies and Research in partial
fulfillment of the requirements for the degree of Doctor of Philosophy

Department of Mechanical Engineering

Edmonton, Alberta

Fall 2000



National Library
of Canada

Acquisitions and
Bibliographic Services

395 Wellington Street
Ottawa ON K1A 0N4
Canada

Bibliothèque nationale
du Canada

Acquisitions et
services bibliographiques

395, rue Wellington
Ottawa ON K1A 0N4
Canada

Your file Votre référence

Our file Notre référence

The author has granted a non-exclusive licence allowing the National Library of Canada to reproduce, loan, distribute or sell copies of this thesis in microform, paper or electronic formats.

The author retains ownership of the copyright in this thesis. Neither the thesis nor substantial extracts from it may be printed or otherwise reproduced without the author's permission.

L'auteur a accordé une licence non exclusive permettant à la Bibliothèque nationale du Canada de reproduire, prêter, distribuer ou vendre des copies de cette thèse sous la forme de microfiche/film, de reproduction sur papier ou sur format électronique.

L'auteur conserve la propriété du droit d'auteur qui protège cette thèse. Ni la thèse ni des extraits substantiels de celle-ci ne doivent être imprimés ou autrement reproduits sans son autorisation.

0-612-59667-2

Canada

University of Alberta

Library Release Form

Name of Author: Hongnian Shen

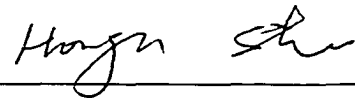
Title of Thesis: An Elliptic Inclusion with Imperfect Interface Embedded in an Infinite Elastic Medium

Degree: Doctor of Philosophy

Year this Degree Granted: 2000

Permission is hereby granted to the University of Alberta Library to reproduce single copies of this thesis and to lend or sell such copies for private, scholarly or scientific research purposes only.

The author reserves all other publication and other rights in association with the copyright in the thesis, and except as herein before provided, neither the thesis nor any substantial portion thereof may be printed or otherwise reproduced in any material form whatever without the author's prior written permission.



Engineering Mechanics & Design Laboratory
Department of Mechanical & Industrial Engineering
University of Toronto
5 King's College Road
Toronto, Ontario M5S 3G8
C A N A D A

Date: June 20, 2000

ABSTRACT

This dissertation presents a semi-analytic solution for the problem associated with an elliptic inclusion embedded within an infinite matrix with a homogeneously imperfect interface subjected to simple mechanical and thermal loadings. The interface is modeled as a spring (interphase) layer with vanishing thickness. Under the assumptions of this model the interface bonding will no longer be considered perfect and interfacial displacement discontinuities will be allowed. The role of the imperfect interface parameters on the stress field and average stress is investigated systematically. Both the inclusion and the matrix materials are considered to be homogeneous, isotropic and linearly elastic.

Three distinct studies of composites incorporating imperfect interfacial bonding under the influence of thermal and mechanical loading are presented in this dissertation. The solutions thus obtained illustrate the effectiveness of the present solution methodology.

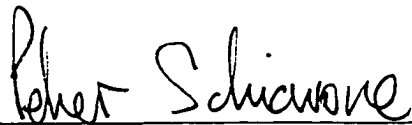
Complex variable techniques are used to obtain infinite series representations of the stresses induced within the inclusion. The results obtained demonstrate how the (non-uniform) stress field and the average stresses inside the inclusion vary with the aspect ratio of the inclusion and the parameter describing the imperfect interface. In addition, and perhaps most significantly, for different aspect ratios of the elliptic inclusion, we identify a specific value of the interface parameter which corresponds to maximum peak stress along the inclusion-matrix interface or within the elliptic inclusion. Furthermore, the results indicate that it is possible to reduce the thermal stress by inserting a reasonably thick compliant interphase layer under a thermal loading. For the first time, the present

work provides a systematic study on the combined effects of an imperfect interface with the aspect ratio of the inclusion shape. The results could be used to evaluate effective properties of composite materials incorporating non-ideal material interfaces and to design these interfaces for minimizing peak interfacial or internal stresses.

University of Alberta

Faculty of Graduate Studies and Research


The undersigned certify that they have read, and recommend to the Faculty of Graduate Studies and Research for acceptance, a thesis entitled **An Elliptic Inclusion with Imperfect Interface Embedded in an Infinite Elastic Medium** submitted by **Hongnian Shen** in partial fulfillment of the requirements for the degree of Doctor of Philosophy.



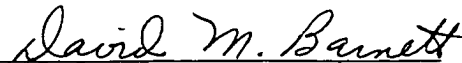
Dr. Peter Schiavone(Supervisor)



Dr. Andrew Mioduchowski(Co-Supervisor)



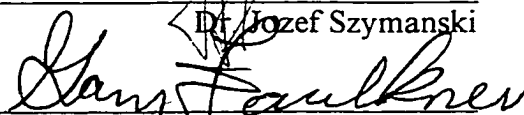
Dr. Chongqing Ru(Co- Supervisor)



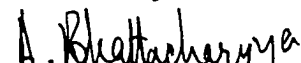
Dr. David M. Barnett



Dr. Jozef Szymanski



Dr. M Gary Faulkner



Dr. Abhijit Bhattacharyya

Date: June 19, 2000

ACKNOWLEDGMENT

The author wishes to express his most sincere and deepest gratitude to his supervisor, Dr. Peter Schiavone, and co-supervisors, Drs. Chongqing Ru and Andrew Mioduchowski, for their invaluable advice, guidance and kind understanding which made this thesis a pleasant and fruitful experience.

Last but not least, the author would like also to thank all his friends for lending a helping hand in the course of his studies. Special thanks to his wife, Qin Hong, and his son, Cheng Cheng, for their love, support and understanding which make it possible to see the completion of this work today.

TABLE OF CONTENTS

ABSTRACT

ACKNOWLEDGMENT

TABLE OF CONTENTS

LIST OF FIGURES

LIST OF SYMBOLS

CHAPTER 1: INTRODUCTION

1.1 General Background & Literature Review ----- 1

1.2 Objectives and Dissertation Overview ----- 8

CHAPTER 2: AN ELLIPTIC INCLUSION WITH IMPERFECT

INTERFACE IN ANTI-PLANE SHEAR

2.1 Introduction ----- 10

2.2 Problem Formulation ----- 12

2.3 Conformal Mapping ----- 15

2.4 General Solution ----- 16

2.5 Numerical Example and Discussion ----- 22

2.5.1 The Case of Remote Mechanical Loading ----- 22

2.5.2 Eigenstrain Problem ----- 34

2.6 Summary of Results Obtained ----- 36

CHAPTER 3: STRESS ANALYSIS OF AN ELLIPTIC INCLUSION

WITH HOMOGENEOUSLY IMPERFECT INTERFACE IN PLANE ELASTICITY

3.1 Introduction	38
3.2 Problem Formulation	39
3.3 Numerical Example and Discussion	54
3.3.1 Interfacial Stress	54
3.3.2 Average Stress Inside Inclusion	68
3.3.3 Internal Stress Distribution	72
3.3.4 Mean Stresses and Von Mises Stresses	76
3.4 Summary of Results Obtained	87

CHAPTER 4: THERMAL STRESS ANALYSIS OF AN ELLIPTIC INCLUSION

WITH A COMPLIANT INTERPHASE LAYER IN PLANE ELASTICITY

4.1 Introduction	90
4.2 Problem Formulation	92
4.3 Numerical Example and Discussion	102
4.3.1 Interfacial Stress	102
4.3.2 Internal Stress Distribution	117
4.3.3 Mean Stresses and Von Mises Stresses	121
4.3.4 Average Stress Inside Inclusion	134
4.4 Summary of Results Obtained	135

CHAPTER 5: SUMMARY AND SUGGESTIONS FOR FUTURE STUDY ----- 139

REFERENCES ----- 145

APPENDIX ----- 157

LIST OF FIGURES

<u>Figure 2.1</u> : The conformal mapping from z -plane to ξ -plane -----	15
<u>Figure 2.2</u> : Effect of the imperfect interface parameter h on the average stress ($\bar{\sigma}_{xz} / S_{0xz}$) inside the inclusion when the remote stress is S_{0xz} -----	25
<u>Figure 2.3</u> : Non-uniformity of stress along the interface when the remote stress is S_{0xz} with $a/b=3$ -----	26
<u>Figure 2.4</u> : The stress distribution along the x and y axes for remote stress S_{0xz} with $a/b=3$ -----	26
<u>Figure 2.5</u> : Effect of the imperfect interface parameter h on the average stress ($\bar{\sigma}_{xz} / S_{0xz}$) inside inclusion when the remote stress is S_{0xz} -----	27
<u>Figure 2.6</u> : Non-uniformity of stress along the interface when the remote stress is S_{0xz} with $a/b=6$ -----	28
<u>Figure 2.7</u> : The stress distribution along the x and y axes for remote stress S_{0xz} with $a/b=6$ -----	28
<u>Figure 2.8</u> : Effect of the imperfect interface parameter h on the average stress ($\bar{\sigma}_{xz} / S_{0xz}$) inside the inclusion when the remote stress is S_{0xz} -----	29
<u>Figure 2.9</u> : Non-uniformity of stress along the interface when the remote stress is S_{0xz} with $a/b=9$ -----	30
<u>Figure 2.10</u> : The stress distributions along the x and y axes for the remote stress S_{0xz} with $a/b=9$ -----	30
<u>Figure 2.11</u> : The relationship between h^* and a/b -----	32

<u>Figure 2.12</u> : The effective peak stress along the interface varies as a function of the imperfect interface parameter h when the remote stress is S_{0xz} -----	33
<u>Figure 2.13</u> : The stress distribution with $a/b=3$ for the matrix along x axis with different h when (a)remote mechanical loading S_{0xz} ; (b) eigenstrain loading -----	35
<u>Figure 3.1</u> : Conformal mapping from z -plane to ξ -plane -----	42
<u>Figure 3.2</u> : Normal and tangential stresses along the interface with $a/b=3.5$ and $h_1 = h_2 = h$ when the remote stress is S_{x0} -----	56
<u>Figure 3.3</u> : Normal and tangential stresses along the interface with $a/b = 3.5$ and $h_1 = 3h_2 = h$ when the remote stress is S_{x0} -----	56
<u>Figure 3.4</u> : Normal and tangential stresses along the interface with $a/b = 7$ and $h_1 = h_2 = h$ when the remote stress is S_{x0} -----	57
<u>Figure 3.5</u> : Normal and tangential stresses along the interface with $a/b = 7$ and $h_1 = 3h_2 = h$ when the remote stress is S_{x0} -----	57
<u>Figure 3.6</u> : Normal and tangential stresses along the interface with $a/b = 10$ and $h_1 = h_2 = h$ when the remote stress is S_{x0} -----	58
<u>Figure 3.7</u> : Normal and tangential stresses along the interface with $a/b = 10$ and $h_1 = 3h_2 = h$ when the remote stress is S_{x0} -----	58
<u>Figure 3.8</u> : Peak traction along the interface varies as a function of the interface parameter $h = h_1 = h_2$ when the remote stress is S_{x0} -----	61
<u>Figure 3.9</u> : Peak energy per unit interphase varies as a function of the imperfect interface parameter $h = h_1 = h_2$ when the remote stress is S_{x0} -----	63
<u>Figure 3.10</u> : The relationship between h^* and a/b using the resultant traction criterion when $h_1 = h_2 = h$ -----	66

<u>Figure 3.11</u> : The relationship between h^* and a/b using the interfacial energy density criterion for $h_1 = h_2 = h$ -----	67
<u>Figure 3.12</u> : Effect of the imperfect interface parameter h on the average stress $(\frac{\bar{\sigma}_{xx}}{S_{x0}})$ inside the inclusion for $h_1 = h_2 = h$ when the remote stress is S_{x0} -----	68
<u>Figure 3.13</u> : Effect of the imperfect interface parameter h on the average stress $(\frac{\bar{\sigma}_{yy}}{S_{y0}})$ inside the inclusion for $h_1 = h_2 = h$ when the remote stress is S_{y0} -----	69
<u>Figure 3.14</u> : Effect of the imperfect interface parameter h on the average stress $(\frac{\bar{\sigma}_{xy}}{S_{xy0}})$ inside the inclusion for $h_1 = h_2 = h$ when the remote stress is S_{xy0} -----	70
<u>Figure 3.15</u> : Non-uniformity of internal stresses along the interface when the remote stress is S_{x0} with $a/b=3.5$ for $h_1=h_2=h$ -----	73
<u>Figure 3.16</u> : Non-uniformity of internal stresses along the interface when the remote stress is S_{x0} with $a/b=7$ for $h_1=h_2=h$ -----	74
<u>Figure 3.17</u> : Non-uniformity of internal stresses along the interface when the remote stress is S_{x0} with $a/b=10$ for $h_1=h_2=h$ -----	75
<u>Figure 3.18</u> : The stress distribution along the x and y axes for remote stress S_{x0} with $a/b=3.5$ -----	76
<u>Figure 3.19</u> : Non-uniformity of mean stress along the interface when the remote stress is S_{x0} with $a/b=3.5$ for $h_1=h_2=h$ -----	77
<u>Figure 3.20</u> : Non-uniformity of mean stress along the interface when the remote stress is S_{x0} with $a/b=7$ for $h_1=h_2=h$ -----	78

<u>Figure 3.21</u> : Non-uniformity of mean stress along the interface when the remote stress is S_{x0} with $a/b=10$ for $h_1=h_2=h$	78
<u>Figure 3.22</u> : Non-uniformity of the von Mises stress along the interface when the remote stress is S_{x0} with $a/b=3.5$ for $h_1=h_2=h$	80
<u>Figure 3.23</u> : Non-uniformity of the von Mises stress along the interface when the remote stress is S_{x0} with $a/b=7$ for $h_1=h_2=h$	80
<u>Figure 3.24</u> : Non-uniformity of the von Mises stress along the interface when the remote stress is S_{x0} with $a/b=10$ for $h_1=h_2=h$	81
<u>Figure 3.25</u> : Non-uniformity of internal stresses along the interface when the remote stress is S_{xy0} with $a/b=3.5$ for $h_1=h_2=h$	82
<u>Figure 3.26</u> : Non-uniformity of mean stress along the interface when the remote stress is S_{xy0} with $a/b=3.5$ for $h_1=h_2=h$	83
<u>Figure 3.27</u> : Non-uniformity of the von Mises stress along the interface when the remote stress is S_{xy0} with $a/b=3.5$ for $h_1=h_2=h$	83
<u>Figure 3.28</u> : The peak mean stress along the interface varies as a function of the imperfect interface parameter h when the remote stress is S_{x0} for $h_1=h_2=h$	85
<u>Figure 3.29</u> : The relationship between h^* and a/b for $h_1=h_2=h$	86
<u>Figure 4.1</u> : Normal and tangential stresses along the interface for $a/b=3.5$ in plane strain under a uniform change in temperature for $h_1=h_2=h$	104
<u>Figure 4.2</u> : Normal and tangential stresses along the interface for $a/b=3.5$ in plane strain under a uniform change in temperature for $h_1=3h_2=h$	104
<u>Figure 4.3</u> : Normal and tangential stresses along the interface for $a/b=7$ in plane strain under a uniform change in temperature for $h_1=h_2=h$	105

Figure 4.4: Normal and tangential stresses along the interface for $a/b=7$ in plane strain under a uniform change in temperature for $h_1=3h_2=h$ -----106

Figure 4.5: Normal and tangential stresses along the interface for $a/b=10$ in plane strain under a uniform change in temperature for $h_1=h_2=h$ -----107

Figure 4.6: Normal and tangential stresses along the interface for $a/b=10$ in plane strain under a uniform change in temperature for $h_1=3h_2=h$ -----107

Figure 4.7: The peak resultant traction along the interface varies as a function of the imperfect interface parameter h in plane strain under a uniform change in temperature for $h_1=3h_2=h$ -----109

Figure 4.8: The interfacial strain energy (\bar{U}) along the interface for $a/b=3.5$ in plane strain under a uniform change in temperature for $h_1=3h_2=h$ -----111

Figure 4.9: The interfacial strain energy (\bar{U}) along the interface for $a/b=7$ in plane strain under a uniform change in temperature for $h_1=3h_2=h$ -----111

Figure 4.10: The interfacial strain energy (\bar{U}) along the interface for $a/b=10$ in plane strain under a uniform change in temperature for $h_1=3h_2=h$ -----112

Figure 4.11: The interfacial strain energy density varies as a function of the imperfect interface parameter h in plane strain under a uniform change in temperature for $h_1=3h_2=h$ -----113

Figure 4.12: The relationship between h^* and a/b using the resultant traction criterion when $h_1 = 3h_2 = h$ -----115

Figure 4.13: The relationship between h^* and a/b using the interfacial strain energy density criterion for $h_1 = 3 h_2 = h$ -----116

<u>Figure 4.14</u> : Non-uniformity of internal stresses along the interface for $a/b=3.5$ in plane strain under a uniform change in temperature for $h_1=h_2=h$	118
<u>Figure 4.15</u> : Non-uniformity of internal stresses along the interface for $a/b=7$ in plane strain under a uniform change in temperature for $h_1=h_2=h$	119
<u>Figure 4.16</u> : Non-uniformity of internal stresses along the interface for $a/b=10$ in plane strain under a uniform change in temperature for $h_1=h_2=h$	120
<u>Figure 4.17</u> : The stress distribution along the x and y axes for $a/b=3.5$ in plane strain under a uniform change in temperature for $h_1=h_2=h$	121
<u>Figure 4.18</u> : Non-uniformity of mean stresses along the interface for $a/b=3.5$ in plane strain under a uniform change in temperature for $h_1=h_2=h$	122
<u>Figure 4.19</u> : Non-uniformity of mean stresses along the interface for $a/b=7$ in plane strain under a uniform change in temperature for $h_1=h_2=h$	123
<u>Figure 4.20</u> : Non-uniformity of mean stresses along the interface for $a/b=10$ in plane strain under a uniform change in temperature for $h_1=h_2=h$	123
<u>Figure 4.21</u> : Non-uniformity of the von Mises stresses along the interface for $a/b=3.5$ in plane strain under a uniform change in temperature for $h_1=h_2=h$	124
<u>Figure 4.22</u> : Non-uniformity of the von Mises stresses along the interface for $a/b=7$ in plane strain under a uniform change in temperature for $h_1=h_2=h$	125
<u>Figure 4.23</u> : Non-uniformity of the von Mises stresses along the interface for $a/b=10$ in plane strain under a uniform change in temperature for $h_1=h_2=h$	125
<u>Figure 4.24</u> : The peak mean stress at the interface varies as a function of the imperfect interface parameter h in plane strain under a uniform change in temperature for $h_1=h_2=h$	126

Figure 4.25: The peak von_Mises stress at the interface varies as a function of the imperfect interface parameter h in plane strain under a uniform change in temperature for $h_1=h_2=h$ -----127

Figure 4.26: The critical mean stress (corresponding to h^R) at the interface varies as a function of the imperfect interface parameter h in plane strain under a uniform change in temperature for $h_1=h_2=h$ -----129

Figure 4.27: The critical von_Mises stress (corresponding to h^R) at the interface varies as a function of the imperfect interface parameter h in plane strain under a uniform change in temperature for $h_1=h_2=h$ -----129

Figure 4.28: The relationship between h^* and a/b for the mean stress' criterion -----130

Figure 4.29: The relationship between h^* and a/b for von_Mises' stress criterion ----131

Figure 4.30: The relationship between h^R and a/b for the mean stress' criterion -----132

Figure 4.31: The relationship between h^R and a/b for von_Mises' stress criterion ----133

Figure 4.32: Effect of the imperfect interface parameter h on the average stress

$(\frac{\bar{\sigma}_{xx}}{\Delta\alpha E_1 \Delta T})$ inside inclusion in plane strain under a uniform change in temperature --134

Figure 4.33: Effect of the imperfect interface parameter h on the average stress

$(\frac{\bar{\sigma}_{yy}}{\Delta\alpha E_1 \Delta T})$ inside inclusion in plane strain under a uniform change in temperature --135

LIST OF SYMBOLS

Symbol	Description & dimension
a	semi-major axis.
b	semi-minor axis.
E_1, E_2	Young's modulae, GPA .
F_x, F_x	components of resultant force.
h	imperfect interface parameter in anti-plane elasticity, PA/M .
h_1	imperfect interface parameter along normal direction in plane elasticity, PA/M .
h_2	imperfect interface parameter along tangential direction in plane elasticity, PA/M .
h^*	imperfect interface parameter corresponding to maximum peak stress or maximum peak interfacial strain energy density, PA/M .
h^R	imperfect interface parameter corresponding to perfect bonding, PA/M .
m	mapping function.
n	unit outer normal vector to path Γ .
S_1	domain occupied by the matrix.
S_2	domain occupied by the elliptic inclusion.
ΔT	uniform change in temperature, $^{\circ}C$.

u_x, u_y	displacement components in plan-strain.
U	strain energy density, PA/M .
w_1, w_2	displacements in anti-plane elasticity in the matrix and inclusion, respectively.
α_1, α_2	coefficients of thermal expansion in the matrix and inclusion, respectively, $^{\circ}C$.
Γ	an arbitrary path along the interface.
ε_{ij}	strain tensor.
μ_1, μ_2	shear moduli in the matrix and inclusion, respectively, GPA .
ν_1, ν_2	Poisson's ratios in the matrix and inclusion, respectively.
σ_{ij}	stress tensor, N/M^2 .
Φ_1, Φ_2	complex potentials in anti-plane elasticity in the matrix and inclusion, respectively.
ϕ, ψ	analytic functions in plane elasticity.
$[[\]]$	denotes the jump across Γ .

CHAPTER 1

INTRODUCTION

1.1 GENERAL BACKGROUND & LITERATURE REVIEW

Most materials and structures in engineering contain defects in the form of inclusions, cracks, and voids or second phase particles. The popular application of composite materials in recent decades has prompted researchers to investigate the elastic behavior of fibers embedded in the matrix material involving various bimaterial geometries. It is now well understood that the presence of inhomogeneities in an elastic material may result in stress intensification in their vicinities, and the local disturbances (thermal or mechanical) can induce some "weak" areas that might further cause the failure of the composite. The exact mechanism by which this process occurs is complex and often involves the interaction of different types of defects such as voids, cracks, inclusions and dislocations.

The high temperature and pressure processes used when fabricating composites may also contribute to form a region between an individual fiber and the surrounding matrix, commonly referred to as an *interphase*. This region of the material, in most cases, exhibits different mechanical properties from either side of the constituents (Brennan, 1988; Lerch et al, 1990; Sottos et al, 1992). The interphase may, sometimes, be viewed as a diffusion zone, a nucleation zone, a chemical reaction zone or a combination of any of the above. Due to its general complexity in forming, the interphase has to be

characterized at several levels for one to fully comprehend the nature of bonding developed between the bulk materials. A survey of the literature reveals that extensive research has been done in the areas of micromechanics, chemistry and material sciences on the interphase (Brennan, 1988; Kim and Bau, 1992). While a comprehensive thermomechanical characterization of the interphase is difficult, a great deal of effort has been made to physically measure and model the effects of the interphase on the local and global failure mechanisms of the composites (Brennan, 1988; Jayaraman et al, 1993a,b).

In many cases, manufacturing of composites may also require that an individual fiber be coated before being embedded in the host matrix. This may be done to enhance the bonding strength between the fiber and matrix, to remove unfavorable stress concentrations along the fiber/matrix interface region or to isolate the fiber from severe service conditions. Therefore, the interphase can be considered as a *thin interfacial layer* between an inclusion and a matrix, that can be created by coating the inclusions, or by chemical reactions during the fabrication process. This layer is often modeled as an imperfect interface of vanishing thickness across which the displacements may be discontinuous. It is well known that the interphase layer between the fiber and the matrix material affects the overall mechanical properties and the strength of the composite. Walpole (1978) has shown that even a thin coating on a fiber could have a pronounced effect on the field just outside the inclusion. Further studies have shown (Benveniste et al, 1989; Dasgupta and Sirkis, 1992; Mikata and Taya, 1985) that adjusting the fiber volume fraction and the thickness of the coating may improve the stress state at the fiber/matrix interface. It was suggested by Theocaris and Phillippidis (1985) and later expanded by Jayaraman and Reifsnider (1991) to model the interphase properties by means of a

gradient property model. This model, however, can be used only under very specific mathematical simplifications (Jayaraman et al, 1992,1993a,) which sometimes yield unrealistic results (Lu, 1993).

Many research efforts have been devoted to characterizing the complex behavior of the interphase. The following general observations are discussed in Jayaraman et al, 1992: a) the interphase is responsible for transmitting any interaction between the fiber and the matrix; b) interphasial degradation has a definite effect on the global properties and response of the composite material; and c) interphasial failure may often lead to global failure of composite materials. Given the nature of the interphase and its effect on interfacial bonding, it is important to consider the interfacial bonding stiffness together with the corresponding elastic fields. Thus, incorporating the interphase properties into the analysis not only requires complete knowledge about the interphase but also demands a more complicated model. In addition, a significant amount of research has been devoted to investigating the impact of the interphase, or coating properties (Agarwal and Bansal, 1979; Benveniste et al, 1989; Jayaraman et al, 1992; Pagano and Tandon, 1990) on the mechanical properties of the composites. Recognizing the existence of an interphase implies that the composite has to be regarded, at least, as a three-phase material. Such a consideration requires complete knowledge of the physical properties of the interphase, information which is mainly in situ, and is very difficult to measure. Therefore it is suggested that other suitable methods be developed to account for the interphase effects.

In contrast to the interphase approach outlined above, the concept of *interface* becomes a natural candidate to solve the complex problems associated with an interphase. In three-dimensional problems, an interface is defined as a two-dimensional

imaginary entity, or border, that physically separates distinct material phases such as fiber and matrix. Physically, it can be viewed as a limiting case of an interphase layer with very thin (vanishing) thickness. This imaginary boundary separates the bulk materials and, consequently, allows the material properties to be changed abruptly across the interface. As we know, the interphase is three-dimensional, but the interface is the limiting value of the interphase as its thickness tends to zero. Consequently, unless the actual bonding mechanism of the composite or the physical/chemical properties of the interphase is of concern, this model provides a much-simplified way of modeling the complex behavior of the interphase.

Although the failure of composite materials does not necessarily occur at the material interface, debonding along the interface does play an important role in various failure processes. In some instances, interfacial separation leads directly to catastrophic failure, while in other circumstances failure results from void nucleation as a result of a sequence of inclusion decohesion events (Levy, 1991; Needlerman, 1990).

Traditionally, the interface is considered as a surface across which both the displacements and the tractions are continuous. Such an interface is usually referred to as a *perfect interface* (Benveniste et al, 1989; Dokos, 1949; Dundurs and Zienkiewicz, 1964; Dundurs, 1989; Honein and Herrmann, 1990; Jasiuk et al, 1992; Jayaraman et al, 1993, Ru & Schiavone, 1996). A review of earlier research can be found in Hashin, 1983. Recent studies have shown, however, that, this model, is not suitable in the presence of an interphase layer (Achenbach and Zhu, 1989,1990). In fact, a prominent feature of certain brittle matrix composites is the presence of imperfect bonding between various constituent materials, such as the interface between fiber/interphase or interphase/matrix.

Such poor bonding has generally been considered as essential for damage tolerance or ultimate fracture resistance in the presence of strong, stiff matrix materials. The nature of the bonding is, in turn, affected by the properties of the constituents due to their influence on the stress field caused by process conditions as well as loading conditions (Dhingra and Fishman, 1986; Pagano and Tandon, 1990). To promote the understanding of the local stress fields near the inclusion/matrix interface, a more realistic model to delineate the complex interfacial characteristics needs to be established.

A critical examination of the literature dealing with the interface problem of composite materials also reveals that the vast majority of contributions are concerned with effective properties of composites when imperfections of the interface are considered (Aboudi, 1987; Benveniste, 1985; Benveniste and Miloh, 1986; Hashin, 1990; Jun and Jasiuk, 1993; Mal and Bose, 1975; Pagano and Tandon, 1990). A review of methods for finding the effective moduli for two-dimensional composites with sliding inclusions (imperfect tangential bonding) can be found in Jun and Jasiuk, 1993. Among the studies undertaken to evaluate localized elastic fields in the presence of interface imperfections, practically all results are related to the *circular* inclusion (Gao, 1995; Ru & Schiavone, 1997, Sudak et al, 1999). No systematic research and solution are available for an *elliptic* inclusion with imperfect interface, even for anti-plane shear in spite of its fundamental importance to composite mechanics. This is partially due to the mathematical difficulties encountered when formulating and analyzing the problem. The simplest imperfect interface model is the elastic spring-type interface model (Aboudi, 1987) in which the tractions are continuous, displacements are discontinuous and proportional to the tractions. The proportionality (or spring) constants characterize

the stiffness of the interface between the inclusion and the matrix. This model was first proposed by Jones and Whitter (1967) to solve a wave propagation problem across a bimaterial interface, and later was extended by a number of researchers to find the effective properties of composites containing spherical inclusions (Benveniste and Miloh, 1986; Mal and Bose, 1975). A numerical treatment of a square periodic inclusion array in an infinite matrix has been given by Achenbach and Zhu (1989). Hashin (1991b) provided an analytical solution for a spherical inclusion using this model. Hashin demonstrated that the interface imperfection could have significant effect on the stress fields in and near the inclusion. Using certain simplifications, he also showed that the material properties and thickness of the interphase layer may be related to a limited number of interfacial parameters associated with interfacial bonding. His analysis also gives a reasonable explanation for possible material overlapping across the interface.

Most of the existing analytical models are based on the assumption that the fibre-matrix interface has uniform properties e.g. that the interphase layer has uniform thickness and material properties (in this case, the interface is referred as a *homogeneously imperfect interface*). In some cases, for example, when an interface exhibits significant inhomogeneous damage it becomes necessary to consider an *inhomogeneously imperfect interface*. Therefore, recently, Ru & Schiavone, 1997 and Sudak et al, 1999, have investigated the inhomogeneous interface but only for the circular inclusion. In most cases of interest in composite mechanics, the interphase layer can be considered to be equal thickness and approximately uniform properties around the inclusion. Hence, the *homogeneously imperfect interface* model described by Hashin (1991b) provides an adequate approximation to the behavior of the actual interphase layer

between the matrix and the inclusion. Therefore, in this thesis we adopt this approach and base our analysis on the *homogeneously imperfect interface* model.

For the elliptic inclusion with a *homogeneously imperfect interface*, no systematic research and solution are available despite its importance to composite mechanics. In this case (elliptic inclusion), it is of interest to investigate the shape effect on stress fields by adjusting the aspect ratios of the elliptic inclusion.

It is well known that the single-inclusion problem is the fundamental problem in a composite (Eshelby, 1957, 1959; Hashin 1991b). For example, Eshelby considered one single inclusion and Eshelby's tensor is a famous solution in a composite. For many problems in composites such as calculation of effective (global) material properties of the composite, it is most important to obtain the average strain or stress field for the inclusion phase in the composite. We may use several different approximate procedures (for example, Dilute Approximation, Self-Consistent Scheme, Mori_Tanaka Method, etc.) to obtain the effective (global) material properties of the composite once we know the average stress and average strain field within the single-inclusion embedded within an infinite matrix. In addition, the single-inclusion model is suitable for modeling composites with fiber volume fractions up to 40% (Schmauder et al, 1992). Under this condition, the interaction among neighboring fibers and its influence on the stress fields on the overall composite system can be neglected. Therefore a single inclusion model should describe the stress and displacement fields inside and around the inclusion reliably for low or medium fiber volume content composites (Schmauder et al, 1992). More important, the single-inclusion model adopted in this analysis is a much simpler and more

practical model than other available multi-inclusion composite models (Achenbach and Zhu, 1990).

Furthermore, the single-inclusion model may be extended to the problem of thermal stress analysis. As we know, thermal mismatch induced stresses are considered as the main cause of failure in many materials and devices, such as metal-ceramic composites and passivated interconnect lines in integrated circuits (Gouldstone et al, 1998; Ru, 1998a; Ru et al 1999; Shen, 1998; Dao et al, 1997; Gleixner et al, 1997; Wu et al, 1996). Many practical problems require a systematic study of the effects of interphase layers on thermal mismatch induced stresses in inclusion/matrix systems. For example, the failure of interconnect lines due to thermal stress-induced voiding has become a major issue in the design of reliable integrated circuits (Gouldstone et al, 1998; Gleixner et al, 1997). In this case, the line is subjected to large tensile stresses upon cooling from high passivation deposition temperatures.

1.2 OBJECTIVES AND DISSERTATION OVERVIEW

The present project emphasizes an elliptic inclusion with a *homogeneously imperfect interface* condition. The objective of this research is to employ this imperfect interface model to study several fundamental problems in composites associated with a single elastic elliptic inclusion with imperfect interface embedded within an infinite matrix subjected to simple mechanical and thermal loadings. Our aim is to develop a semi-analytical solution and to study systematically the role of the imperfect interface

parameters on the corresponding stress field. Once the local stress and strain fields of the inclusion/matrix interface are determined, we can predict the possible failure mechanism of the composite structure. The knowledge of the influence of an imperfect interface on the localized elastic fields will also enable us to calculate the effective (global) material properties of the composite more accurately so that the design of such structures can be enhanced.

In the present research, complex variable techniques are used to obtain infinite series representations of the stresses which, when evaluated numerically, demonstrate how the stress field inside the inclusion varies with the aspect ratio of the ellipse and parameters describing the imperfect interface.

Three distinct studies of composites with an imperfect interfacial bonding are presented in this dissertation. They are organized as follows. Chapter 2 reports the semi-analytic solution for the problem associated with an elliptic inclusion embedded within an infinite matrix in anti-plane shear. Chapter 3 develops the analogous problem in plane elasticity. In Chapter 4, the same imperfect interface model is extended to study the problem of thermal stress analysis associated with an elliptic inclusion embedded within a compliant layer in an infinite matrix subjected to a uniform change in temperature. Chapter 5 provides some concluding remarks with some suggestions for future research.

CHAPTER 2

AN ELLIPTIC INCLUSION WITH AN IMPERFECT INTERFACE IN ANTI-PLANE SHEAR

2.1 INTRODUCTION

Problems involving elastic inclusions with imperfect bonding at the inclusion-matrix interface (imperfect interface) have received a considerable amount of attention in the literature (see, for example, Benveniste, 1984; Hashin, 1990, 1991a,b, 1992; Jasiuk & Tong, 1989; Jasiuk & Kouider, 1993; Gao, 1995 and Ru & Schiavone, 1997). Interest in these problems is motivated by the study of interface damage in composites (for example, debonding, sliding and/or cracking across an interface) and its subsequent effect on the effective properties of composites.

One of the more widely used models of an imperfect interface (see, for example, Aboudi 1987, Achenbach & Zhu 1989, Hashin 1991b, Gao 1995 and Ru & Schiavone 1997) is based on the assumption that tractions are continuous but displacements are discontinuous across the interface. More precisely, jumps in the displacement components are assumed to be proportional, in terms of 'spring-factor-type' interface parameters, to their respective interface traction components. When these interface

parameters are assumed to be uniform along the entire length of the material interface, the interface model is said to represent a *homogeneously imperfect interface*. Using this model, Hashin (1991b) examined the case of a spherical inclusion imperfectly bonded to a three-dimensional matrix. In contrast to the case of perfect bonding (see, for example, Eshelby 1957), Hashin found that, under a remote uniform stress field, the state of stress inside the inclusion is no longer uniform. The analogous result in plane elasticity has been established by Gao (1995) for a circular inclusion (see also Qu (1993a,b) for similar results concerning an elliptic inclusion with a ‘slightly weakened interface’). To the author’s knowledge, despite its importance to composite mechanics and the study of elastic inclusions with imperfect interfaces, the solution of the problem of an *elliptic inclusion with homogeneously imperfect interface* has not been recorded in the literature.

In the present chapter, we consider the problem associated with an elliptic elastic inclusion embedded within an infinite matrix in anti-plane shear when the interface is homogeneously imperfect (Shen et al, 1999a). Using complex variable techniques we obtain infinite series representations of the corresponding stresses which, when evaluated numerically, demonstrate how the (non-uniform) stress field and the average stress within the inclusion vary with the parameter describing the imperfect interface. In addition, we show that, in some cases (depending on the aspect ratio of the inclusion), interfacial stresses are found to be non-monotonic functions of the interface parameter. In these cases, it is possible to identify specific values of the interface parameter which correspond to maximum peak stress along the interface.

2.2 PROBLEM FORMULATION

Anti-plane shear deformations are one of the simplest classes of deformations that solids can undergo. In anti-plane shear (or longitudinal shear, generalized shear) of a cylindrical body, the displacement is parallel to the generators of the cylinder and is independent of the axial coordinate. Therefore, anti-plane shear, with just a single scalar axial displacement field, may be viewed as complementary to the more complicated plane strain deformation, with its two in-plane displacements. Studies in the area of elasticity anti-plane elasticity were largely motivated by the promise of relative analytic simplicity compared with plane problems since the governing equations are described by a single second-order linear or quasi-linear partial differential equation rather than the higher-order or coupled systems of partial differential equations found in theories of plane elasticity. Thus the anti-plane shear problem plays a useful role as a pilot problem, within which various aspects of solutions in solid mechanics may be examined in a particularly simple setting (Horgan, 1995 for a complete account of anti-plane elasticity).

Consider a domain in \mathcal{R}^2 , infinite in extent, containing a single internal elastic inclusion, with elastic properties different from those of the surrounding matrix. The linearly elastic materials occupying the matrix and inclusion are assumed to be homogeneous and isotropic with associated shear moduli μ_1 and μ_2 , respectively. At infinity, the prescribed deformation is that of a simple shear. We represent the matrix by the domain S_1 and assume the inclusion occupies an elliptic region S_2 . The ellipse Γ will denote the inclusion-matrix interface. In what follows, the subscripts 1 and 2 will refer to

the regions S_1 and S_2 , respectively, (x, y) is a generic point in \mathcal{H}^2 and $w(x, y)$ will denote the elastic (anti-plane) deformation at the point (x, y) .

We assume that the interface is homogeneously imperfect as described in §2.1. The interface condition in anti-plane elasticity is therefore given by (see Ru & Schiavone 1997)

$$h[w_1 - (w_2 + \omega^*)] = \mu_1 \frac{\partial w_1}{\partial n} = \mu_2 \frac{\partial w_2}{\partial n}, \quad \text{on } \Gamma, \quad (2.1)$$

where $h = \text{constant}$ is the imperfect interface parameter, n is the outward unit normal to Γ and $\omega^*(x, y)$ represents the additional displacement induced within the inclusion by a uniform eigen-strain specified below. We note that as h approaches infinity in (2.1), we must have $w_1 = w_2 + \omega^*(x, y)$ so that, in this case, (2.1) describes a perfectly bonded interface (see, for example, Ru & Schiavone 1996). Similarly, if $h = 0$, (2.1) reduces to the case of a traction-free interface which characterizes the complete debonding of the inclusion from the matrix. Consequently, the following boundary value problem describes anti-plane shear deformations of an elliptic inclusion with the imperfect interface of the form (2.1) (see Ru & Schiavone 1997):

$$\left. \begin{aligned} \nabla^2 w_1 &= 0, \quad \text{in } S_1, \quad \nabla^2 w_2 = 0, \quad \text{in } S_2 \\ h[w_1 - w_2] &= \mu_2 \frac{\partial w_2}{\partial n} + h\omega^*, \quad \mu_1 \frac{\partial w_1}{\partial n} = \mu_2 \frac{\partial w_2}{\partial n} \quad \text{on } \Gamma \\ w_1(x, y) &\equiv c_1 x - c_2 y + o(1), \quad x^2 + y^2 \rightarrow \infty \end{aligned} \right\} \quad (2.2)$$

Here, c_α , $\alpha=1,2$ are given constants (remote stress parameters).

We denote the complex potentials corresponding to $w_\alpha(x,y)$, $\alpha=1,2$, by $\Phi_1(z)$ and $\Phi_2(z)$, respectively. Since $\Phi_1(z)$ and $\Phi_2(z)$ are analytic within S_1 and S_2 , respectively, we can write,

$$\left. \begin{aligned} 2w_k &= \Phi_k(z) + \overline{\Phi_k(z)} \\ \sigma_{xz} - i\sigma_{yz} &= \mu_k \Phi'_k(z) \end{aligned} \right\} z \in S_k \quad (k=1,2) \quad (2.3)$$

where σ_{xz} and σ_{yz} represent the corresponding stress components in anti-plane shear.

Noting that

$$2 \frac{\partial w_2}{\partial n} = \Phi'_2(z) e^{in(z)} + \overline{\Phi'_2(z) e^{-in(z)}}, \quad z \in \Gamma,$$

where, $e^{in(z)}$ represents (in complex form) the outward unit normal to Γ at z , the boundary value problem (2.2) can now be re-written in complex form as:

$$\left. \begin{aligned} \Phi_1(z) &= \delta \Phi_2(z) + (1-\delta) \overline{\Phi_2(z)} + \alpha \left[\Phi'_2(z) e^{in(z)} + \overline{\Phi'_2(z) e^{-in(z)}} \right] + \omega^*(z), \quad z \in \Gamma \\ \Phi_1(z) &\equiv Az + O(1), \quad |z| \rightarrow \infty. \end{aligned} \right\} \quad (2.4)$$

Here

$$A \equiv c_1 + ic_2, \quad \alpha = \frac{\mu_2}{2h} \geq 0, \quad \delta \equiv \frac{\mu_1 + \mu_2}{2\mu_1} > \frac{1}{2}, \quad \omega^* = \omega z + \overline{\omega z} \quad (2.5)$$

and ω is a known complex constant determined by the uniform eigen-strain given in the inclusion.

2.3 CONFORMAL MAPPING

Let Γ be an ellipse with center at the origin of the complex z -plane, semi-major and semi-minor axes a and b , respectively and foci at $x = \pm 2R$, $R > 0$. Consider the following conformal mapping from the complex z -plane to the complex ξ -plane (Muskhelishvili 1963):

$$z = m(\xi) = R\left(\xi + \frac{1}{\xi}\right), R = \frac{\sqrt{a^2 - b^2}}{2} > 0, \zeta = \zeta + i\eta = re^{i\theta} \quad (2.6)$$

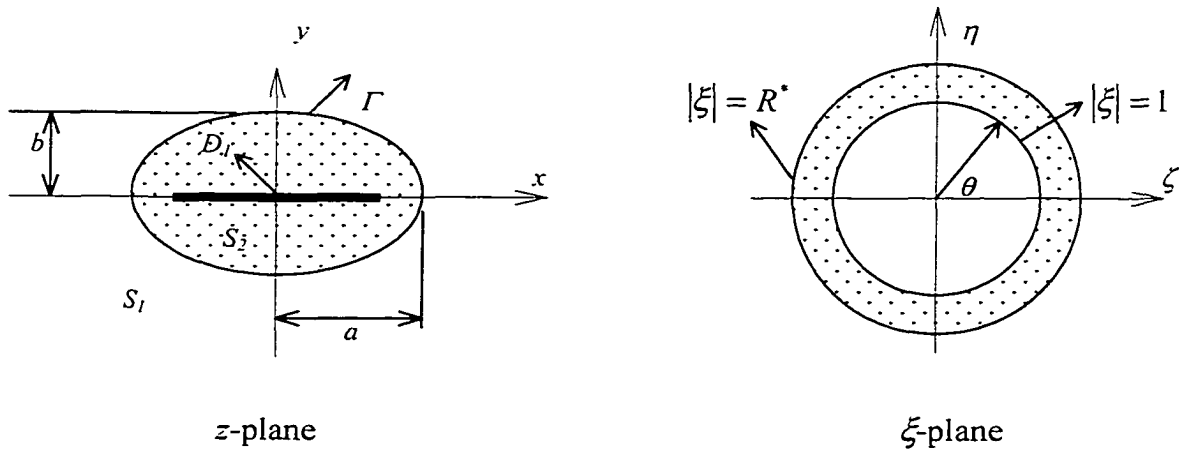


Figure 2.1: The conformal mapping from z -plane to ξ -plane

As illustrated in Figure 2.1, we imagine the enclosed region S_2 to be cut along the segment $D_1 = \{(x,0): -2R \leq x \leq 2R\}$ connecting the foci of the ellipse. This cut may be thought of as an ellipse, which is confocal with Γ but whose minor axis is zero. Hence the cut region in S_2 may be thought of as the limiting case of a region between two confocal ellipses.

Using (2.6), we map the ellipse $x = R(R^* + \frac{1}{R^*})\cos\theta, y = R(R^* - \frac{1}{R^*})\sin\theta$ and its exterior region in the complex z -plane, onto and outside, respectively, the circle of radius R^* in the complex ξ -plane (see Figure 2.1). Here

$$R^* = \frac{a + \sqrt{a^2 - 4R^2}}{2R} = \sqrt{\frac{a+b}{a-b}} > 1 \quad (2.7)$$

Since, $\Phi_2(z)$ is analytic in S_2 , it follows that

$$\Phi_2(z) = \Phi_2(\bar{z}), \quad z \in D_1 \quad (2.8)$$

2.4 GENERAL SOLUTION

For convenience, we write

$$\Phi_\alpha(z) = \Phi_\alpha(m(\xi)) = \Phi_\alpha(\xi), \quad \alpha = 1, 2,$$

so that, in the ξ -plane, condition (2.8) becomes

$$\Phi_2(\xi) = \Phi_2(\bar{\xi}), \quad \forall \xi : |\xi| = 1$$

Using (2.6), writing $\xi = re^{i\theta}$ and noting that (England 1971)

$$e^{i2n(z)} = \frac{\xi^2}{r^2} \frac{m'(\xi)}{m'(\bar{\xi})}, \quad e^{in(z)} = \frac{\xi}{r} \frac{m'(\xi)}{|m'(\xi)|}, \quad e^{-in(z)} = \frac{\bar{\xi}}{r} \frac{\overline{m'(\xi)}}{|m'(\xi)|},$$

the problem (2.4) reduces to finding analytic functions $\Phi_\alpha(\xi)$, $\alpha = 1, 2$ in the regions

$|\xi| > R^*$ and $1 < |\xi| < R^*$, respectively, such that

$$\Phi_1(\zeta) = \delta \Phi_2(\zeta) + (1 - \delta) \overline{\Phi_2(\zeta)} + \beta [\zeta \Phi_2'(\zeta) + \overline{\zeta \Phi_2'(\zeta)}] + \omega m(\zeta) + \overline{\omega m(\zeta)}, \quad |\zeta| = R^* \quad , \quad (2.9)$$

$$\Phi_2(\zeta) = \Phi_2(\bar{\zeta}), \quad |\zeta| = 1, \quad (2.10)$$

$$\Phi_1(\zeta) \cong AR\zeta + O(1), \quad |\zeta| \rightarrow \infty. \quad (2.11)$$

Here,

$$\beta(\theta) = \frac{\alpha}{R^* |m'(\xi)|} = \frac{\alpha}{b \sqrt{1 + b^* \sin^2 \theta}}, \quad b^* = \frac{a^2 - b^2}{b^2} > 0 \quad (2.12)$$

Since $\Phi_1(\xi)$ is analytic in $|\xi| > R^*$, using (2.11), it can be represented there by the

following Laurent series

$$\Phi_1(\zeta) = AR\zeta + \sum_{n=0}^{\infty} d_n \zeta^{-n} \quad (2.13)$$

where d_n are unknown coefficients to be determined. Similarly, $\Phi_2(\zeta)$ is analytic in the annulus $I < |\zeta| < R^*$ and hence has Laurent series representation there given by

$$\Phi_2(\zeta) = \sum_{n=-\infty}^{\infty} b_n \zeta^n \quad (2.14)$$

where, again, b_n are unknown constants to be determined.

From Eq. (2.10), letting $\zeta = re^{i\theta}$ we obtain (see, for example, Muskhelishvili 1963)

$$b_n = b_{-n}, \quad \Phi_2(\zeta) = \sum_{n=0}^{\infty} b_n (\zeta^n + \zeta^{-n}) \quad (2.15)$$

In the following equations, since the constants b_0 and d_0 make no contribution to the calculation of stresses, they will be taken to be zero. The problem is then reduced to the determination of the complex coefficients d_n and b_n ($n = 1, 2, \dots$). The interface condition (2.9) can be rewritten as

$$\Phi_1(\zeta) - \delta\Phi_2(\zeta) + (\delta - 1)\overline{\Phi_2(\zeta)} = \beta[\zeta\Phi_2'(\zeta) + \overline{\zeta\Phi_2'(\zeta)}] + \omega m(\zeta) + \overline{\omega m(\zeta)}, \quad |\zeta| = R^* \quad (2.16)$$

Using (2.13) and (2.15), the left-hand side of Eq. (2.16) becomes

$$AR\xi - \delta \sum_{n=1}^{\infty} b_n \xi^n + (\delta - 1) \sum_{n=1}^{\infty} \overline{b_n} \xi^{-n} + \sum_{n=1}^{\infty} d_n \xi^{-n} - \delta \sum_{n=1}^{\infty} b_n \xi^{-n} + (\delta - 1) \sum_{n=1}^{\infty} \overline{b_n} \xi^n$$

Since the above expression is real, we obtain (setting $\xi = R^* e^{i\theta}$)

$$d_1 = \overline{AR}(R^*)^2 + (2\delta - 1)[b_1 - \overline{b_1}(R^*)^2] \quad \text{when } n = 1 \quad (2.17)$$

$$d_n = (2\delta - 1)[b_n - \overline{b_n}(R^*)^{2n}] \quad \text{when } n \neq 1 \quad (2.18)$$

Using the expressions (2.17) and (2.18) to eliminate d_n ($n = 1, 2, \dots$), the left-hand side of Eq. (2.16) becomes

$$\begin{aligned} \Phi_1(\xi) - \delta \Phi_2(\xi) + (\delta - 1) \overline{\Phi_2(\xi)} = RR^* (Ae^{i\theta} + \overline{A}e^{-i\theta}) - \\ \delta \sum_{n=1}^{\infty} [b_n e^{in\theta} + \overline{b_n} e^{-in\theta}] (R^*)^n + (\delta - 1) \sum_{n=1}^{\infty} (R^*)^{-n} [\overline{b_n} e^{in\theta} + b_n e^{-in\theta}], \quad |\xi| = R^* \end{aligned} \quad (2.19)$$

Noting Eqs. (2.6), (2.12) and (2.16) and setting $\xi = R^* e^{i\theta}$, the interface condition (2.16) is further reduced to:

$$\begin{aligned} \sqrt{1 + b^* \sin^2 \theta} \left\{ RR^* \left[(A - \omega - \frac{\overline{\omega}}{R^{*2}}) e^{i\theta} + (\overline{A} - \overline{\omega} - \frac{\omega}{R^{*2}}) e^{-i\theta} \right] - \sum_{n=1}^{\infty} \delta [b_n e^{in\theta} + \overline{b_n} e^{-in\theta}] (R^*)^n + \right. \\ \left. \sum_{n=1}^{\infty} (\delta - 1) (R^*)^{-n} [\overline{b_n} e^{in\theta} + b_n e^{-in\theta}] \right\} = \sum_{n=1}^{\infty} \frac{\alpha n}{b} \left[(R^*)^n (b_n e^{in\theta} + \overline{b_n} e^{-in\theta}) - (R^*)^{-n} (b_n e^{-in\theta} + \overline{b_n} e^{in\theta}) \right] \end{aligned} \quad (2.20)$$

Substituting the expression (see Appendix)

$$\sqrt{1+b^* \sin^2 \theta} = \sum_{k=-\infty}^{\infty} I_{2k} e^{i2k\theta} \approx \sum_{k=0}^{M-1} I_{2k} (e^{i2k\theta} + e^{-i2k\theta}) + I_{2M} \frac{e^{i2M\theta} + e^{-i2M\theta} - \eta(e^{i2(M-1)\theta} + e^{i2(1-M)\theta})}{1 + \frac{1}{R^{*4}} - \frac{e^{i2\theta} + e^{-i2\theta}}{R^{*2}}} \quad (2.21)$$

into Eq. (2.20) (here M is a sufficiently large integer) and letting $T = A - \omega - \frac{\bar{\omega}}{R^{*2}}$, we

obtain

$$\begin{aligned} & RR^* \left\{ \sum_{k=0}^{M-1} I_{2k} (e^{i2k\theta} + e^{-i2k\theta}) \left[1 + \frac{1}{R^{*4}} - \frac{e^{i2\theta} + e^{-i2\theta}}{R^{*2}} \right] + I_{2M} [e^{i2M\theta} + e^{-i2M\theta} - \eta(e^{i2(M-1)\theta} + e^{i2(1-M)\theta})] \right\} \\ & \times (Te^{i\theta} + \bar{T}e^{-i\theta}) = \\ & \delta \left\{ \sum_{k=0}^{M-1} I_{2k} (e^{i2k\theta} + e^{-i2k\theta}) \left[1 + \frac{1}{R^{*4}} - \frac{e^{i2\theta} + e^{-i2\theta}}{R^{*2}} \right] + I_{2M} [e^{i2M\theta} + e^{-i2M\theta} - \eta(e^{i2(M-1)\theta} + e^{i2(1-M)\theta})] \right\} \times \\ & \sum_{n=1}^{\infty} [b_n e^{in\theta} + \bar{b}_n e^{-in\theta}] (R^*)^n + (1-\delta) \times \\ & \left\{ \sum_{k=0}^{M-1} I_{2k} (e^{i2k\theta} + e^{-i2k\theta}) \left[1 + \frac{1}{R^{*4}} - \frac{e^{i2\theta} + e^{-i2\theta}}{R^{*2}} \right] + I_{2M} [e^{i2M\theta} + e^{-i2M\theta} - \eta(e^{i2(M-1)\theta} + e^{i2(1-M)\theta})] \right\} \\ & \times \sum_{n=1}^{\infty} [\bar{b}_n e^{in\theta} + b_n e^{-in\theta}] (R^*)^{-n} + \frac{\alpha}{b} \left[1 + \frac{1}{R^{*4}} - \frac{e^{i2\theta} + e^{-i2\theta}}{R^{*2}} \right] \times \\ & \sum_{n=1}^{\infty} n [b_n e^{in\theta} + \bar{b}_n e^{-in\theta}] (R^*)^n - \frac{\alpha}{b} \left[1 + \frac{1}{R^{*4}} - \frac{e^{i2\theta} + e^{-i2\theta}}{R^{*2}} \right] \sum_{n=1}^{\infty} n [\bar{b}_n e^{in\theta} + b_n e^{-in\theta}] (R^*)^{-n} \end{aligned} \quad (2.22)$$

Furthermore, noting that $I_{2k} = I_{-2k}$, and equating coefficients of $e^{in\theta}$ in the interface condition (2.22), we finally obtain

$$\sum_{j=0}^{\frac{m-1}{2}} \left(\sum_{k=0}^M D_{nkj} I_{2k} + G_{nj} \right) b_{2j+1} + \sum_{j=0}^{\frac{m-1}{2}} \left(\sum_{k=0}^M E_{nkj} I_{2k} + P_{nj} \right) \bar{b}_{2j+1} = \sum_{k=0}^M F_{nk} I_{2k} \quad (2.23)$$

Here, $n = 1, 3, 5, \dots, m$, where m is odd and always less than M ; D_{nkj} , E_{nkj} are real constants; G_{nj} , P_{nj} are real constants related to the imperfect interface parameter h and F_{nk} are complex constants. For example, by comparing Eqs. (2.22) and (2.23), when $M=5$, $n=3$ ($m=5$), we obtain

$$\begin{aligned} D_{300} &= -\frac{\delta}{R^*}; D_{310} = \delta R^* + \frac{2\delta - 1}{R^{*3}}; D_{320} = \frac{(1 - 2\delta)}{R^*} + \frac{1 - \delta}{R^{*5}}; D_{330} = -\frac{1 - \delta}{R^{*3}}; D_{340} = D_{350} = 0; \\ G_{30} &= -\frac{\alpha}{bR^*}; E_{300} = -\frac{1 - \delta}{R^{*3}}; E_{310} = \frac{1 - \delta}{R^{*5}} - \frac{2\delta - 1}{R^*}; E_{320} = \delta R^* + \frac{2\delta - 1}{R^{*3}}; E_{330} = -\frac{\delta}{R^*}; \\ E_{340} &= E_{350} = 0; P_{30} = \frac{\alpha}{bR^{*3}} \\ D_{301} &= \delta(R^{*3} + \frac{1}{R^*}); D_{311} = -2\delta R^* - \frac{1 - \delta}{R^{*5}}; D_{321} = -\frac{1 - \delta}{R^{*5}}; D_{331} = (1 - \delta)(\frac{1}{R^{*3}} + \frac{1}{R^{*7}}); \\ D_{341} &= D_{351} = 0; G_{31} = \frac{3\alpha}{b}(R^{*3} + \frac{1}{R^*}) \\ E_{301} &= (1 - \delta)(\frac{1}{R^{*3}} + \frac{1}{R^{*7}} - \frac{1}{R^{*5}}); E_{311} = \frac{1 - \delta}{R^{*5}}; E_{321} = \delta R^*; E_{331} = \delta(R^{*3} + \frac{1}{R^*}); \\ E_{341} &= -\delta R^*; E_{351} = 0; P_{31} = -\frac{3\alpha}{b}(\frac{1}{R^{*3}} + \frac{1}{R^{*7}}) \end{aligned}$$

$$\begin{aligned}
D_{302} &= -\delta R^{*3}; D_{312} = \delta(R^{*5} + R^*); D_{322} = -\delta R^{*3}; D_{332} = -\frac{1-\delta}{R^{*5}}; D_{342} = (1-\delta)\left(\frac{1}{R^{*5}} + \frac{1}{R^{*9}}\right); \\
D_{352} &= -\frac{1-\delta}{R^{*5}}\eta; G_{32} = -\frac{5\alpha}{b}R^{*5} \\
E_{302} &= -(1-\delta)\frac{1}{R^{*7}}; E_{312} = (1-\delta)\left(\frac{1}{R^{*5}} + \frac{1}{R^{*9}}\right); E_{322} = -(1-\delta)\frac{1}{R^{*7}}; E_{332} = \delta R^{*3}; \\
E_{342} &= \delta(R^{*5} + R^*); E_{352} = -\delta R^{*5}\eta; P_{32} = \frac{5\alpha}{b}\frac{1}{R^{*7}} \\
F_{30} &= 0; F_{31} = T\left(1 + \frac{1}{R^{*4}}\right) - \frac{\bar{T}}{R^{*2}}; F_{32} = \bar{T}\left(1 + \frac{1}{R^{*4}}\right) - \frac{T}{R^{*2}}; F_{33} = -\frac{\bar{T}}{R^{*2}}; F_{34} = F_{35} = 0
\end{aligned}$$

2.5 NUMERICAL EXAMPLES AND DISCUSSION

We compute (numerically) the complex coefficients of the Laurent series for a wide range of imperfect interface parameters and aspect ratios a/b .

2.5.1 The Case of Remote Mechanical Loading

We first consider the case of remote loading in the absence of any eigenstrain inside the inclusion. That is, when $T = A$, $\bar{T} = \bar{A}$.

Let $b = 1$ and consider the case of an epoxy matrix surrounding a glass inclusion. The material properties of the matrix and the inclusion are described by (Huang and Hu 1995):

$$E_1 = 2.76 \text{ Gpa}, \nu_1 = 0.35, \mu_1 = 1.02 \text{ Gpa}$$

$$E_2 = 72.4 \text{ Gpa}, \nu_2 = 0.2, \mu_2 = 30.17 \text{ Gpa},$$

where, E is Young's modulus and ν is Poisson's ratio.

It is well known that, in the case of a perfectly bonded interface in anti-plane elasticity, the stress and strain fields inside an elliptic inclusion are uniform (see, for example, Ru & Schiavone 1996). In fact, when $h = \infty$ (corresponding to $\alpha=0$, perfect bonding) and $G_{nj} = P_{nj} = 0$ in (2.23), we obtain

$$\delta R^* b_1 + \frac{1-\delta}{R^*} b_1 = A R R^*, \quad b_1 = \frac{R}{\delta} \frac{A - \delta^* \bar{A}}{1 - \delta^{*2}}, \quad b_3 = b_5 = \dots = 0 \quad \text{where } \delta^* = \frac{1-\delta}{\delta R^{*2}}.$$

Consequently,

$$\Phi_2 = b_0 + \frac{R}{\delta} \frac{A - \delta^* \bar{A}}{1 - \delta^{*2}} \frac{z}{R},$$

which coincides with the result obtained in Ru & Schiavone (1996) for an elliptic inclusion with perfectly bonded interface.

In practice, the imperfect interface parameter h is rendered dimensionless by division by μ_1 / b , where μ_1 is the shear modulus of the matrix and b is the minor axis of the ellipse.

In the case of the homogeneously imperfect interface, numerical computation of the corresponding series demonstrates that the non-uniformity of the stress field inside the inclusion depends significantly on the aspect ratio of the ellipse and the imperfect interface parameter.

In what follows, we present results for three different ranges of the aspect ratio a/b . In each case, the number of coefficients in the corresponding series is chosen so that the error in the numerical calculations is maintained below 1%. This is achieved simply by calculating an increasing sequence of partial sums from each of the (uniformly convergent) infinite series representations and noting the minimum number of coefficients required to ensure that the difference between any two subsequent partial sums is less than 1%.

CASE 1 When $1 < a/b \leq 3$, only the coefficients b_1 and b_3 are necessary to achieve the desired accuracy. In this case, we find that

$$\Phi_2 \approx b_0 + (b_1 - 3b_3) \left(\frac{z}{R} \right) + b_3 \left(\frac{z}{R} \right)^3 \quad (2.24)$$

We obtain values of b_1 and b_3 by selecting $m = 3$ and $M = 7$ in Eq. (2.23). It should be noted that the result for $a/b = 1$ cannot be obtained directly from the numerical analysis but is available analytically. The relationship between average stress and the imperfect parameter h , in this case, is given in Figure 2.2.

The average stress inside the inclusion is defined as

$$\bar{\sigma}_{ij} = \frac{\int \sigma_{ij} dA}{A} \quad (2.25)$$

where A is the area of the ellipse.

In Figures 2.3 and 2.4, the stress distribution along the interface and the regions of the ellipse described by the lines $x = 0$ and $y = 0$ is plotted for the value $a/b = 3$ and different values of the parameter h . It is clear that the non-uniformity of the stresses inside the inclusion is very strong. In fact, when $h = 5E+5$, the local stresses reach maximum values.

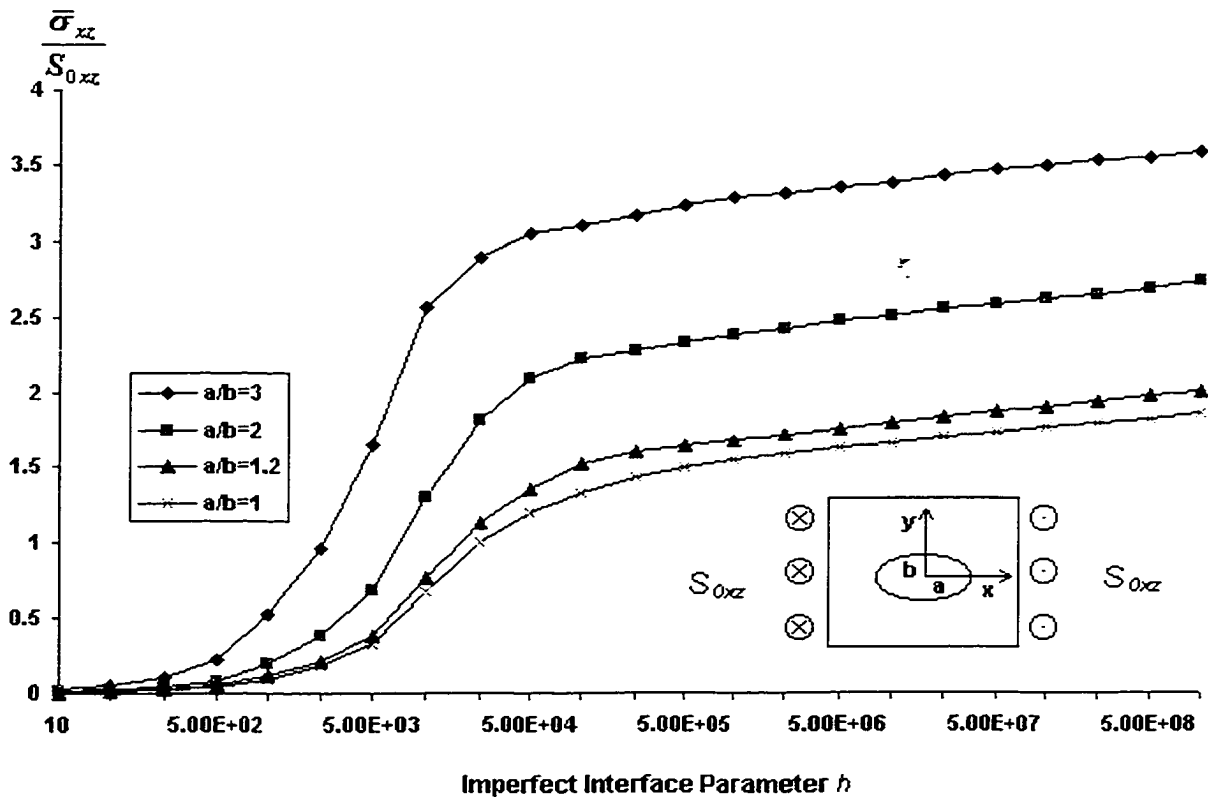


Figure 2.2: Effect of the imperfect interface parameter h on the average stress ($\bar{\sigma}_{xz} / S_{0xz}$) inside the inclusion when the remote stress is S_{0xz}

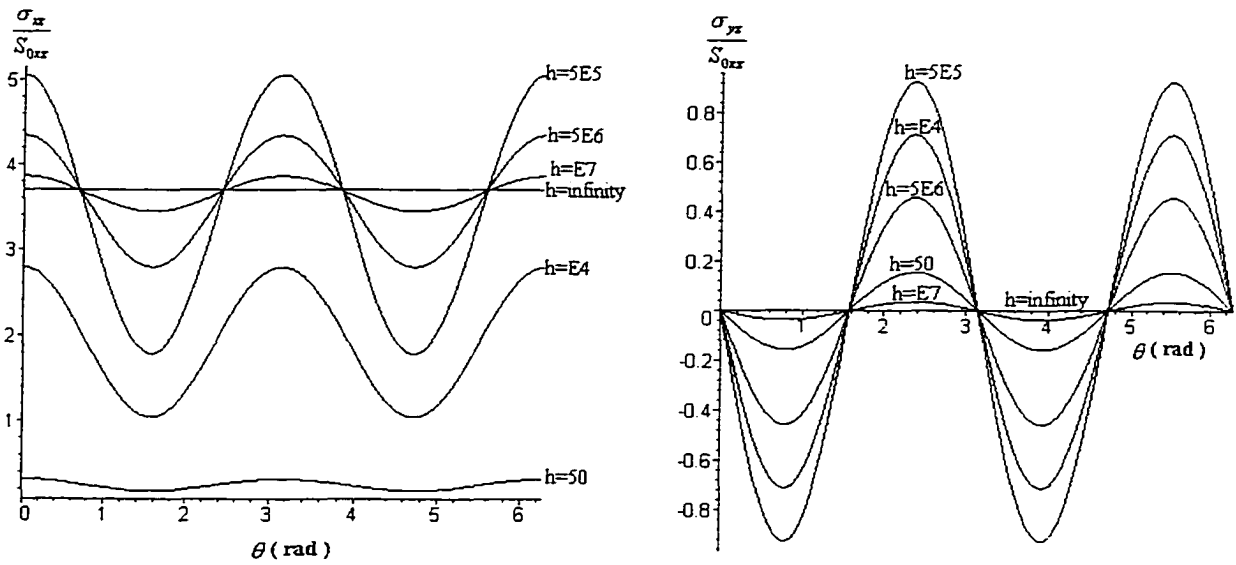


Figure 2.3: Non-uniformity of stress along the interface when the remote stress is S_{0xz} with $a/b=3$

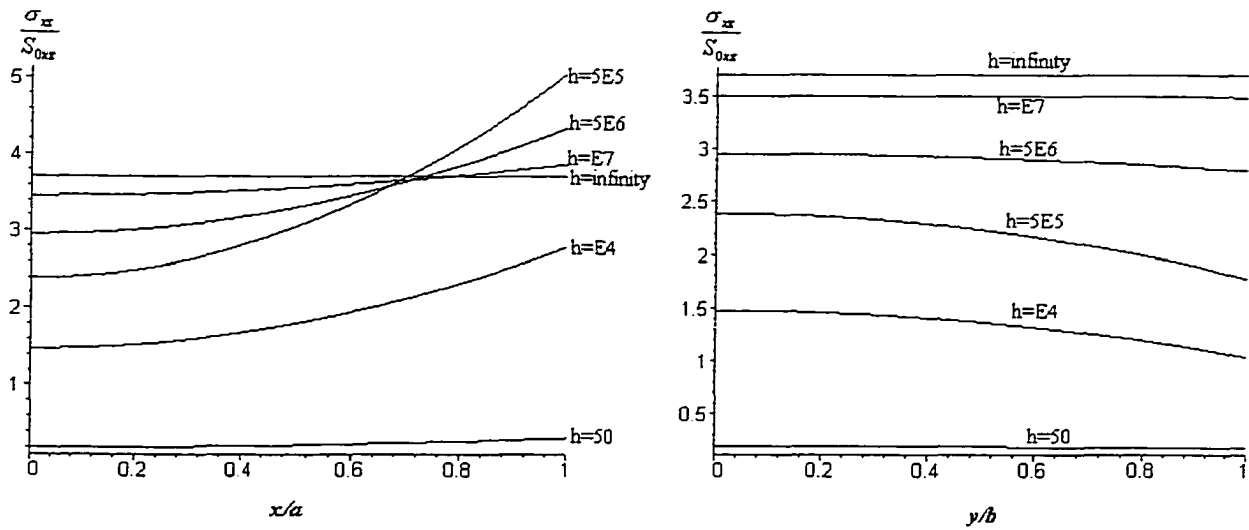


Figure 2.4: The stress distribution along the x and y axes for remote stress S_{0xz} with $a/b=3$

CASE 2 When $3 < a/b \leq 6$, it is sufficient to consider only the coefficients b_1 , b_3 and b_5 to obtain the required accuracy. In this case, we obtain

$$\Phi_2 \approx b_0 + (b_1 - 3b_3 + 5b_5) \left(\frac{z}{R}\right) + (b_3 - 5b_5) \left(\frac{z}{R}\right)^3 + b_5 \left(\frac{z}{R}\right)^5 \quad (2.26)$$

We may obtain values of b_1 , b_3 and b_5 by selecting $m=5$ and $M=9$ in Eq. (2.23).

The corresponding stress distributions are presented in Figures 2.5, 2.6 and 2.7.

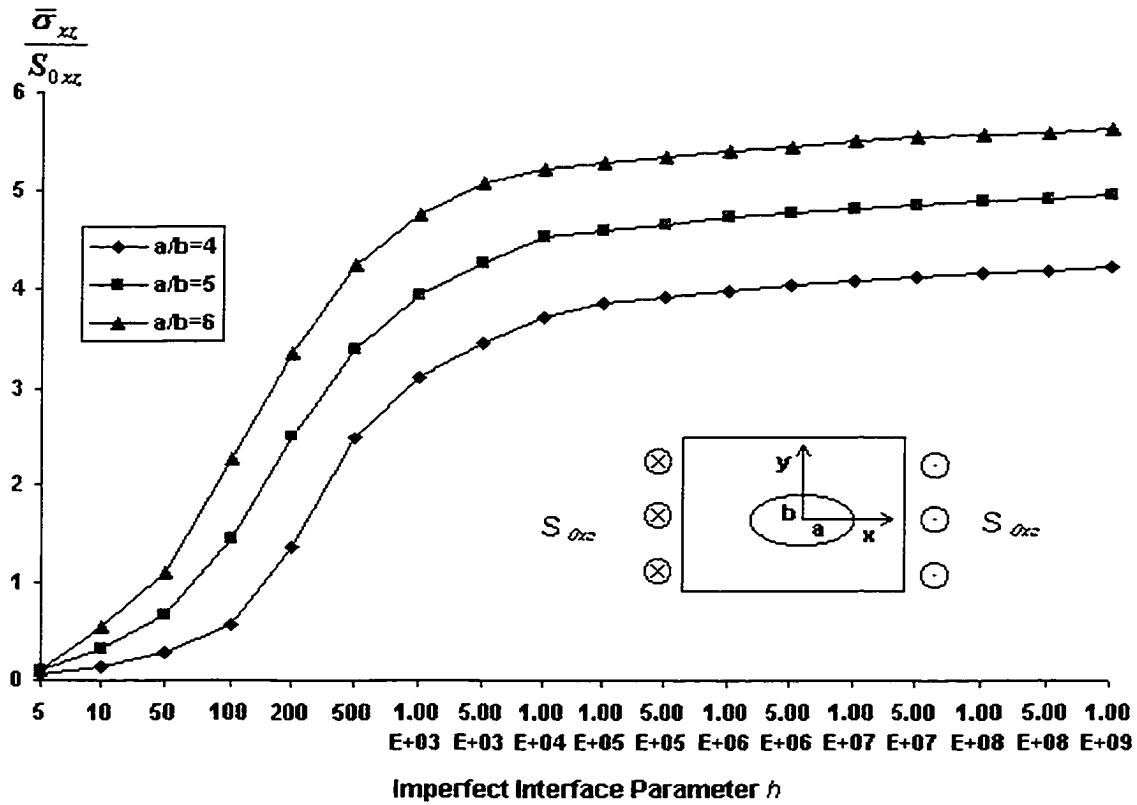


Figure 2.5: Effect of the imperfect interface parameter h on the average stress ($\bar{\sigma}_{xz} / S_{0,xz}$)

inside inclusion when the remote stress is $S_{0,xz}$

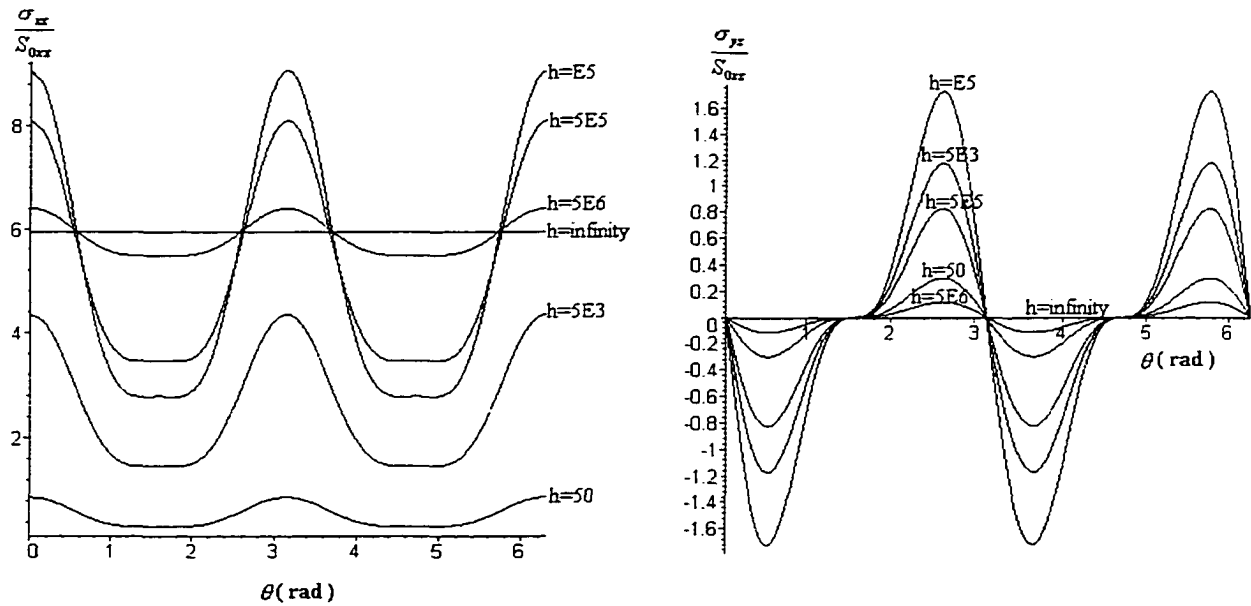


Figure 2.6: Non-uniformity of stress along the interface when the remote stress is S_{0xz} with $a/b=6$

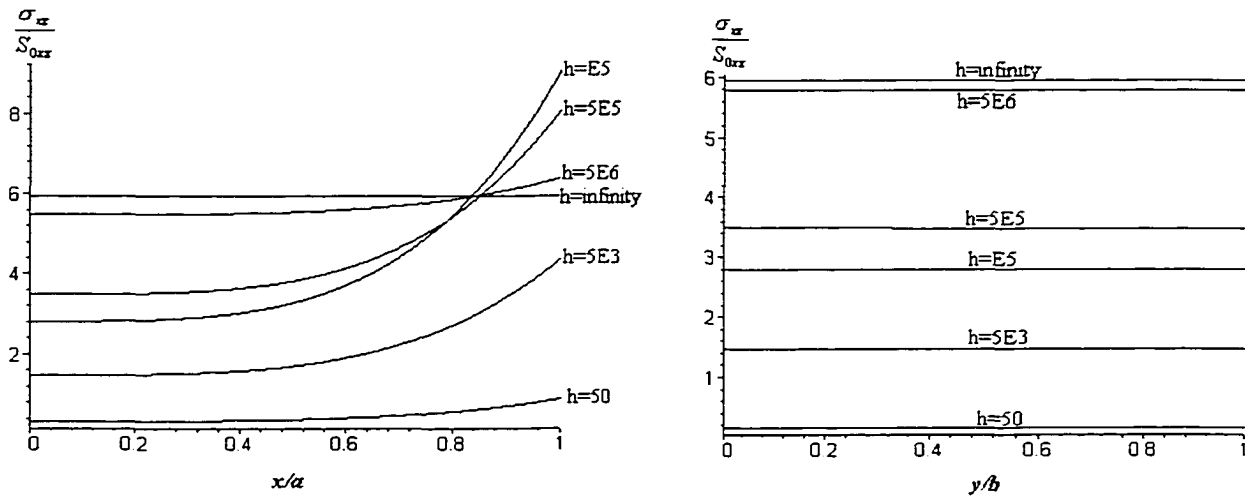


Figure 2.7: The stress distribution along the x and y axes for remote stress S_{0xz} with $a/b=6$

CASE 3 When $6 < a/b \leq 9$, only b_1 , b_3 , b_5 and b_7 are required to obtain the desired accuracy. In this case, we obtain

$$\Phi_2 \approx b_0 + (b_1 - 3b_3 + 5b_5 + 28b_7) \frac{z}{R} + (b_3 - 5b_5 + 14b_7) \left(\frac{z}{R}\right)^3 + (b_5 - 7b_7) \left(\frac{z}{R}\right)^5 + b_7 \left(\frac{z}{R}\right)^7 \quad (2.27)$$

We may obtain values of b_1 , b_3 , b_5 and b_7 by selecting $m=7$, $M=11$ in Eq. (2.23).

The corresponding stress distributions are presented in Figures 2.8, 2.9, 2.10.

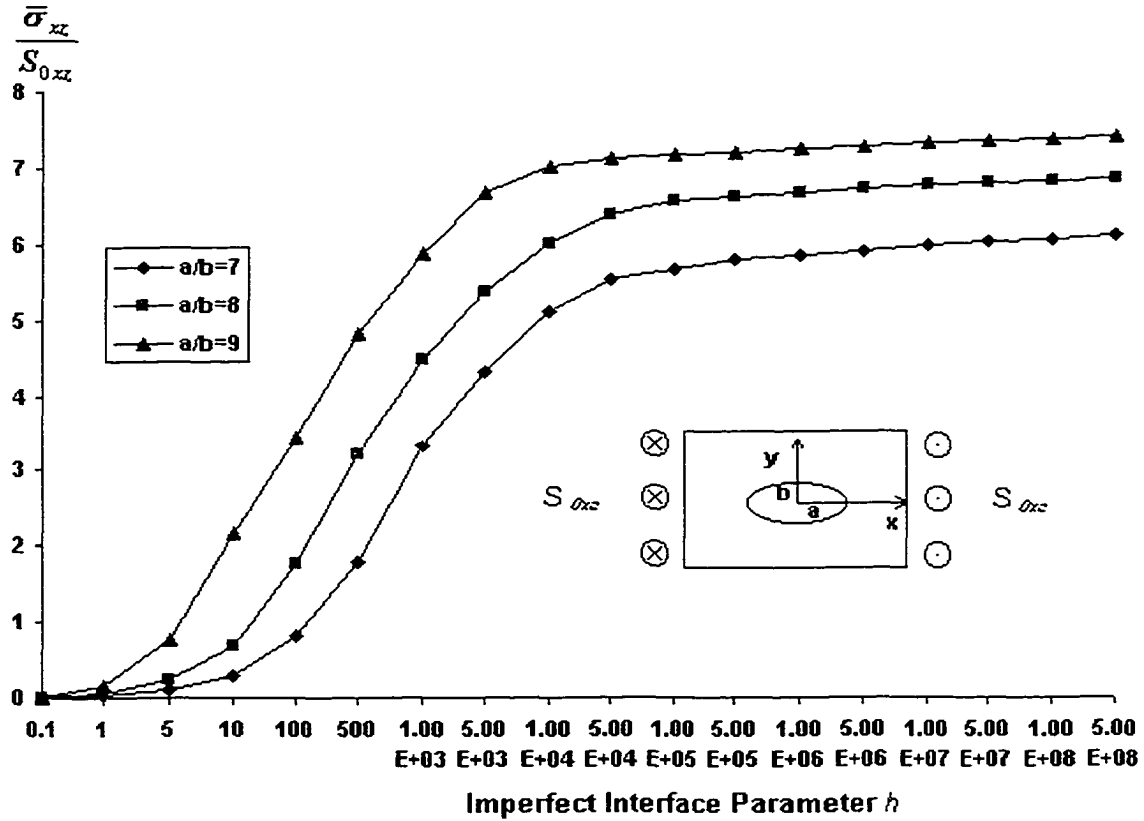


Figure 2.8: Effect of the imperfect interface parameter h on the average stress ($\bar{\sigma}_{xz} / S_{0,xz}$)

inside the inclusion when the remote stress is $S_{0,xz}$

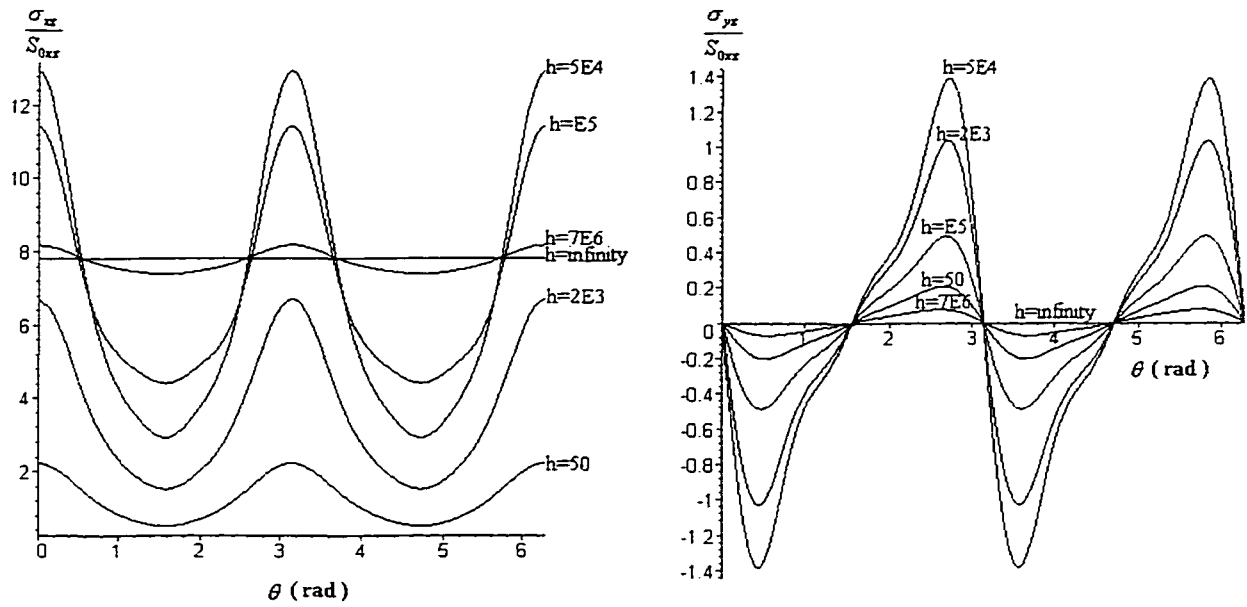


Figure 2.9: Non-uniformity of stress along the interface when the remote stress is S_{0xz}

with $a/b=9$

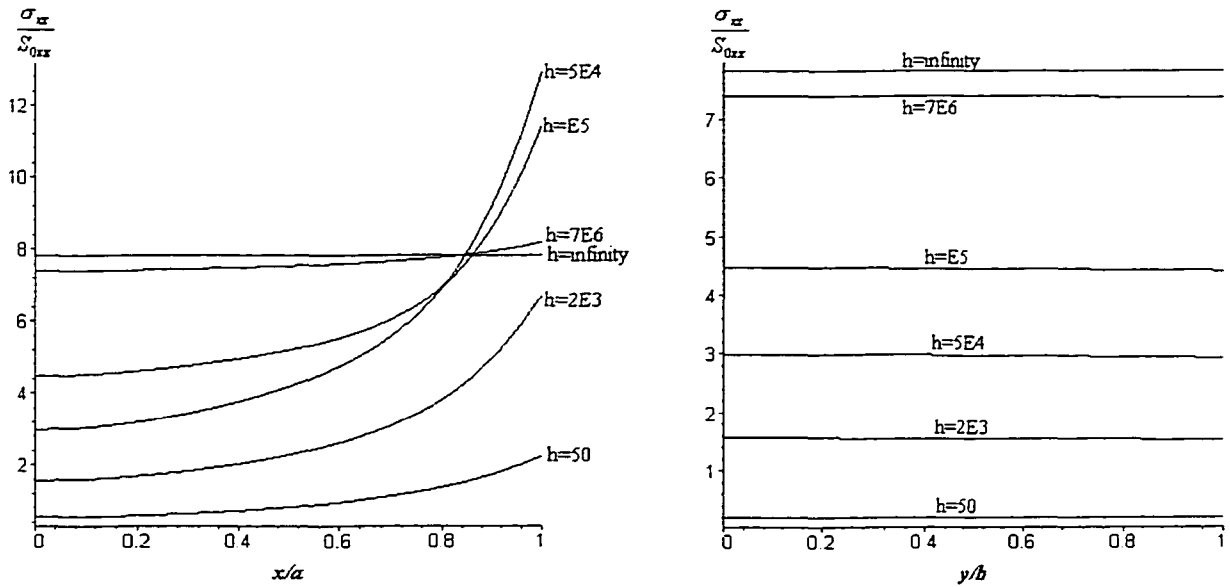


Figure 2.10: The stress distributions along the x and y axes for the remote stress S_{0xz} with

$a/b=9$

It is noted that for values of the aspect ratio $a/b \geq 10$, the procedure is similar although a much larger number of coefficients is required to evaluate the corresponding series to the desired accuracy.

The above results indicate that the average stress alone is insufficient to describe the debonding and failure of the interface because the average stress is a monotonic function of h . This means that the average stress does not give any useful information about the debonding and failure of the interface. It is the local stress (maximum) that decides where the debonding and failure will occur. For example, from the stress distribution along the interface in Figure 2.9, the maximum local stresses occur at $\theta = 0, \pi$. These stresses are much greater than those in the case of perfect bonding although the average stresses (see Figure 2.8) are smaller. In addition, from Figures 2.2, 2.5 and 2.8, it is clear that the effect of the imperfect interface parameter h on the average stress inside the inclusion increases with the aspect ratio of the ellipse.

It should be emphasized that the imperfect interface condition (2.1) arises from the assumption of the existence of a thin flexible coating (interphase layer) of thickness $t \ll b$ with shear modulus $\mu_c \ll \min\{\mu_1, \mu_2\}$ between the inclusion and the matrix (Hashin 1991b). This defines the physical meaning of the parameter h . In practice; the interface model may be represented by an adhesive layer. For the present case, h is in the range 1 to 10^6 which demonstrates that the stress field is closely related to this physical meaning of h . In addition, the local stresses along the (imperfect) interface itself reach maximum values when the interface parameter h reaches a particular value (h^*). For the example

under consideration, the relationship between the parameter h^* and the aspect ratio a/b is presented in Figure 2.11.

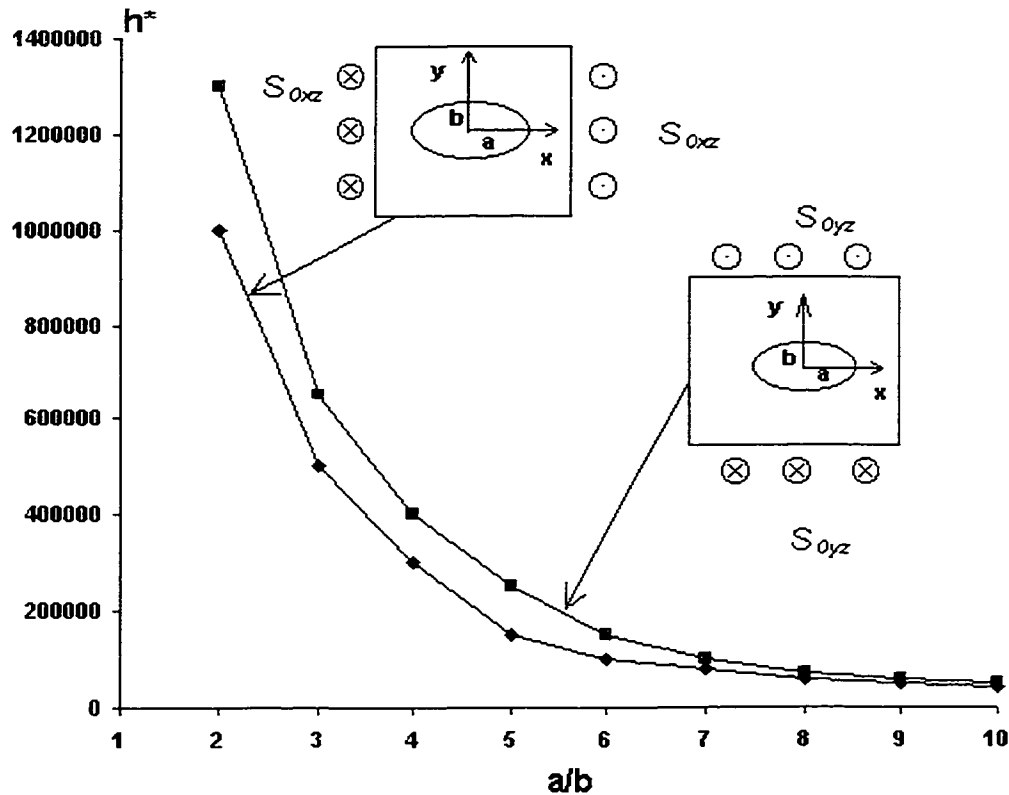


Figure 2.11: The relationship between h^* and a/b

Since values of h^* correspond to local maximum stress and are related to the mechanical properties and thickness of the adhesive layer between the inclusion and the matrix, the parameter h^* may be used as a control parameter when designing composites involving elastic inclusions. For example, for the remote loading S_{0xz} and aspect ratio $a/b=1$ (circular inclusion), the peak stress corresponds to the value $h^* = \infty$ (perfect bonding). However, when $a/b=3$, the peak stress corresponds to $h^* = 5E+5$. Since h^* is rendered dimensionless by division by μ_1/b , for a specific aspect ratio, we could avoid the peak

stress by adjusting μ_l (the shear moduli of the matrix), and the thickness of the interphase layer (related to b).

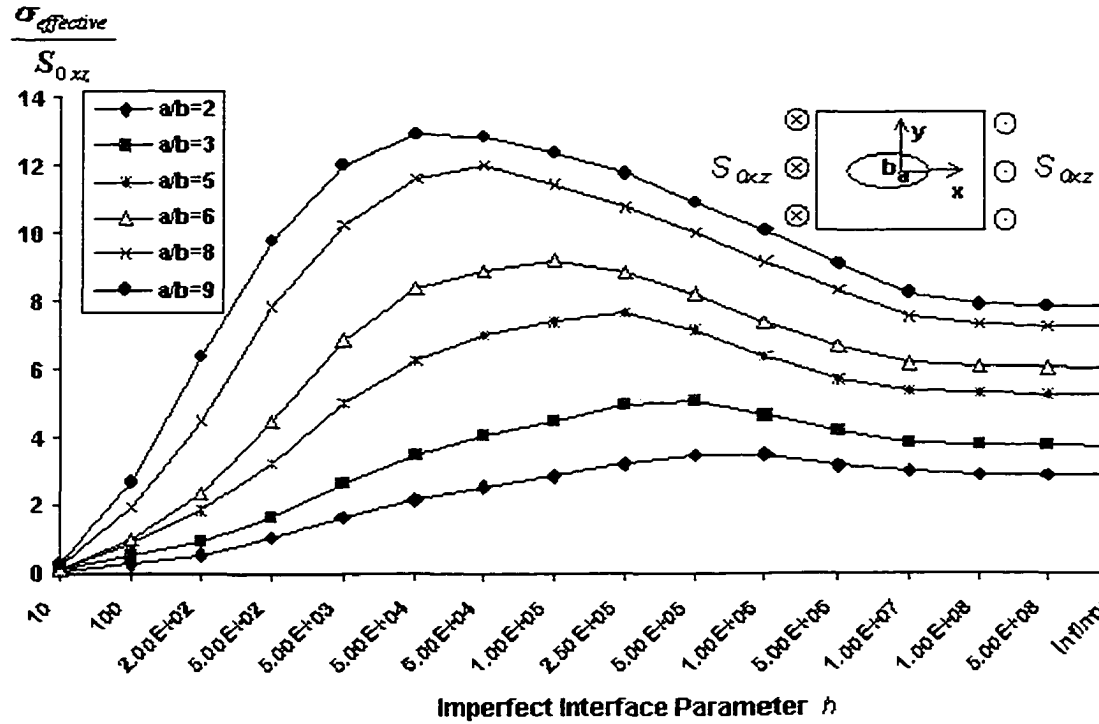


Figure 2.12: The effective peak stress along the interface varies as a function of the imperfect interface parameter h when the remote stress is S_{0xz}

In order to better understand the relationship between the imperfect interface parameter h and the failure of the interface, Figure 2.12 plots the peak stresses as a function of the imperfect interface parameter. These peak stresses are calculated at the values $\theta = 0$ or π and correspond to the effective stress which is defined by the relation

$$\sigma_{effective} = \sqrt{\sigma_{xz}^2 + \sigma_{yz}^2}. \text{ In Figures 2.3, 2.6 and 2.9, we note that the values of } \frac{\sigma_{yz}}{S_{0xz}} \text{ are}$$

much smaller than the corresponding values of $\frac{\sigma_{xz}}{S_{0,xz}}$ when the remote stress is $S_{0,xz}$.

Thus, the effective stress is mainly determined by $\frac{\sigma_{xz}}{S_{0,xz}}$. Furthermore, at the values $\theta = 0$

or π , the effective stresses is equal to the values of $\frac{\sigma_{xz}}{S_{0,xz}}$ because the values of $\frac{\sigma_{yz}}{S_{0,xz}}$ are

zero. The maximum peak stresses in Figure 2.12 correspond to values of the parameter h^* . For the circular inclusion, we know that the maximum peak stress appears at $h=\infty$ (see Ru & Schiavone 1997). However, for the elliptic inclusion, the maximum peak stresses are related to the imperfect interface parameter and the aspect ratio. To explain this, we note that for the present interphase layer model (Hashin 1991b), in order to keep the thickness of the adhesive layer between the elliptic inclusion and the matrix uniform, unlike the innermost edge, the outer edge of the interphase layer cannot be elliptical. This is why, in the case of a homogeneously imperfect interface, values of h^* correspond to different local maximum stresses for different values of the aspect ratio a/b (for the circular inclusion with homogeneously imperfect interface the outer edge of the interphase layer is circular). This makes the stress distributions along the interface extremely complicated in the case of an elliptic inclusion.

2.5.2 Eigenstrain Problem

By a suitable choice of eigenstrain in S_2 , the problem considered in § 2.5.1 (remote loading with no eigenstrain in S_2) can be shown to be equivalent (in the sense that the

stress field induced within S_2 is equivalent) to one in which the remote loading is zero. In fact, if A is the remote loading parameter, we choose the eigenstrain ω such that

$$\begin{cases} \omega + \frac{\bar{\omega}}{R^{*2}} = -A \\ \bar{\omega} + \frac{\omega}{R^{*2}} = -\bar{A} \end{cases} \Rightarrow \begin{cases} \omega = -\frac{R^{*2}(\bar{A}R^{*2} - A)}{R^{*4} - 1} \\ \bar{\omega} = -\frac{R^{*2}(AR^{*2} - \bar{A})}{R^{*4} - 1} \end{cases} \quad (2.28)$$

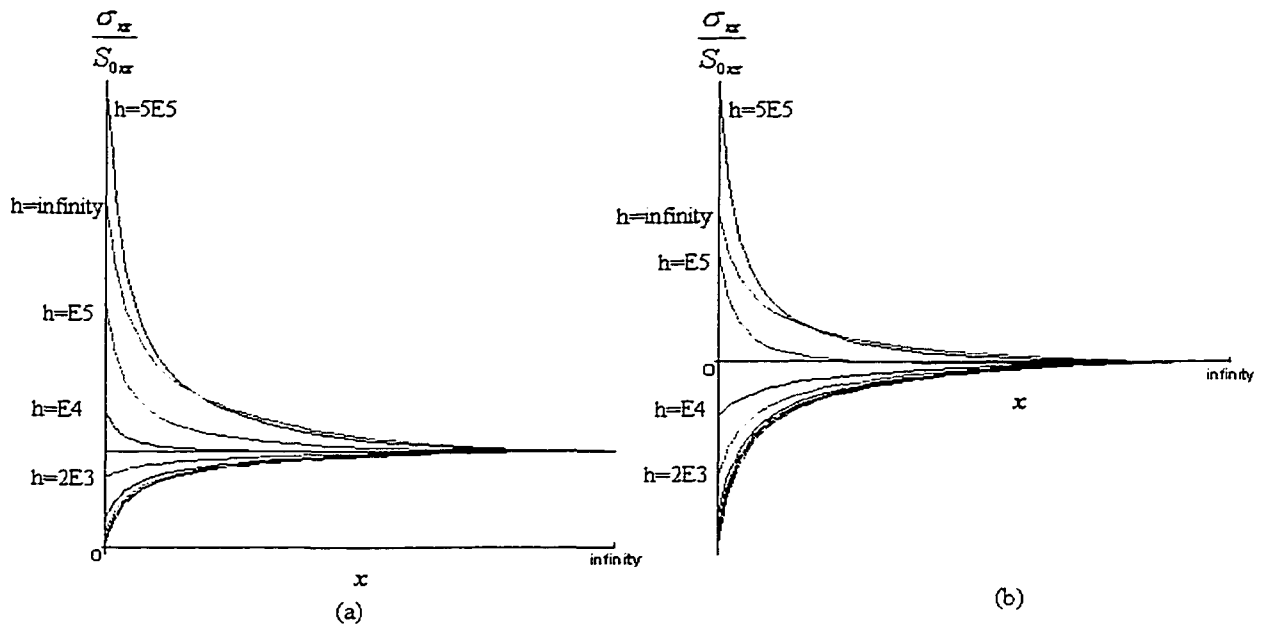


Figure 2.13: The stress distribution with $a/b=3$ for the matrix along x axis with different h when (a) remote mechanical loading S_{0xz} ; (b) eigenstrain loading

It is worth noting that for the above condition, the stress distribution in the eigenstrain problem is equivalent (to that with remote loading and no eigenstrain in S_2) only within the inclusion, and not in the matrix. For example, the stress distribution in the matrix

along the x -axis in the case when $a/b=3$ is presented in Figure 2.13. In the case of remote mechanical loading, all stresses in the matrix tend to $\frac{\sigma_{\varepsilon}}{S_{0,x}} = 1$ when x tends to infinity, as expected. On the other hand, for the eigenstrain loading, all stresses tend to $\frac{\sigma_{\varepsilon}}{S_{0,x}} = 0$ in the similar situation.

2.6 SUMMARY OF RESULTS OBTAINED

This chapter presents a semi-analytic solution of the problem of an elliptic inclusion with homogeneously imperfect interface in anti-plane shear. The results show that the interface imperfection has a significant effect on stress fields in and near the inclusion (along the interface). The non-uniformity of stress is closely related to the interface parameter describing the imperfection and the aspect ratio of the ellipse. It has also been demonstrated that the definition of the imperfect interface and the physical explanation of the interface parameters used in Hashin (1991b) are indeed suitable for describing the nature of the interface.

Our calculations show that using only average stress is insufficient to describe the debonding and failure of the material interface since both are controlled by interfacial stresses which are themselves closely related to the imperfect interface condition. Furthermore, it has been shown that the effect of the imperfect interface parameter h on the average stress inside the inclusion increases with the aspect ratio of the ellipse. In particular, our results indicate that it is possible to predict and control the debonding and

failure of the interface by identifying a distinct value (h^*) of the interface parameter which depends on the aspect ratio of the ellipse and the properties and thickness of the adhesive layer between the elliptic inclusion and the matrix. This is a direct consequence of the fact that values of h^* correspond to maximum peak stress along the interface. Furthermore, we have shown that, for a specific aspect ratio, it is possible to avoid or minimize peak interfacial stress by adjusting μ_l (the shear modulus of the matrix) and the thickness of the interphase layer.

CHAPTER 3

STRESS ANALYSIS OF AN ELLIPTIC INCLUSION WITH A HOMOGENEOUSLY IMPERFECT INTERFACE IN PLANE ELASTOSTATICS

3.1 INTRODUCTION

The present chapter extends the work initiated in Chapter 2 for anti-plane shear elasticity to plane elasticity. In Chapter 2, we considered the problem associated with an elliptic inclusion with a homogeneously imperfect interface embedded within an infinite matrix in anti-plane shear and found the peak interfacial stress to be a non-monotonic function of the parameter h describing the imperfect interface. In addition, it was shown that the influence of the parameter h on the average stress inside the inclusion increases with the aspect ratio of the ellipse.

Of greater theoretical and practical interest, however, is the plane problem. Consequently, in this chapter, we consider plane deformations of an elliptic elastic inclusion embedded within an infinite matrix when the inclusion-matrix interface is again homogeneously imperfect. Using complex variable techniques we obtain infinite series

representations of the corresponding stresses which, when evaluated numerically, again demonstrate how the peak interfacial stress and the average stress inside the inclusion vary with the parameter h describing the imperfect interface (Shen et al, 1999b,d). Perhaps most significant is the fact that our results demonstrate that the peak stress along the interface is again a non-monotonic function of h . This allows us to identify a specific value h^* of the interface parameter which corresponds to maximum peak stress along the inclusion-matrix interface (Shen et al, 1999b,d). We also identify another value (also referred to as h^*) of h which corresponds to maximum peak interfacial strain energy density as defined by Achenbach & Zhu (1990). In each case, we plot the relationship between this new parameter (h^*) and the aspect ratio of the ellipse. This gives significant and valuable information regarding the failure of the interface using two different yet well-established failure criteria (Shen et al, 1999b,d).

3.2 PROBLEM FORMULATION

It is well-known that for plane deformations, the displacement components (u_x, u_y) , stress (or traction) components $(\sigma_{xx}, \sigma_{yy}, \sigma_{xy})$ and the components of the resultant force (F_x, F_y) in \mathcal{R}^2 referred to a Cartesian coordinate system are given in terms of two analytic functions $\phi(z)$ and $\psi(z)$ by (Muskhelishvili, 1963) :

$$2\mu(u_x + iu_y) = [\kappa\phi(z) - z\overline{\phi'(z)} - \overline{\psi(z)}] \quad , \quad (3.1)$$

$$\sigma_{xx} + \sigma_{yy} = 2[\phi'(z) + \overline{\phi'(z)}] \quad , \quad (3.2)$$

$$\sigma_{xx} - i\sigma_{xy} = \phi'(z) + \overline{\phi'(z)} - [z\phi''(z) + \psi'(z)] \quad , \quad (3.3)$$

$$F_x + iF_y = -i[\phi(z) + z\overline{\phi'(z)} + \overline{\psi(z)}]_p^q \quad . \quad (3.4)$$

Here, $z=x+iy$ is the complex coordinate, ν is Poisson's ratio, $\kappa=3-4\nu$ for plane strain and, $\kappa=(3-\nu)/(1+\nu)$ for plane stress and $[]_p^q$ represents the change in the corresponding function in moving from point p to point q along any arc pq .

Across the interface Γ , the boundary displacements and tractions are written in normal-tangential ((n,t) -) coordinates as:

$$2\mu(u_n + iu_t) = [\kappa\phi(z) - z\overline{\phi'(z)} - \overline{\psi(z)}]e^{-i\rho(z)} \quad , \quad (3.5)$$

$$\sigma_{nn} - i\sigma_{nt} = \phi'(z) + \overline{\phi'(z)} - [z\phi''(z) + \psi'(z)]e^{2i\rho(z)} \quad , \quad (3.6)$$

where n is the outward unit normal at $z \in \Gamma$ also represented, in complex form, by $e^{i\rho(z)}$ (where ρ defines the angle between the normal direction n and the positive x -axis). Assume that the elliptic inclusion is bonded to the matrix by a homogeneously imperfect interface. The interface conditions are then given by (Ru, 1998b)

$$[[\sigma_{nn} - i\sigma_{nt}]] = 0 \quad , \quad \sigma_{nn} = h_1(z)[[u_n]] \quad , \quad \sigma_{nt} = h_2(z)[[u_t]] \quad . \quad (3.7)$$

Here h_1 and h_2 are two non-negative interface parameters (basically the 'spring -type constants' of the interface model having dimension of stress divided by length) and $[[*]] = (*)_1 - (*)_2$ denotes the jump across Γ . Since the model of the homogeneously

imperfect interface is based on that of an adhesive layer, the constants h_1 and h_2 represent the degree of bonding at the interface. With this in mind, we mention that the classical case of perfect bonding is obtained from our model in the limiting case when $h_1 = h_2 = \infty$. Similarly, the case of pure sliding can be obtained by setting $h_1 = 0$ and $h_2 = \infty$ while the completely debonded interface can be described by setting $h_1 = h_2 = 0$. Any remaining finite positive values of h_1 and h_2 represent the imperfectly bonded interface considered in this chapter.

The asymptotic conditions at infinity are given by

$$\phi_1(z) \equiv Az + o(1), \quad \psi_1(z) \equiv Bz + o(1), \quad |z| \rightarrow \infty,$$

where A and B are given constants characterizing the remote stress field.

By considering the second and third expressions in Eq. (3.7), we may obtain

$$\sigma_{xx} - i\sigma_{xy} = \frac{h_1 - h_2}{2} [[u_n + iu_t]] + \frac{h_1 + h_2}{2} [[u_n - iu_t]] \quad (3.8)$$

Similarly, from Equation (3.5), we can write the displacements in the form:

$$2[[u_n + iu_t]] = \frac{e^{-i\rho(z)}}{\mu_1} [\kappa_1 \phi_1(z) - z\overline{\phi_1'(z)} - \overline{\psi_1(z)}] - \frac{e^{-i\rho(z)}}{\mu_2} [\kappa_2 \phi_2(z) - z\overline{\phi_2'(z)} - \overline{\psi_2(z)}], \quad \text{on } \Gamma, \quad (3.9)$$

$$2[[u_n - iu_t]] = \frac{e^{i\rho(z)}}{\mu_1} [\kappa_1 \overline{\phi_1(z)} - \bar{z}\phi_1'(z) - \psi_1(z)] - \frac{e^{i\rho(z)}}{\mu_2} [\kappa_2 \overline{\phi_2(z)} - \bar{z}\phi_2'(z) - \psi_2(z)], \text{ on } \Gamma. \quad (3.10)$$

The geometry of the problem is simplified by mapping the ellipse into the unit circle using the mapping function (Muskhelishvili, 1963):

$$z = m(\xi) = \frac{l}{2} \left(R\xi + \frac{1}{R\xi} \right), \quad R\xi = \frac{z}{l} \left\{ 1 + \left[1 - \left(\frac{l}{z} \right)^2 \right]^{\frac{1}{2}} \right\}, \quad \xi = \zeta + i\eta = re^{i\theta}. \quad (3.11)$$

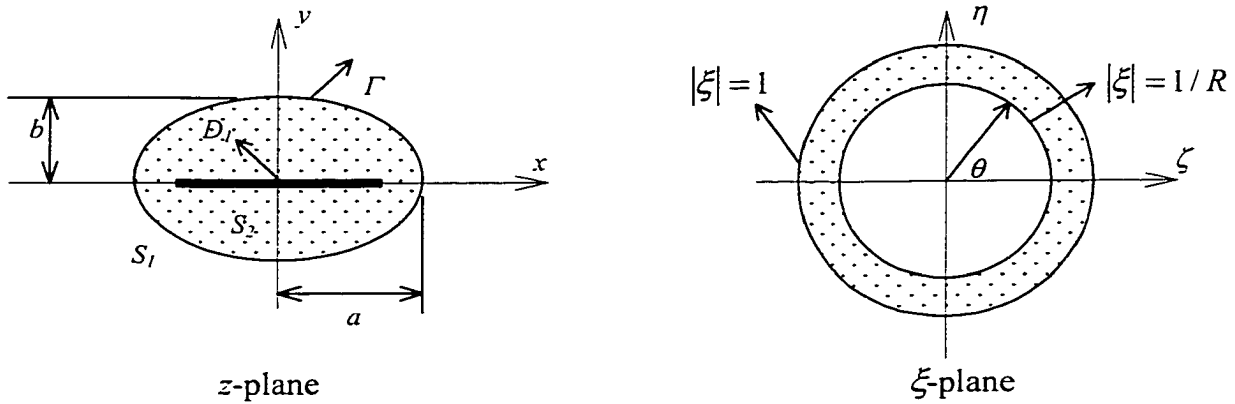


Figure 3.1: Conformal mapping from z -plane to ξ -plane

Here,

$$R = \sqrt{\frac{a+b}{a-b}} > 1, \quad l = \sqrt{a^2 - b^2}$$

We imagine the enclosed region S_2 to be cut along the segment $D_1 = \{(x,0) : -l \leq x \leq l\}$ connecting the foci. This cut may be thought of as an ellipse, which is confocal with Γ but whose minor axis is zero. Hence the cut region in S_2 may be thought of as the limiting case of a region between two confocal ellipses.

If, in the cut ellipse (S_2),

$$\phi_2(z) = \phi_2(\bar{z}), \quad \psi_2(z) = \psi_2(\bar{z}) \quad z \in D_1, \quad (3.12)$$

the functions $\phi_2(z)$, $\psi_2(z)$ will take only one and the same value when the point z approaches the segment D_1 from either side. Consequently, the conditions (3.12) ensure that $\phi_2(z)$, $\psi_2(z)$ are analytic functions throughout the domain S_2 .

For convenience, we write $\phi(\xi) = \phi(m(\xi))$ and $\psi(\xi) = \psi(m(\xi))$ so that in the mapped ξ -plane, the displacements, stresses and resultant forces respectively take the form:

$$2\mu(u_x + iu_y) = \kappa\phi(\xi) - m(\xi)\overline{\Phi(\xi)} - \overline{\psi(\xi)}, \quad (3.13)$$

$$\sigma_{xx} + \sigma_{yy} = 2[\Phi(\xi) + \overline{\Phi(\xi)}], \quad (3.14)$$

$$\sigma_{xx} - i\sigma_{yy} = \Phi(\xi) + \overline{\Phi(\xi)} - \left[\Phi'(\xi) \frac{\overline{m(\xi)}}{m'(\xi)} + \Psi(\xi) \right], \quad (3.15)$$

$$F_x + iF_y = -i[\phi(\xi) + m(\xi)\overline{\Phi(\xi)} + \overline{\psi(\xi)}]_p. \quad (3.16)$$

Here, the prime denotes differentiation with respect to ξ , $\Phi(\xi) = \phi'(\xi)/m'(\xi)$ and $\Psi(\xi) = \psi'(\xi)/m'(\xi)$. Similarly, the condition (3.12) becomes:

$$\phi_2(\xi) = \phi_2(\bar{\xi}), \psi_2(\xi) = \psi_2(\bar{\xi}), \quad \forall \xi: |\xi| = 1/R. \quad (3.17)$$

The condition that tractions be continuous across the interface may be integrated to become a resultant continuity condition of the form:

$$(F_x + iF_y)_1 = (F_x + iF_y)_2. \quad (3.18)$$

For convenience, we introduce an auxiliary stress function $\Omega(\xi)$ such that (see Stagni, 1991)

$$\Omega(\xi) = \frac{\overline{m(1/\bar{\xi})}}{m'(\xi)} \phi'(\xi) + \psi'(\xi). \quad (3.19)$$

Thus, using (3.16), (3.18) and (3.19), continuity of tractions across the interface may be expressed in the form:

$$\phi_1(\xi) + \overline{\Omega_1(\xi)} = \phi_2(\xi) + \overline{\Omega_2(\xi)}, \quad |\xi| = 1. \quad (3.20)$$

The complex potentials $\phi_\alpha(\xi)$ and $\Omega_\alpha(\xi)$ are now expanded into their respective Laurent series in the matrix and in the inclusion as follows:

$$\left. \begin{aligned} \phi_1(\xi) &= \frac{l}{2} AR\xi + \sum_{n=0}^{\infty} A_n \xi^{-(n+1)} \\ \Omega_1(\xi) &= \frac{l}{2} \left(\frac{A}{R} + BR \right) \xi + \sum_{n=0}^{\infty} C_n \xi^{-(n+1)} \end{aligned} \right\}, \quad (3.21)$$

$$\left. \begin{aligned} \phi_2(\xi) &= \sum_{n=0}^{\infty} (S_n \xi^{n+1} + T_n \xi^{-(n+1)}) \\ \Omega_2(\xi) &= \sum_{n=0}^{\infty} (D_n \xi^{n+1} + E_n \xi^{-(n+1)}) \end{aligned} \right\}. \quad (3.22)$$

Note that the constant terms have been omitted since they have no effect on the stress distribution. From (3.19), at infinity, $\Omega_1(\xi) = \frac{l}{2} \left(\frac{A}{R} + BR \right) \xi$. Furthermore, (3.17) combined with (3.21) and (3.22) yields the following relation (see Gong & Meguid, 1993):

$$T_n = \frac{S_n}{R^{2n+2}}, E_n = \frac{D_n}{R^{2n+2}} + (n+1) \frac{S_n}{R^{2n+4}} (R^4 - 1), \quad (n = 0, 1, 2, 3, \dots) \quad (3.23)$$

Consequently, (3.23) allows us to express the coefficients T_n , E_n in terms of the coefficients D_n , S_n . The traction continuity condition (3.20) now becomes:

$$\begin{aligned} & \frac{l}{2} AR\xi + \sum_{n=0}^{\infty} A_n \xi^{-(n+1)} + \frac{l}{2} \left(\frac{\bar{A}}{R} + \bar{B}R \right) \bar{\xi} - \sum_{n=0}^{\infty} \bar{D}_n \bar{\xi}^{n+1} + \sum_{n=0}^{\infty} (\bar{C}_n - \bar{E}_n) \bar{\xi}^{-(n+1)} = \\ & \sum_{n=0}^{\infty} (S_n \xi^{n+1} + T_n \xi^{-(n+1)}) \end{aligned}$$

Noting that $\xi = e^{i\theta}$ on the interface, comparing coefficients, we obtain

$$\bar{C}_0 = -\frac{l}{2}AR + \bar{E}_0 + S_0, \quad A_0 = T_0 + \bar{D}_0 - \frac{l}{2}\left(\frac{\bar{A}}{R} + \bar{B}R\right) \quad (n=0) \quad (3.24)$$

$$\bar{C}_n = \bar{E}_n + S_n, \quad C_n = E_n + \bar{S}_n \quad (n=1,2,3,\dots) \quad (3.25)$$

$$A_n = T_n + \bar{D}_n, \quad \bar{A}_n = \bar{T}_n + D_n \quad (n=1,2,3,\dots) \quad (3.26)$$

Thus the coefficients A_n, C_n can be expressed in terms of the coefficients D_n, S_n . The only unknown coefficients are therefore D_n, S_n . These can be obtained from the interface condition (3.8) as follows.

In the mapped ξ -plane, noting the following relations from England (1971),

$$e^{i2\rho(z)} = \frac{\xi^2 m'(\xi)}{r^2 \overline{m'(\xi)}}, \quad e^{i\rho(z)} = \frac{\xi m'(\xi)}{r |m'(\xi)|}, \quad e^{-i\rho(z)} = \frac{\bar{\xi} \overline{m'(\xi)}}{r |m'(\xi)|},$$

equations (3.9) and (3.10) become

$$2[[u_n + iu_t]] = \frac{\bar{\xi} \overline{m'(\xi)}}{|\xi| |m'(\xi)|} \left\{ \frac{1}{\mu_1} [\kappa_1 \phi_1(\xi) - \overline{\Omega_1(\xi)}] - \frac{1}{\mu_2} [\kappa_2 \phi_2(\xi) - \overline{\Omega_2(\xi)}] \right\}, \quad \text{on } \Gamma, \quad (3.27)$$

$$2[[u_n - iu_t]] = \frac{\xi m'(\xi)}{|\xi| |m'(\xi)|} \left\{ \frac{1}{\mu_1} [\kappa_1 \overline{\phi_1(\xi)} - \Omega_1(\xi)] - \frac{1}{\mu_2} [\kappa_2 \overline{\phi_2(\xi)} - \Omega_2(\xi)] \right\}, \quad \text{on } \Gamma. \quad (3.28)$$

Similarly, (3.6) becomes

$$\begin{aligned} \sigma_{nn} - i\sigma_{nt} &= \frac{\phi'(\xi)}{m'(\xi)} + \frac{\overline{\phi'(\xi)}}{m'(\xi)} - \left\{ \frac{1}{m(\xi)} \frac{d}{d\xi} \left[\frac{\phi'(\xi)}{m'(\xi)} \right] \frac{1}{m'(\xi)} + \frac{\psi'(\xi)}{m'(\xi)} \right\} \xi^2 \frac{m'(\xi)}{m'(\xi)} = \\ &= \frac{\phi'(\xi)}{m'(\xi)} + \frac{\overline{\phi'(\xi)}}{m'(\xi)} - \left\{ \frac{\phi''(\xi)m'(\xi) - \phi'(\xi)m''(\xi)}{[m'(\xi)]^2} \frac{\overline{m(\xi)}}{m'(\xi)} + \frac{\psi'(\xi)}{m'(\xi)} \right\} e^{2i\theta} \quad \text{on } \Gamma. \end{aligned} \quad (3.29)$$

Multiplying the above expression by the (non-vanishing) factor $[m'(\xi)]^2 \overline{m'(\xi)}$, and eliminating $\psi'(\xi)$ using (3.19), we obtain

$$[m'(\xi)]^2 \overline{m'(\xi)} [\sigma_{nn} - i\sigma_{nt}] = [m'(\xi)]^2 [\overline{\phi'(\xi)} - e^{2i\theta} \Omega'(\xi)] \quad (3.30)$$

Consequently, from (3.27) - (3.29), the interface condition (3.8) becomes

$$\begin{aligned} [m'(\xi)]^2 [\overline{\phi'(\xi)} - e^{2i\theta} \Omega'(\xi)] &= \\ &= \frac{h_1 - h_2}{4} |m'(\xi)| \overline{m'(\xi)} m'(\xi) e^{-i\theta} \left\{ \frac{1}{\mu_1} [\kappa_1 \phi_1(\xi) - \overline{\Omega_1(\xi)}] - \frac{1}{\mu_2} [\kappa_2 \phi_2(\xi) - \overline{\Omega_2(\xi)}] \right\} + \\ &+ \frac{h_1 + h_2}{4} |m'(\xi)| [m'(\xi)]^2 e^{i\theta} \left\{ \frac{1}{\mu_1} [\kappa_1 \overline{\phi_1(\xi)} - \Omega_1(\xi)] - \frac{1}{\mu_2} [\kappa_2 \overline{\phi_2(\xi)} - \Omega_2(\xi)] \right\} \end{aligned}$$

Using (3.11), we can eliminate ξ from the right-hand side of this expression and obtain:

$$\begin{aligned}
& [m'(\xi)]^2 [\overline{\phi'(\xi)} - e^{2i\theta} \Omega'(\xi)] = \\
& m' \sqrt{1 + b^* \sin^2 \theta} \frac{b}{4} \left\{ (h_1 - h_2) \overline{m'} e^{-i\theta} \left[\frac{1}{\mu_1} [\kappa_1 \phi_1 - \overline{\Omega_1}] - \frac{1}{\mu_2} [\kappa_2 \phi_2 - \overline{\Omega_2}] \right] + \right. \\
& \left. (h_1 + h_2) m' e^{i\theta} \left[\frac{1}{\mu_1} [\kappa_1 \overline{\phi_1} - \Omega_1] - \frac{1}{\mu_2} [\kappa_2 \overline{\phi_2} - \Omega_2] \right] \right\} \quad z \in \Gamma
\end{aligned} \tag{3.31}$$

where $b^* = (a^2 - b^2)/b^2$. From (3.21)-(3.26), noting that $\xi = e^{i\theta}$ on the interface, we obtain the final form of the interface condition (3.8):

$$\begin{aligned}
& [m'(\xi)]^2 [\overline{\phi'(\xi)} - e^{2i\theta} \Omega'(\xi)] = \\
& m' \sqrt{1 + b^* \sin^2 \theta} \frac{Rbl}{8} \{ (h_1 - h_2) Q_n + (h_1 + h_2) \overline{Q_n} \} \quad z \in \Gamma \tag{3.32}
\end{aligned}$$

where

$$\left. \begin{aligned}
& Q_n = g_1 - g_2 e^{2i\theta} - g_3 e^{-2i\theta} + \sum_{n=0}^{\infty} M_n e^{-i(n+2)\theta} - \sum_{n=0}^{\infty} N_n e^{in\theta} - \\
& \sum_{n=0}^{\infty} M_n R^{-2} e^{-in\theta} + \sum_{n=0}^{\infty} N_n R^{-2} e^{i(n+2)\theta} \\
& g_1 = AR\Lambda_1 \frac{l}{2} + \frac{\Lambda_1 E}{R^2}, g_2 = \frac{lA\Lambda_1}{2R}, g_3 = \Lambda_1 E, M_n = (\Lambda_2 \overline{D}_n + \Lambda_3 T_n) \\
& N_n = (\Lambda_4 \overline{E}_n + \Lambda_5 S_n), \Lambda_1 = \frac{1}{\mu_1} (1 + \kappa_1), \Lambda_2 = \frac{\kappa_1}{\mu_1} + \frac{1}{\mu_2}, \Lambda_3 = \frac{\kappa_1}{\mu_1} - \frac{\kappa_2}{\mu_2} \\
& \Lambda_4 = \frac{1}{\mu_1} - \frac{1}{\mu_2}, \Lambda_5 = \frac{1}{\mu_1} + \frac{\kappa_2}{\mu_2}, E = \frac{l}{2} \left(\frac{\overline{A}}{R} + \overline{BR} \right)
\end{aligned} \right\} \tag{3.33}$$

From (3.11) and (3.21)-(3.26), the interface condition (3.32) becomes

$$\left\{ d_0 + d_1 e^{-i\theta} + d_2 e^{i\theta} + d_3 e^{-2i\theta} + d_4 e^{2i\theta} + d_5 e^{-3i\theta} + d_6 e^{-4i\theta} + \sum_{n=0}^{\infty} U_n e^{i(n+2)\theta} + \sum_{n=0}^{\infty} V_n e^{-i(n+4)\theta} \right\} \\ = \Lambda \sqrt{1 + b^* \sin^2 \theta} \times \\ \left[+ \sum_{n=0}^{\infty} P_n e^{i(n+2)\theta} + \sum_{n=0}^{\infty} O_n e^{-i(n+4)\theta} + c_0 + c_1 e^{-i\theta} + c_2 e^{i\theta} + f_2 e^{i2\theta} + c_3 e^{-i2\theta} + c_4 e^{-i3\theta} + f_4 e^{-i4\theta} \right] \quad (3.34)$$

where

$$\left. \begin{aligned} U_n &= 2l^2 \left[-R^4 (\bar{T}_n + D_n)(n+1) + 2R^2 (\bar{T}_{n+2} + D_{n+2})(n+3) - (\bar{T}_{n+4} + D_{n+4})(n+5) \right] \\ V_n &= 2l^2 \left[-2R^2 (T_{n+1} + \bar{D}_{n+1})(n+2) + 2(T_{n+3} + \bar{D}_{n+3})(n+4) + \right. \\ &\quad \left. R^4 (E_{n+4} + \bar{S}_{n+4})(n+5) - 2R^2 (E_{n+2} + \bar{S}_{n+2})(n+3) + \right. \\ &\quad \left. (E_n + \bar{S}_n)(n+1) + 2R^2 (T_n + \bar{D}_n)(n+1) + (T_{n+2} + \bar{D}_{n+2})(n+3) \right] \end{aligned} \right\} \quad (3.35)$$

$$\left. \begin{aligned} P_n &= L_{n+4} + G_{n+2} + J_n, O_n = F_{n+2} - H_{n+4} - K_n, \\ F_n &= 2(h_1 + h_2)R^{-2}\bar{N}_n + (h_1 - h_2)(1 + R^{-4})M_n, \\ G_n &= 2(h_1 + h_2)R^{-2}\bar{M}_n + (h_1 - h_2)(1 + R^{-4})N_n, \\ H_n &= (h_1 + h_2)\bar{N}_n + (h_1 - h_2)R^{-2}M_n, J_n = (h_1 + h_2)\bar{M}_n + (h_1 - h_2)R^{-2}N_n, \\ K_n &= [(h_1 + h_2)R^{-2}\bar{N}_n + (h_1 - h_2)M_n]R^{-2}, \\ L_n &= [(h_1 + h_2)R^{-2}\bar{M}_n + (h_1 - h_2)N_n]R^{-2}, \\ f_1 &= (h_1 + h_2)(\bar{g}_1 - \bar{g}_3 R^{-2}) + (h_1 - h_2)(g_1 + g_2 R^{-2}), \\ f_2 &= (h_1 + h_2)\bar{g}_3 - (h_1 - h_2)g_2, \\ f_3 &= (h_1 + h_2)(-\bar{g}_2 - \bar{g}_1 R^{-2}) + (h_1 - h_2)(g_3 - g_1 R^{-2}), \\ f_4 &= [(h_1 + h_2)\bar{g}_2 - (h_1 - h_2)g_3]R^{-2}, \\ c_0 &= f_1 + L_2 + G_0 + H_0, c_1 = L_1 + H_1, c_2 = L_3 + G_1, \\ c_3 &= L_0 + F_0 + H_2 + f_3, c_4 = F_1 + H_3, \end{aligned} \right\} \quad (3.36)$$

$$\begin{aligned}
\Lambda &= \frac{b(a+b)^3}{2(a-b)}, \\
d_0 &= -2l^3 RA + 4l^2 R^2 (\bar{T}_0 + D_0) - 6l^2 (\bar{T}_2 + D_2) + 2l^2 R^4 (E_0 + \bar{S}_0) \\
d_1 &= 2l^3 R^3 A - 4l^2 (\bar{T}_1 + D_1) + 4l^2 (T_0 + \bar{D}_0 - E) + 4l^2 R^4 (E_1 + \bar{S}_1) \\
d_2 &= -2l^3 RA + 8l^2 R^2 (\bar{T}_1 + D_1) - 8l^2 (\bar{T}_3 + D_3) \\
d_3 &= -2l^3 R^3 A - 2l^2 (\bar{T}_0 + D_0) + 4l^2 (T_0 + \bar{D}_0) - 4l^2 E + 8l^2 (T_1 + \bar{D}_1) + \\
&6l^2 R^4 (E_2 + \bar{S}_2) - 4l^2 R^2 (E_0 + \bar{S}_0) \\
d_4 &= 0 \\
d_5 &= -4l^2 R^2 (T_0 + \bar{D}_0 - E) + 8l^2 (T_1 + \bar{D}_1) + 8l^2 R^4 (E_3 + \bar{S}_3) - 8l^2 R^2 (E_1 + \bar{S}_1) \\
&+ 12l^2 (T_2 + \bar{D}_2) \\
d_6 &= -4l^2 R^2 E
\end{aligned} \tag{3.37}$$

In the above expressions, the coefficients T_i and E_i can be written in terms of S_i and D_i by using (3.23). Hence, the only remaining unknown coefficients are again S_i and D_i .

Next, we employ a method similar to that used in Chapter 2 by substituting the following expression (Appendix) into (3.34):

$$\begin{aligned}
\sqrt{1 + b^* \sin^2 \theta} &= \sum_{k=-\infty}^{\infty} I_{2k} e^{i2k\theta} \approx \sum_{k=0}^{M-1} I_{2k} (e^{i2k\theta} + e^{-i2k\theta}) + I_{2M} \frac{e^{i2M\theta} + e^{-i2M\theta} - \eta(e^{i2(M-1)\theta} + e^{i2(1-M)\theta})}{1 + \frac{1}{R^4} - \frac{e^{i2\theta} + e^{-i2\theta}}{R^2}} \\
&= \sum_{k=0}^{M-1} I_{2k} (e^{i2k\theta} + e^{-i2k\theta}) + I_{2M} \frac{e^{i2M\theta} + e^{-i2M\theta} - \eta(e^{i2(M-1)\theta} + e^{i2(1-M)\theta})}{1 + \eta^2 - \eta(e^{i2\theta} + e^{-i2\theta})} \\
&= \sum_{k=0}^{M-1} I_{2k} (e^{i2k\theta} + e^{-i2k\theta}) + I_{2M} \frac{e^{i2M\theta} + e^{-i2M\theta} - \eta(e^{i2(M-1)\theta} + e^{i2(1-M)\theta})}{x - \eta(e^{i2\theta} + e^{-i2\theta})}
\end{aligned}$$

We obtain

$$\begin{aligned}
& \left[x_2 e^{-i\theta} + x_4 e^{-2i\theta} + x_6 e^{-3i\theta} + x_8 e^{-4i\theta} - x_{10} e^{-5i\theta} - x_{11} e^{-6i\theta} + x \sum_{n=0}^{\infty} V_n e^{-i(n+4)\theta} - \eta \sum_{n=0}^{\infty} V_n e^{-i(n+2)\theta} - \eta \sum_{n=0}^{\infty} V_n e^{-i(n+6)\theta} \right] \\
& + x_1 + \left[x_3 e^{i\theta} + x_5 e^{2i\theta} - x_7 e^{3i\theta} - x_9 e^{4i\theta} + x \sum_{n=0}^{\infty} U_n e^{i(n+2)\theta} - \eta \sum_{n=0}^{\infty} U_n e^{i(n+4)\theta} - \eta \sum_{n=0}^{\infty} U_n e^{in\theta} \right] = \\
& \Lambda \left\{ \left[\sum_{k=0}^{M-1} I_{2k} (e^{i2k\theta} + e^{-i2k\theta}) (x - \eta (e^{i2\theta} + e^{-i2\theta})) + I_{2M} (e^{i2M\theta} + e^{-i2M\theta} - \eta (e^{i2(M-1)\theta} + e^{i2(1-M)\theta})) \right] \right. \\
& \left. \left[\sum_{n=0}^{\infty} P_n e^{i(n+2)\theta} + \sum_{n=0}^{\infty} O_n e^{-i(n+4)\theta} + c_0 + c_1 e^{-i\theta} + c_2 e^{i\theta} + f_2 e^{i2\theta} + c_3 e^{-i2\theta} + c_4 e^{-i3\theta} + f_4 e^{-i4\theta} \right] \right\} \\
& \tag{3.38}
\end{aligned}$$

where

$$\left. \begin{aligned}
& \eta = 1/R^2, x = 1 + \eta^2, x_1 = xd_0 - \eta d_3 - \eta d_4, x_2 = xd_1 - \eta d_5 - \eta d_2, \\
& x_3 = xd_2 - \eta d_1, x_4 = xd_3 - \eta d_6 - \eta d_0, x_5 = xd_4 - \eta d_0, x_6 = xd_5 - \eta d_1, \\
& x_7 = \eta d_2, x_8 = xd_6 - \eta d_3, x_9 = \eta d_4 = 0, x_{10} = \eta d_5, x_{11} = \eta d_6
\end{aligned} \right\}. \tag{3.39}$$

Furthermore, by equating coefficients of $e^{in\theta}$ in (3.38), we finally obtain

$$\sum_{k=0}^M W_{nk} I_{2k} = Q_n \tag{3.40}$$

Hence W_{nk} and Q_n are finally related to coefficients S_i and D_i . For example, for $M=5$ and

$e^{i3\theta}$, we obtain

$$\left. \begin{aligned}
W_{30} &= xP_1 - 2\eta P_3 - c_2\eta, W_{31} = xP_3 - 2\eta P_1 - \eta P_5 + c_2x - c_1\eta \\
W_{32} &= xP_5 - \eta P_3 - \eta P_7 - c_4\eta + c_1x - c_2\eta \\
W_{33} &= xP_7 - \eta P_5 - \eta P_9 + c_4x - c_1\eta - \eta O_1 \\
W_{34} &= xP_9 - \eta P_7 - \eta P_{11} - c_4\eta + xO_1 - \eta O_3 \\
W_{35} &= P_{11} - \eta P_9 - \eta O_1 + O_3, Q_3 = \frac{-x_7 + xU_1 - \eta U_3}{\Lambda}
\end{aligned} \right\}. \quad (3.41)$$

The relationship between above coefficients and S_i and D_i can be expressed as follows:

$$\begin{aligned}
P_n &= L_{n+4} + G_{n+2} + J_n = \left[(h_1 + h_2)R^{-2}\bar{M}_{n+4} + (h_1 - h_2)N_{n+4} \right] R^{-2} + \\
&2(h_1 + h_2)R^{-2}\bar{M}_{n+2} + (h_1 - h_2)(1 + R^{-4})N_{n+2} + (h_1 + h_2)\bar{M}_n + (h_1 - h_2)R^{-2}N_n \\
&= \left[(h_1 + h_2)R^{-2}(\Lambda_2 D_{n+4} + \Lambda_3 \bar{T}_{n+4}) + (h_1 - h_2)(\Lambda_4 \bar{E}_{n+4} + \Lambda_5 S_{n+4}) \right] R^{-2} + \\
&2(h_1 + h_2)R^{-2}(\Lambda_2 D_{n+2} + \Lambda_3 \bar{T}_{n+2}) + (h_1 - h_2)(1 + R^{-4})(\Lambda_4 \bar{E}_{n+2} + \Lambda_5 S_{n+2}) \\
&+ (h_1 + h_2)(\Lambda_2 D_n + \Lambda_3 \bar{T}_n) + (h_1 - h_2)R^{-2}(\Lambda_4 \bar{E}_n + \Lambda_5 S_n) \\
&= \left[(h_1 + h_2)R^{-2} \left(\Lambda_2 D_{n+4} + \Lambda_3 \frac{\bar{S}_{n+4}}{R^{2(n+4)+2}} \right) + (h_1 - h_2) \left(\Lambda_4 \left(\frac{\bar{D}_{n+4}}{R^{2(n+4)+2}} + (n+5) \frac{\bar{S}_{n+4}}{R^{2(n+4)+4}} \right) \right. \right. \\
&\quad \left. \left. + 2(h_1 + h_2)R^{-2} \left(\Lambda_2 D_{n+2} + \Lambda_3 \frac{\bar{S}_{n+2}}{R^{2(n+2)+2}} \right) + (h_1 - h_2)(1 + R^{-4}) \left(\Lambda_4 \left(\frac{\bar{D}_{n+2}}{R^{2(n+2)+2}} + (n+3) \frac{\bar{S}_{n+2}}{R^{2(n+2)+4}} \right) \right. \right. \right. \\
&\quad \left. \left. + (h_1 + h_2) \left(\Lambda_2 D_n + \Lambda_3 \frac{\bar{S}_n}{R^{2n+2}} \right) + (h_1 - h_2)R^{-2} \left(\Lambda_4 \left(\frac{\bar{D}_n}{R^{2n+2}} + (n+1) \frac{\bar{S}_n}{R^{2n+4}} (R^4 - 1) \right) + \Lambda_5 S_n \right) \right) \right]
\end{aligned}$$

$$\begin{aligned}
O_n &= F_{n+2} - H_{n+4} - K_n = 2(h_1 + h_2)R^{-2}\bar{N}_{n+2} + (h_1 - h_2)(1 + R^{-4})M_{n+2} - \\
&(h_1 + h_2)\bar{N}_{n+4} - (h_1 - h_2)R^{-2}M_{n+4} - \left[(h_1 + h_2)R^{-2}\bar{N}_n + (h_1 - h_2)M_n \right] R^{-2} \\
&= 2(h_1 + h_2)R^{-2}(\Lambda_4 E_{n+2} + \Lambda_5 \bar{S}_{n+2}) + (h_1 - h_2)(1 + R^{-4})(\Lambda_2 \bar{D}_{n+2} + \Lambda_3 T_{n+2}) \\
&- (h_1 + h_2)(\Lambda_4 E_{n+4} + \Lambda_5 \bar{S}_{n+4}) - (h_1 - h_2)R^{-2}(\Lambda_2 \bar{D}_{n+4} + \Lambda_3 T_{n+4}) - \\
&\left[(h_1 + h_2)R^{-2}(\Lambda_4 E_n + \Lambda_5 \bar{S}_n) + (h_1 - h_2)(\Lambda_2 \bar{D}_n + \Lambda_3 T_n) \right] R^{-2} \\
&= 2(h_1 + h_2)R^{-2} \left(\Lambda_4 \left(\frac{D_{n+2}}{R^{2(n+2)+2}} + (n+3) \frac{S_{n+2}}{R^{2(n+2)+4}} (R^4 - 1) \right) + \Lambda_5 \bar{S}_{n+2} \right) \\
&+ (h_1 - h_2)(1 + R^{-4}) \left(\Lambda_2 \bar{D}_{n+2} + \Lambda_3 \frac{S_{n+2}}{R^{2(n+2)+2}} \right) - \\
&(h_1 + h_2) \left(\Lambda_4 \left(\frac{D_{n+4}}{R^{2(n+4)+2}} + (n+5) \frac{S_{n+4}}{R^{2(n+4)+4}} (R^4 - 1) \right) + \Lambda_5 \bar{S}_{n+4} \right) - \\
&(h_1 - h_2)R^{-2} \left(\Lambda_2 \bar{D}_{n+4} + \Lambda_3 \frac{S_{n+4}}{R^{2(n+4)+2}} \right) - \\
&\left[(h_1 + h_2)R^{-2} \left(\Lambda_4 \left(\frac{D_n}{R^{2n+2}} + (n+1) \frac{S_n}{R^{2n+4}} (R^4 - 1) \right) + \Lambda_5 \bar{S}_n \right) + (h_1 - h_2) \left(\Lambda_2 \bar{D}_n + \Lambda_3 \frac{S_n}{R^{2n+2}} \right) \right] R^{-2}
\end{aligned}$$

$$\begin{aligned}
U_n &= 2l^2 \left[-R^4(\bar{T}_n + D_n)(n+1) + 2R^2(\bar{T}_{n+2} + D_{n+2})(n+3) - (\bar{T}_{n+4} + D_{n+4})(n+5) \right] = \\
&2l^2 \left[-R^4 \left(\frac{\bar{S}_n}{R^{2n+2}} + D_n \right) (n+1) + 2R^2 \left(\frac{\bar{S}_{n+2}}{R^{2(n+2)+2}} + D_{n+2} \right) (n+3) - \left(\frac{\bar{S}_{n+4}}{R^{2(n+4)+2}} + D_{n+4} \right) (n+5) \right] \\
V_n &= 2l^2 \left[-2R^2(T_{n+1} + \bar{D}_{n+1})(n+2) + 2(T_{n+3} + \bar{D}_{n+3})(n+4) + R^4(E_{n+4} + \bar{S}_{n+4})(n+5) \right. \\
&\left. - 2R^2(E_{n+2} + \bar{S}_{n+2})(n+3) + (E_n + \bar{S}_n)(n+1) + 2R^2(T_n + \bar{D}_n)(n+1) + (T_{n+2} + \bar{D}_{n+2})(n+3) \right] = \\
&2l^2 \left[-2R^2 \left(\frac{S_{n+1}}{R^{2(n+1)+2}} + \bar{D}_{n+1} \right) (n+2) + 2 \left(\frac{S_{n+3}}{R^{2(n+3)+2}} + \bar{D}_{n+3} \right) (n+4) + R^4 \left(\frac{D_{n+4}}{R^{2(n+4)+2}} + \right. \right. \\
&\left. \left. (n+5) \frac{S_{n+4}}{R^{2(n+4)+4}} (R^4 - 1) + \bar{S}_{n+4} \right) (n+5) - 2R^2 \left(\frac{D_{n+2}}{R^{2(n+2)+2}} + (n+3) \frac{S_{n+2}}{R^{2(n+2)+4}} (R^4 - 1) + \bar{S}_{n+2} \right) (n+3) \right. \\
&\left. + \left(\frac{D_n}{R^{2n+2}} + (n+1) \frac{S_n}{R^{2n+4}} (R^4 - 1) + \bar{S}_n \right) (n+1) + 2R^2 \left(\frac{S_n}{R^{2n+2}} + \bar{D}_n \right) (n+1) + \left(\frac{S_{n+2}}{R^{2(n+2)+2}} + \bar{D}_{n+2} \right) (n+3) \right]
\end{aligned}$$

Depending on the level of accuracy required, we may select different values of M in Eq.(3.40) corresponding to a set of M linear equations and finally obtain the coefficients S_i and D_i .

3.3 NUMERICAL EXAMPLES AND DISCUSSION

3.3.1 Interfacial Stress

In the present thesis, the interfacial stress is composed of two parts: σ_{normal} , the component of stress along the normal direction to the interface; $\sigma_{\text{tangential}}$, the component of stress along the tangential direction to the interface.

Let $b = 1$ and consider the case of an epoxy matrix surrounding a glass inclusion. The material properties of the matrix and the inclusion are described by (Huang and Hu 1995):

$$E_1 = 2.76 \text{ Gpa}, \nu_1 = 0.35, \mu_1 = 1.02 \text{ Gpa}$$

$$E_2 = 72.4 \text{ Gpa}, \nu_2 = 0.2, \mu_2 = 30.17 \text{ Gpa},$$

where, E is Young's modulus and ν is Poisson's ratio.

In practice, the imperfect interface parameter h is rendered dimensionless by division by μ_1/b , where μ_1 is the shear modulus of the matrix, and b is the minor axis of the ellipse. In this calculation, two cases are considered, $h_1=h_2$ and $h_1=3h_2$ (Basically, the imperfect interface parameters are related to Young's modulus and Shear's modulus, therefore, it is reasonable to assume $h_1=3h_2$, see Hashin, 1991b). The results from these two cases are compared and discussed.

In what follows, we present results for three different ranges of the aspect ratio a/b . In each case, the number of coefficients in the corresponding series is chosen so that the

error in the numerical calculations is maintained below 1%. This is achieved simply by calculating an increasing sequence of partial sums from each of the (uniformly convergent) infinite series representations and noting the minimum number of coefficients required to ensure that the difference between any two subsequent partial sums is less than 1%.

CASE 1 When $1 < a/b \leq 3.5$, only the coefficients $S_0(D_0)$, $S_1(D_1)$ and $S_2(D_2)$ are necessary to achieve the desired accuracy. From (3.22) and (3.23), considering (3.11), it is easy to find ϕ_2 and Ω_2 expressed in terms of $S_0(D_0)$, $S_1(D_1)$ and $S_2(D_2)$. Furthermore, ψ_2 can be obtained from (3.19). For example, in the present case

$$\phi_2(\xi) \equiv -\frac{2S_1}{R^2} + \left(\frac{S_0}{R} - \frac{3S_2}{R^3}\right)\left(\frac{2z}{l}\right) + \left(\frac{S_1}{R^2}\right)\left(\frac{2z}{l}\right)^2 + \left(\frac{S_2}{R^3}\right)\left(\frac{2z}{l}\right)^3 \quad (3.42)$$

Once ϕ_2 and ψ_2 are obtained, we can calculate the stress distribution inside the inclusion. In Figures 3.2 and 3.3, the stress distribution along the interface (normal and tangential directions) in the two cases $h_1=h_2$ and $h_1=3h_2$ is plotted for the value $a/b=3.5$ and different values of the parameter h . When $h=100$, the local stresses reach maximum values for both cases. The present computations also indicate that there is no significant difference between the cases $h_1=h_2$ and $h_1=3h_2$. Hence, for practical inclusion (structural) design, to satisfy the basic requirements we need only consider the case $h_1=h_2$.

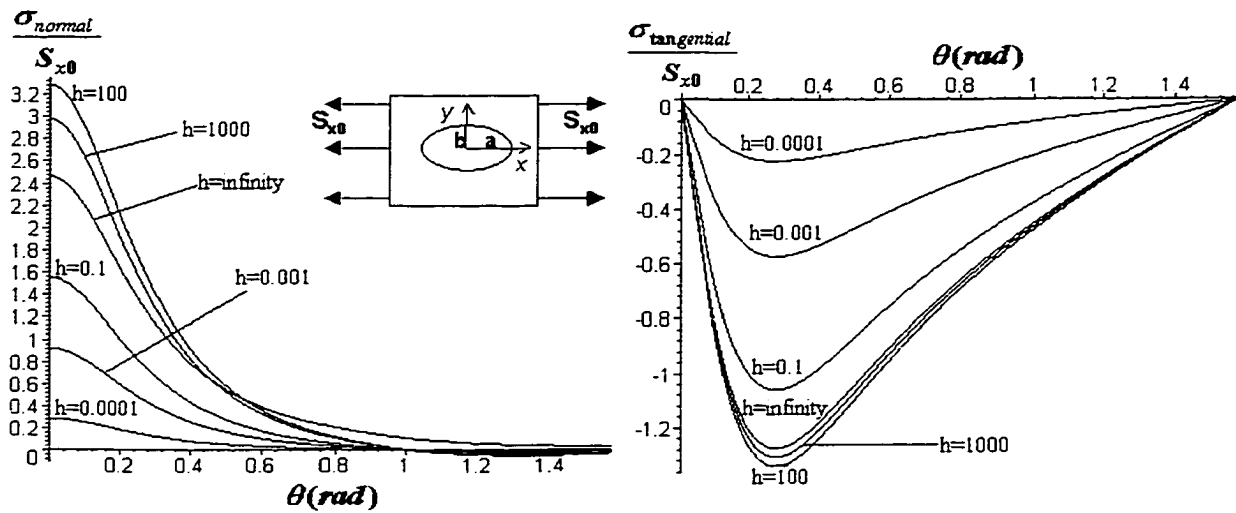


Figure 3.2: Normal and tangential stresses along the interface with $a/b=3.5$ and $h_1 = h_2 = h$ when the remote stress is S_{x0} .

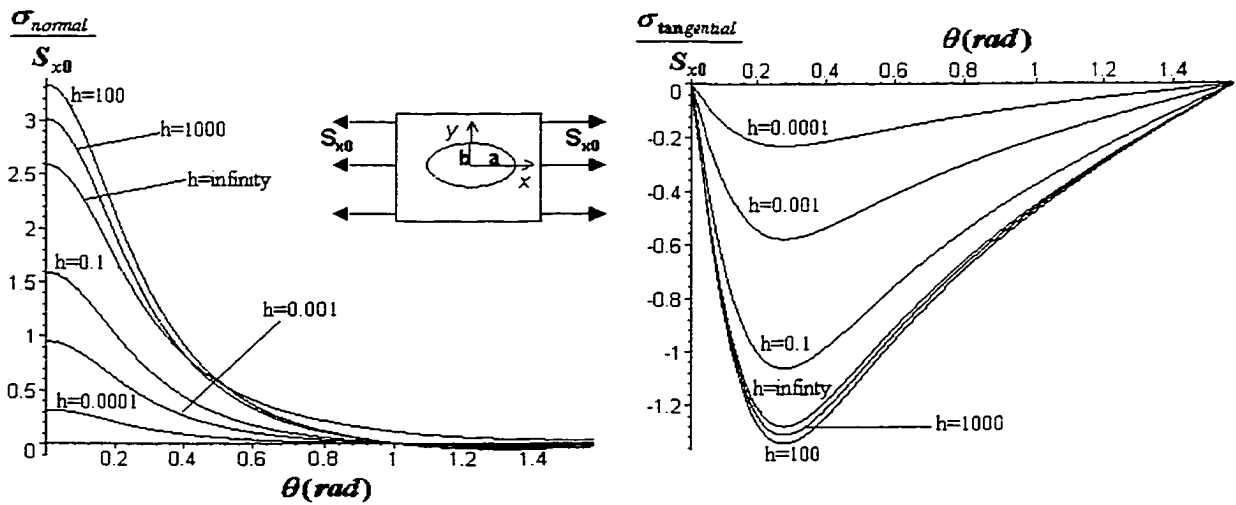


Figure 3.3: Normal and tangential stresses along the interface with $a/b = 3.5$ and $h_1 = 3h_2 = h$ when the remote stress is S_{x0} .

CASE 2 When $3.5 < a/b \leq 7$, only the coefficients $S_0(D_0)$, $S_1(D_1)$, $S_2(D_2)$ and $S_3(D_3)$ are necessary to achieve the desired accuracy. As above, we can obtain ϕ_2 , Ω_2 and ψ_2 expressed in terms $S_0(D_0)$, $S_1(D_1)$, $S_2(D_2)$ and $S_3(D_3)$. The corresponding interfacial stress distributions are presented in Figures 3.4 and 3.5.

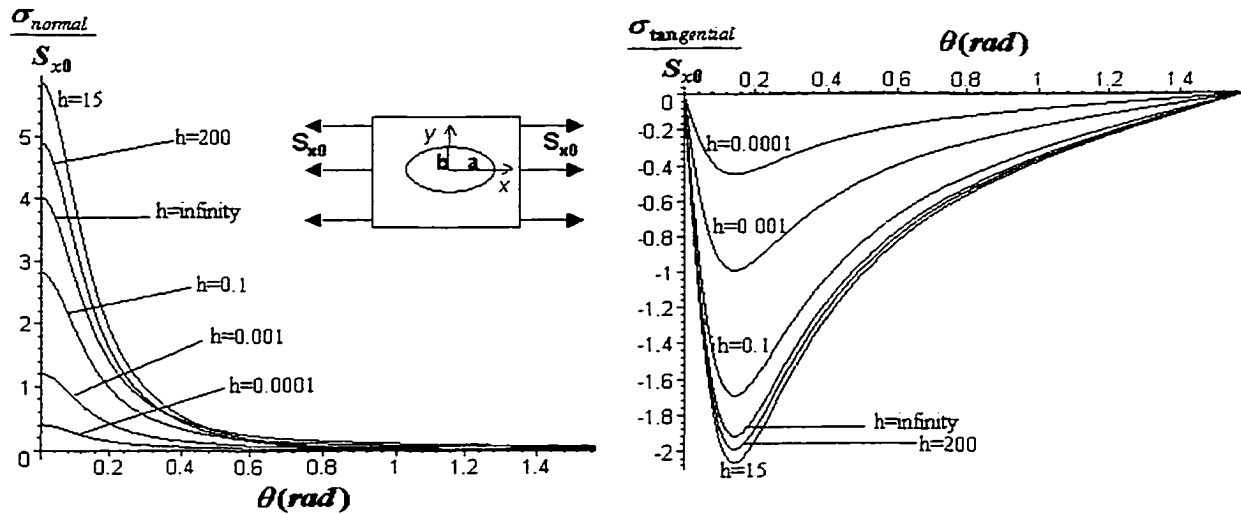


Figure 3.4: Normal and tangential stresses along the interface with $a/b = 7$ and $h_1 = h_2 = h$ when the remote stress is S_{x0} .

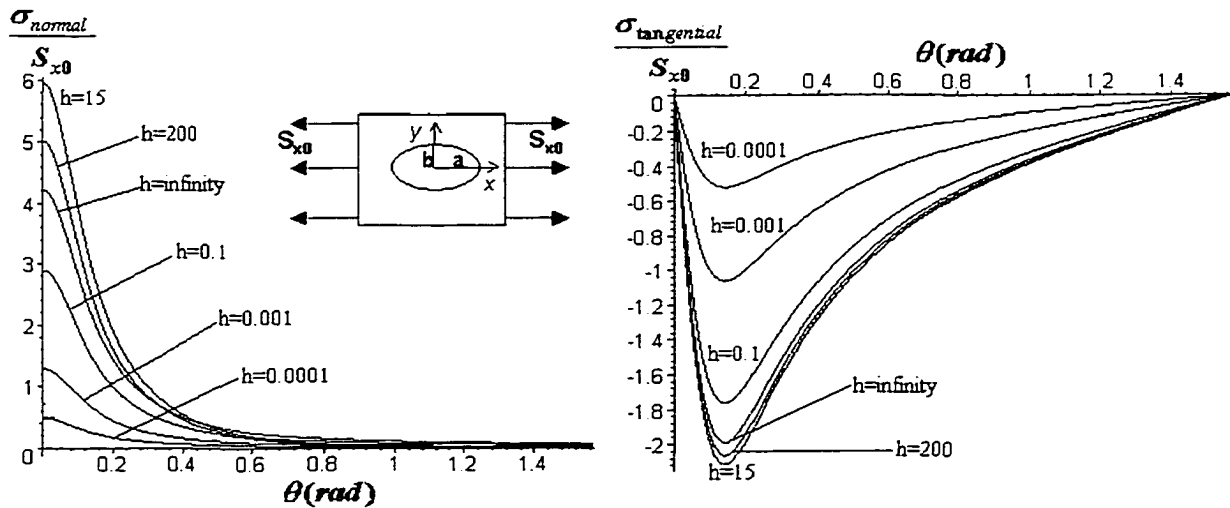


Figure 3.5: Normal and tangential stresses along the interface with $a/b = 7$ and $h_1 = 3h_2 = h$ when the remote stress is S_{x0} .

CASE 3 When $7 < a/b \leq 10$, only the coefficients $S_0(D_0)$, $S_1(D_1)$, $S_2(D_2)$, $S_3(D_3)$ and $S_4(D_4)$ are necessary to achieve the desired accuracy. Again, we can obtain ϕ_2 , Ω_2 and ψ_2 expressed in terms of $S_0(D_0)$, $S_1(D_1)$, $S_2(D_2)$, $S_3(D_3)$ and $S_4(D_4)$. The corresponding interfacial stress distributions are presented in Figures 3.6 and 3.7.

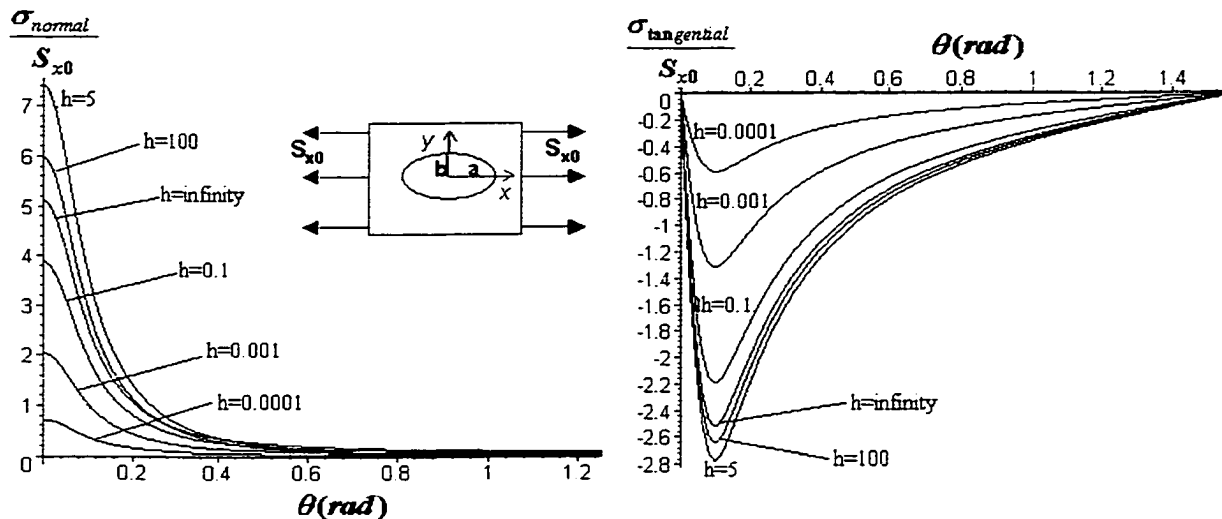


Figure 3.6: Normal and tangential stresses along the interface with $a/b = 10$ and $h_1 = h_2 = h$ when the remote stress is S_{x0} .

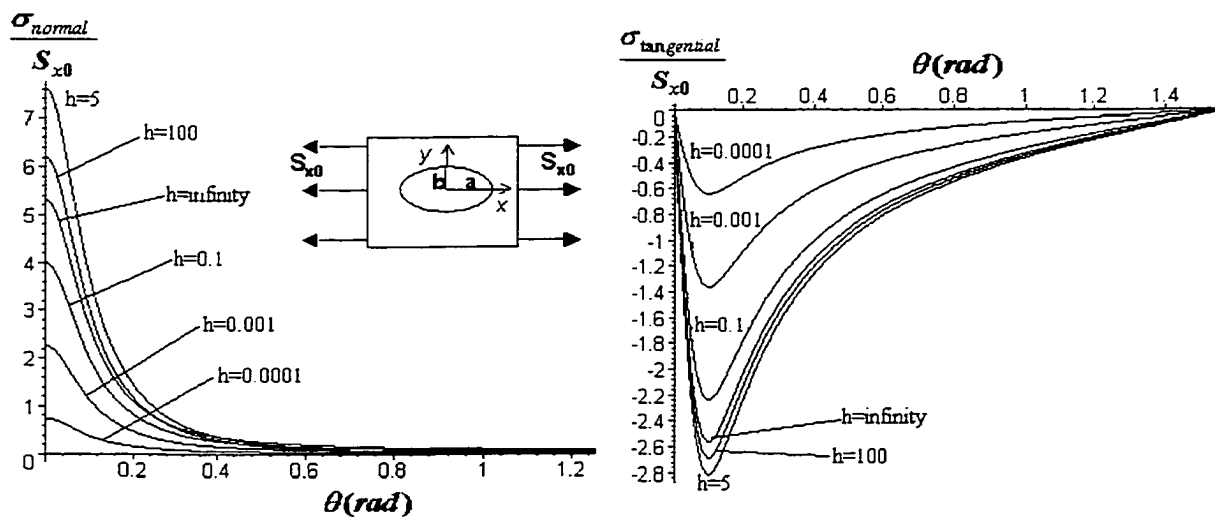


Figure 3.7: Normal and tangential stresses along the interface with $a/b = 10$ and $h_1 = 3h_2 = h$ when the remote stress is S_{x0} .

It is noted that for values $a/b > 10$ of the aspect ratio, the procedure is similar although a much larger number of coefficients is required to evaluate the corresponding series to the desired accuracy.

From Figures 3.2 to 3.7, it is clear that the homogeneously imperfect interface parameter h does not significantly change the *locations* of the maximum normal and tangential tractions along the interface although it does indeed change their magnitudes.

It should be noted here that the imperfect interface model employed in the present paper allows for the possibility of a negative normal displacement jump across the interface. At first, this might seem to contradict the physical grounds on which the present problem is based (that the displacement jump cannot be negative). However, as explained in Hashin(1991b), since the imperfect *interface* model actually represents a compliant thin *interphase layer*, jumps in the normal displacement across the interface are defined by normal deformations of this *interphase layer* which can occur in both outward and inward directions. This implies that this interphase layer tolerates a limited negative normal displacement bounded by the original thickness of the interphase layer. Consequently, a negative normal displacement jump across the interface is acceptable provided it is smaller than the thickness of the original interphase layer (see Hashin, 1991 b). Our computations indicate (see Figures 3.2-3.7) that, in all cases discussed here, the negative normal displacement jump is indeed sufficiently small to be acceptable in this context.

Again, since Figures 3.2 to 3.7 show no significant difference in the results obtained between the cases $h_1=h_2$ and $h_1=3h_2$, the following discussions are based solely on the results from the case $h_1=h_2$.

We employ two different methods to analyze and understand the relationship between the imperfect interface parameter h and the failure of the interface. Firstly, we calculate the peak resultant traction (stress) along the interface (henceforth referred to as the peak traction).

The peak traction is found by calculating the maximum (or peak) value of the resultant traction $\sigma_{\text{resultant}}/S_{x0}$ along the interface for a given aspect ratio and a given value of the parameter h . Here, $\sigma_{\text{resultant}}$ is defined by the relation

$$\sigma_{\text{resultant}} = \sqrt{\sigma_{\text{normal}}^2 + \sigma_{\text{tangential}}^2} \quad (3.43)$$

and S_{x0} represents the remote loading (along the major axis of the ellipse). This peak traction is found always to occur at the point $\theta = 0$. Figure 3.8 plots the peak traction as a function of the imperfect interface parameter h for different aspect ratios.

From Figure 3.8, it is clear that, for each aspect ratio (except $a/b=1$ which is discussed below), the peak traction is a non-monotonic function of the interface parameter h . Consequently, for each aspect ratio, there is a unique value of the interface parameter h which corresponds to maximum peak traction. The collection of these values of h defines the parameter h^* (see Figure 3.10).

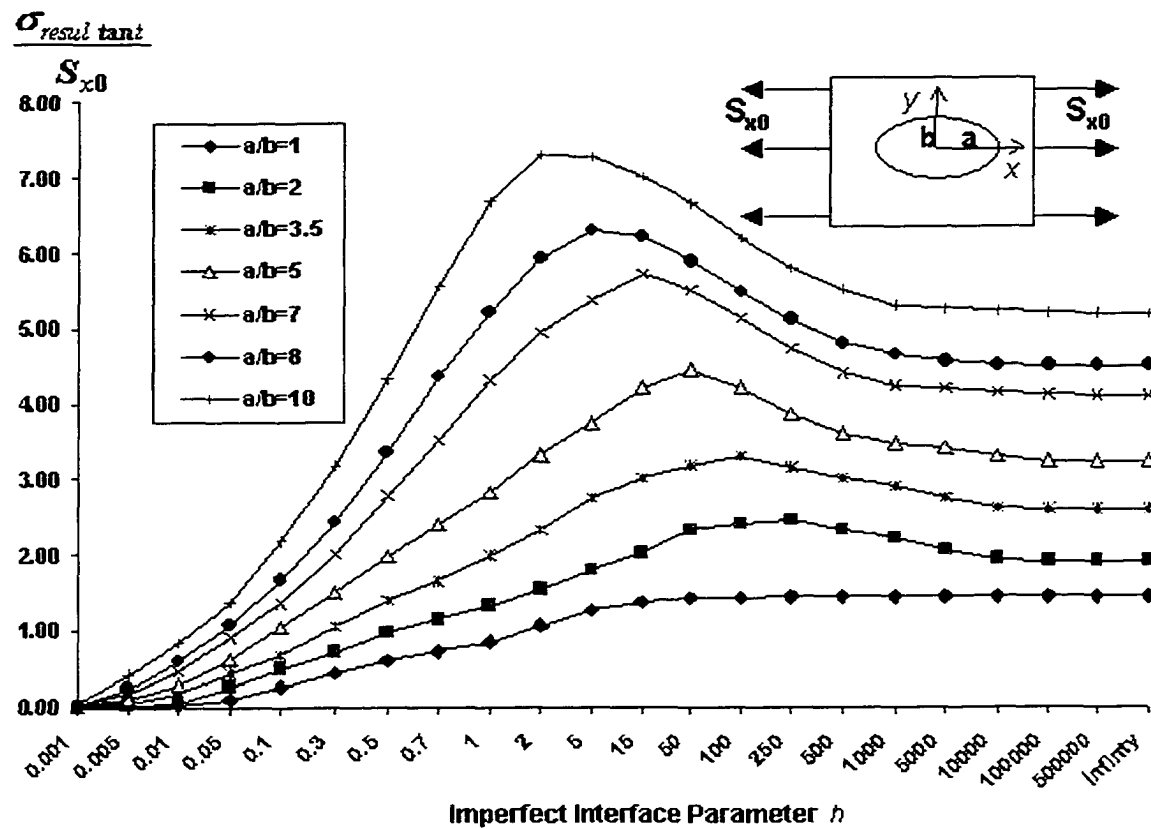


Figure 3.8: Peak traction along the interface varies as a function of the interface parameter $h = h_1 = h_2$ when the remote stress is S_{x0} .

In contrast to the results established for the circular inclusion where the maximum peak traction appears at $h = \infty$ (see Ru, 1998b), the results established here indicate that the maximum peak traction for an elliptic inclusion depends on the imperfect interface parameter and the aspect ratio of the ellipse. To explain this, we note that for the present interphase layer model (Hashin, 1991b), in order to keep the thickness of the adhesive layer between the elliptic inclusion and the matrix uniform, unlike the innermost edge, the outer edge of the interphase layer cannot be elliptical. This is perhaps why, in the case

of a homogeneously imperfect interface, values of h^* correspond to different values of local maximum stress for different values of the aspect ratio a/b (for the circular inclusion with homogeneously imperfect interface the outer edge of the interphase layer is circular). This makes the stress distributions along the interface extremely complicated in the case of an elliptic inclusion.

Next we consider the strain energy density criterion used by Achenbach & Zhu (1990). For the simple interphase model considered here, the strain energy criterion is particularly appropriate since it includes the effects of both normal and shear tractions across the interphase. The energy per unit (length) interphase, U , is defined as:

$$U = \frac{\sigma_{\text{normal}}^2}{2h_1} + \frac{\sigma_{\text{tangential}}^2}{2h_2}$$

By introducing $\bar{\sigma}_{\text{normal}} = \sigma_{\text{normal}} / S_{x0}$ and $\bar{\sigma}_{\text{tangential}} = \sigma_{\text{tangential}} / S_{x0}$, we obtain, in dimensionless form:

$$\bar{U} = \frac{\bar{\sigma}_{\text{normal}}^2}{2h_1} + \frac{\bar{\sigma}_{\text{tangential}}^2}{2h_2} \quad (3.44)$$

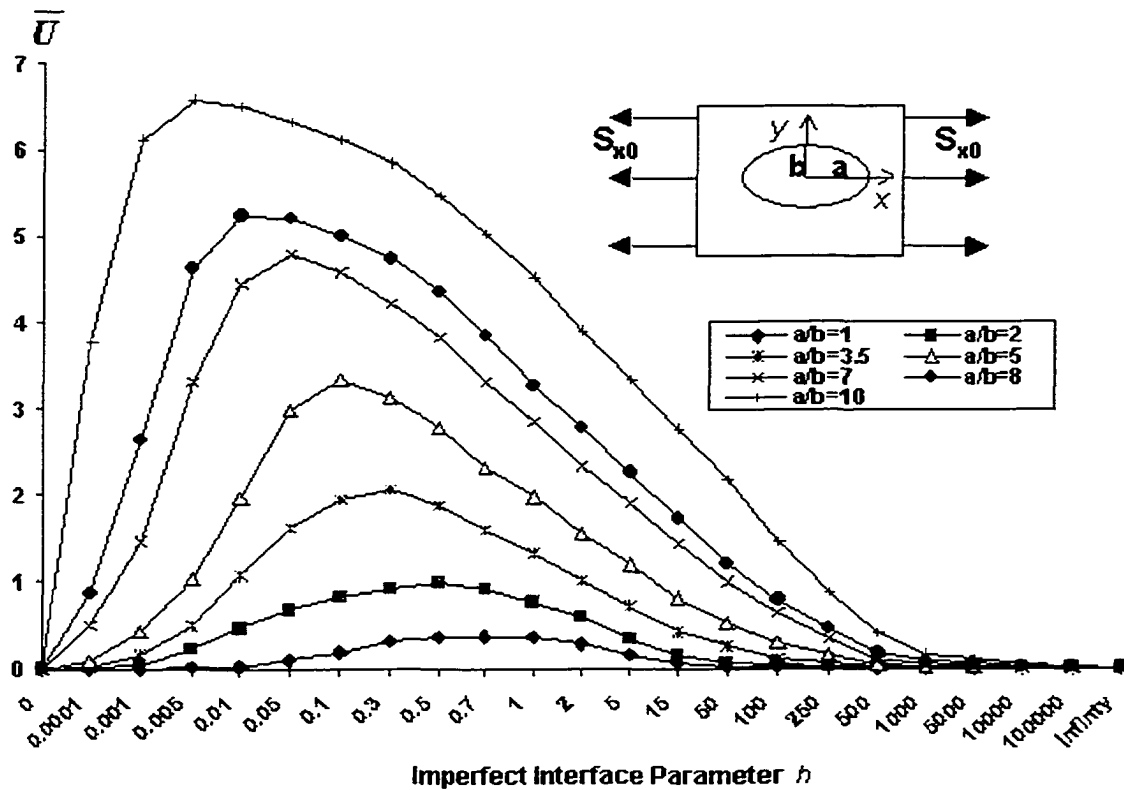


Figure 3.9: Peak energy per unit interphase varies as a function of the imperfect interface parameter $h = h_1 = h_2$ when the remote stress is S_{x0} .

It is now reasonable to assume that the interface will fail when \bar{U} reaches a critical value, \bar{U}_{cr} , which depends on the material properties. Figure 3.9 plots the peak (defined as in the case of peak traction above) strain energy per unit interphase \bar{U} as a function of the imperfect interface parameter $h(=h_1=h_2)$. It is clear from Figure 3.9 that \bar{U} is again a non-monotonic function of the interface parameter h . This means that we can again define a new parameter h^* defined by values of h which correspond to maximum values of the peak strain energy per unit interphase along the inclusion-matrix interface (see Figure 3.11).

We pause briefly to consider the case of the aspect ratio $a/b=1$ (circular inclusion). For $a/b=1$, from Figure 3.8, the peak traction is no longer a non-monotonic function of the interface parameter h with the value of h^* occurring at $h = \infty$ (as in Ru, 1998b). From Figure 3.9, however, \bar{U} is indeed a non-monotonic function of the interface parameter h with $h^* = 0.7$. In Figure 3.9, we may conclude that, since h^* appears only within a range corresponding to minimal stiffness of the spring layer, the energy density criterion is suitable for extremely soft interphase layers. According to Hashin (1991b), the imperfect interface condition arises from the assumption of a thin flexible coating of thickness $t \ll b$ with shear modulus $\mu_c \ll \min\{\mu_1, \mu_2\}$ between the inclusion and the matrix. The physical meaning of the parameter h and the energy density criterion are therefore consistent with Hashin's definition. However, for a slightly harder interface, the peak traction criterion (Figure 3.8) should be used to determine failure.

It should be mentioned here that Achenbach & Zhu (1990) define the strain energy density by the strain energy of the interphase layer per unit length along the interface. If the critical value of the strain energy density corresponding to interfacial failure is of interest, a physically more reasonable definition is \bar{U}_{cr} (as defined above) divided by the thickness of the interphase layer since this more appropriately represents the strain-energy density of the interphase material. In adopting this new definition, it is readily seen that the critical value \bar{U}_{cr} should be proportional to the thickness of the interphase layer and that it then approaches zero as the thickness of the interface layer vanishes (which corresponds to $h = \infty$, since h is inversely proportional to the thickness of the interphase layer).

Since values of h^* correspond to local maximum peak stresses and maximum values of \bar{U} and are related to the mechanical properties and thickness of the adhesive layer between the inclusion and the matrix, the parameter h^* may be used as a control parameter when designing composites involving elastic inclusions. For example, for the remote loading S_{x0} and aspect ratio $a/b=1$ (circular inclusion), the peak traction in Figure 3.8 corresponds to the value $h^* = \infty$ (perfect bonding). However, when $a/b=3.5$, the peak traction corresponds to $h^* = 100$. Since h^* is rendered dimensionless by division by μ_1/b , for a specific aspect ratio, we can avoid the maximum peak traction, or indeed minimize the maximum peak traction by adjusting mechanical properties (for example, the shear moduli of the matrix), and the thickness of the interphase layer (related to b).

The relationship between the parameter h^* and the aspect ratio a/b is presented in Figures 3.10 and 3.11 for the two different failure criteria.

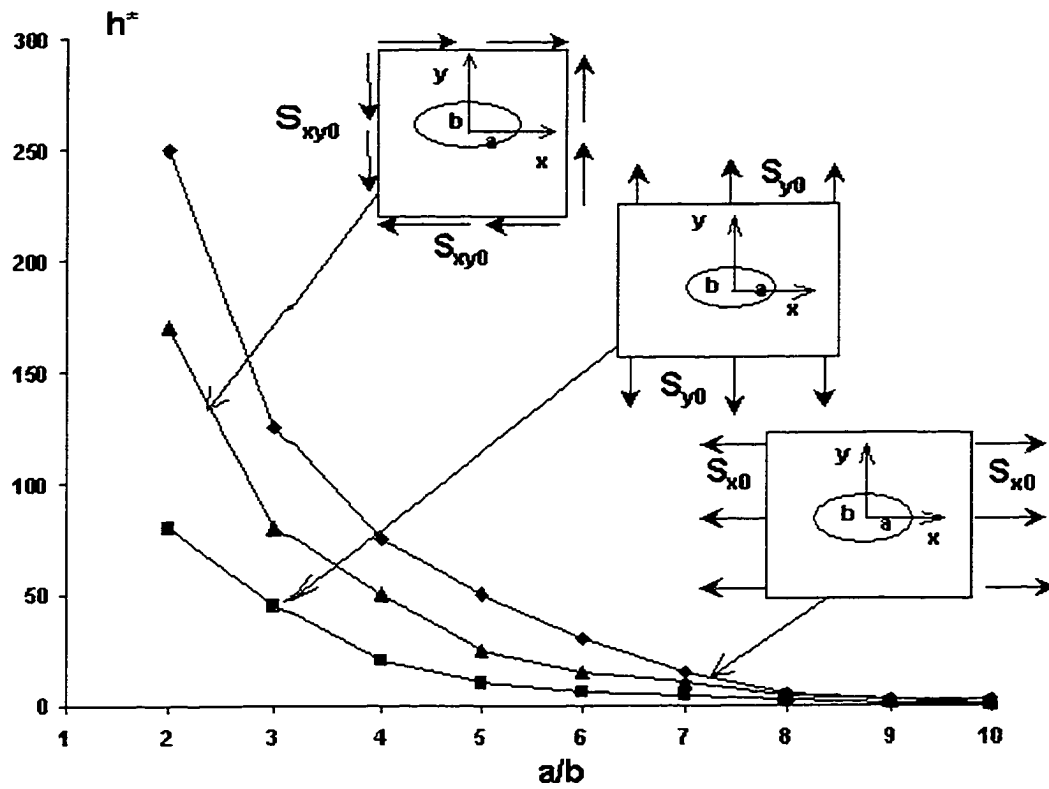


Figure 3.10: The relationship between h^* and a/b using the resultant traction criterion

when $h_1 = h_2 = h$.

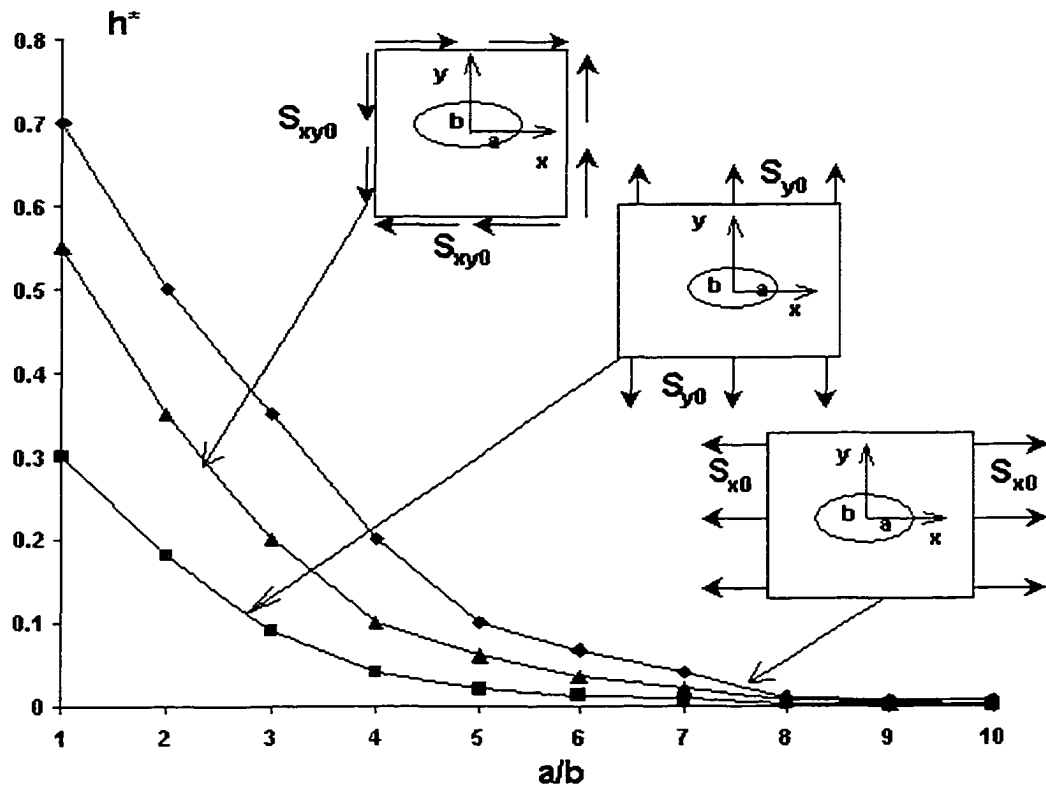


Figure 3.11: The relationship between h^* and a/b using the interfacial energy density criterion for $h_1 = h_2 = h$.

3.3.2 Average Stress Inside Inclusion

It is of interest also to investigate the effect of the imperfect interface parameter h on the average stress (defined in Eq. (2.25)) inside the elliptic inclusion under different remote loadings (Ru & Schiavone, 1997; Ru, 1998b). The relationship between average stress and the imperfect interface parameter $h(=h_1=h_2)$ is given in Figures 3.12 to 3.14 for three different remote loadings.

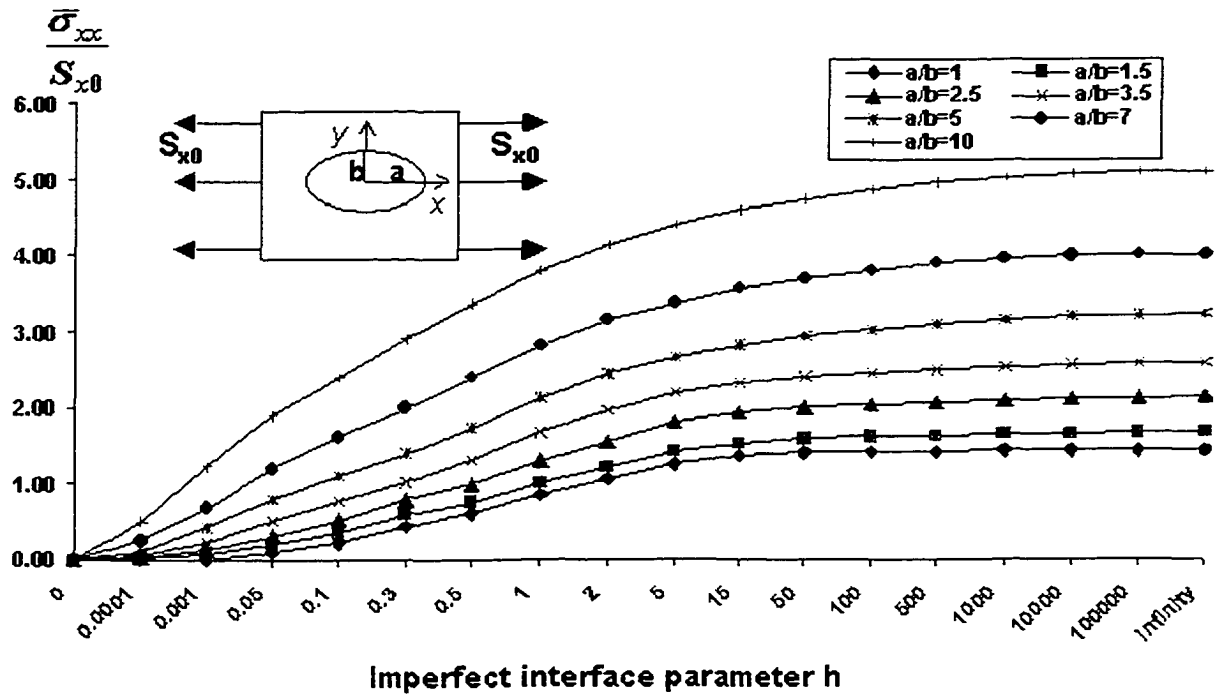


Figure 3.12: Effect of the imperfect interface parameter h on the average stress ($\frac{\bar{\sigma}_{xx}}{S_{x0}}$)

inside the inclusion for $h_1 = h_2 = h$ when the remote stress is S_{x0} .

We note that in Figure 3.12, the average stresses $\frac{\bar{\sigma}_{yy}}{S_{y0}}$ and $\frac{\bar{\sigma}_{xy}}{S_{x0}}$ induced inside the inclusion are significantly smaller than $\frac{\bar{\sigma}_{xx}}{S_{x0}}$ (with $\frac{\bar{\sigma}_{xy}}{S_{x0}}$ being close to zero), the difference being dependent on the parameter h and the aspect ratio of the ellipse.

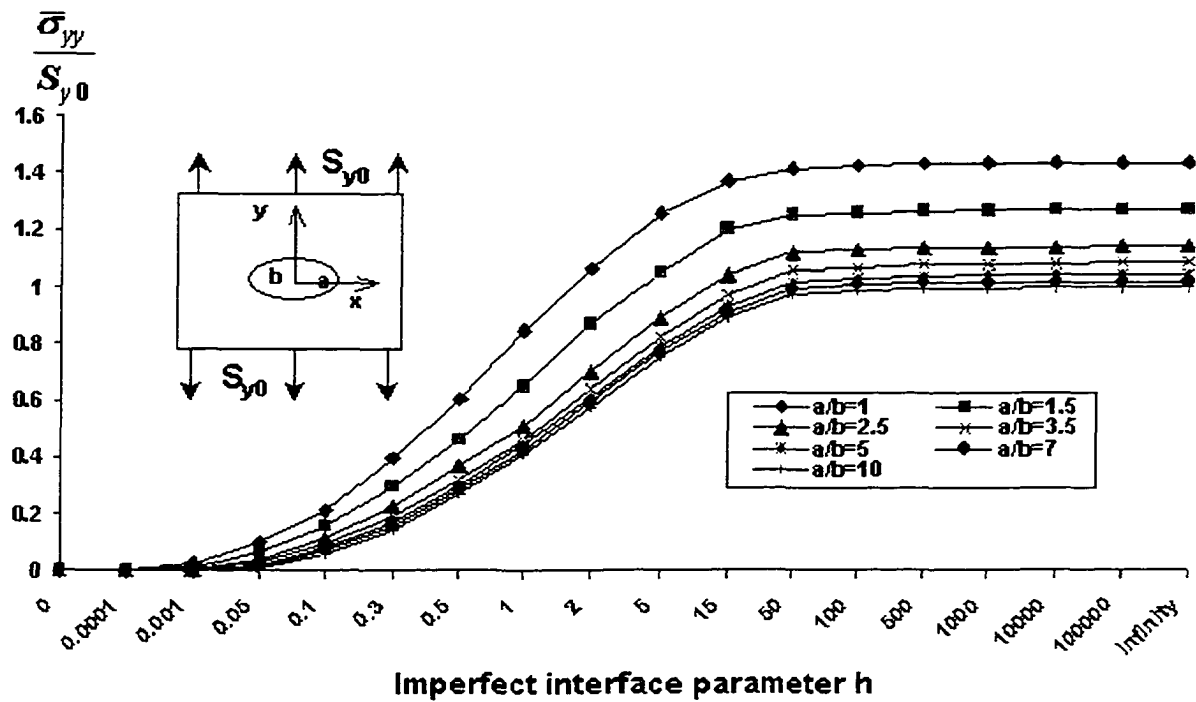


Figure 3.13: Effect of the imperfect interface parameter h on the average stress ($\frac{\bar{\sigma}_{yy}}{S_{y0}}$)

inside the inclusion for $h_1 = h_2 = h$ when the remote stress is S_{y0} .

We note that in Figure 3.13, the average stresses $\frac{\bar{\sigma}_{xx}}{S_{y0}}$ and $\frac{\bar{\sigma}_{xy}}{S_{y0}}$ induced inside the inclusion are significantly smaller than $\frac{\bar{\sigma}_{yy}}{S_{y0}}$ (with $\frac{\bar{\sigma}_{xy}}{S_{y0}}$ being close to zero), the difference being dependent on the parameter h and the aspect ratio of the ellipse.

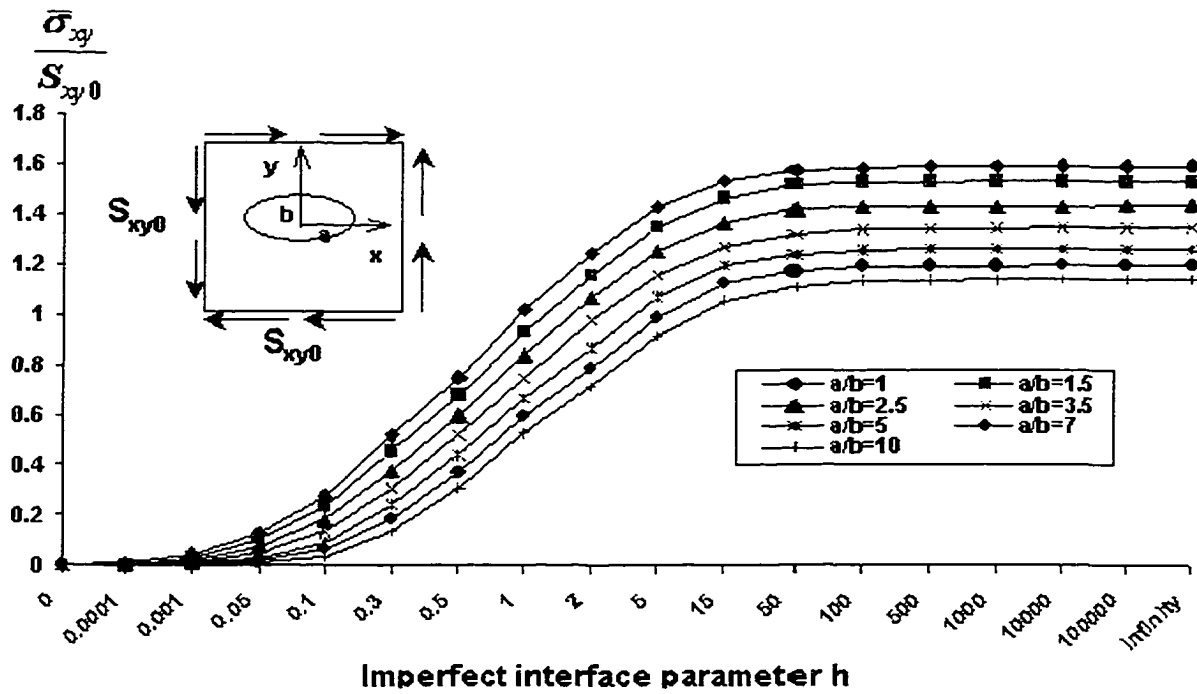


Figure 3.14: Effect of the imperfect interface parameter h on the average stress $\left(\frac{\bar{\sigma}_{xy}}{S_{xy0}}\right)$

inside the inclusion for $h_1 = h_2 = h$ when the remote stress is S_{xy0} .

We note that in Figure 3.14, the average stresses $\frac{\bar{\sigma}_{xx}}{S_{xy0}}$ and $\frac{\bar{\sigma}_{yy}}{S_{xy0}}$ induced inside the inclusion are extremely smaller than $\frac{\bar{\sigma}_{xy}}{S_{xy0}}$.

From Figure 3.12, it is clear that the effect of the imperfect interface parameter h on the average stress inside the inclusion increases with the aspect ratio of the ellipse when the remote loading is S_{x0} (along the major axis of the ellipse). However, for the other two remote loadings S_{y0} (along the minor axis of the ellipse) and S_{xy0} (pure shear), Figures 3.13 and 3.14 indicate that the effect of the imperfect interface parameter h on the average stress inside the inclusion decreases with the aspect ratio of the ellipse. In particular, for the remote loading S_{y0} , the average stress inside the inclusion is hardly affected by aspect ratios $a/b > 10$. For all remote loadings, our results indicate that the average stresses inside the inclusion are monotonic functions of the imperfect interface parameter h .

The above results also indicate that the average stress alone is insufficient to describe the debonding and failure of the interface. It is the local stress (maximum) that decides where the debonding and failure will occur. For example, from the stress distribution along the interface in Figure 3.2, the maximum local stresses occur at $\theta = 0$. These stresses are much greater than those in the case of perfect bonding although the average stresses (see Figures 3.12 to 3.14) are smaller.

Again it should be noted here that the imperfect interface model employed in the present paper allows for the possibility of a negative normal displacement jump across the interface. This, however, is explained as in Section 3.3.1 of Chapter 3(p59).

3.3.3 Internal Stress Distribution

In this section, using complex variable techniques we obtain infinite series representations of the internal stresses which, when evaluated numerically, demonstrate how the internal stresses vary with the aspect ratio of the inclusion and the parameter h describing the imperfection in the interface. These results can be used to evaluate the effects of the imperfect interface and the aspect ratio of the inclusion on internal failure caused by void formation and plastic yielding within the inclusion.

From Figures 3.15 – 3.17, it is clear that the non-uniformity of the stresses inside the inclusion is very strong and that the homogeneously imperfect interface parameter h ($\neq \infty$) significantly changes the stress distribution inside the inclusion. The local stresses reach peak value at $\theta = 0$. Henceforth, we denote by h^* the particular value of the imperfect interface parameter h corresponding to maximum peak stress. For example, for $a/b=3.5$, from Figure 3.15, the maximum peak stress corresponds to the value $h = h^* = 100$.

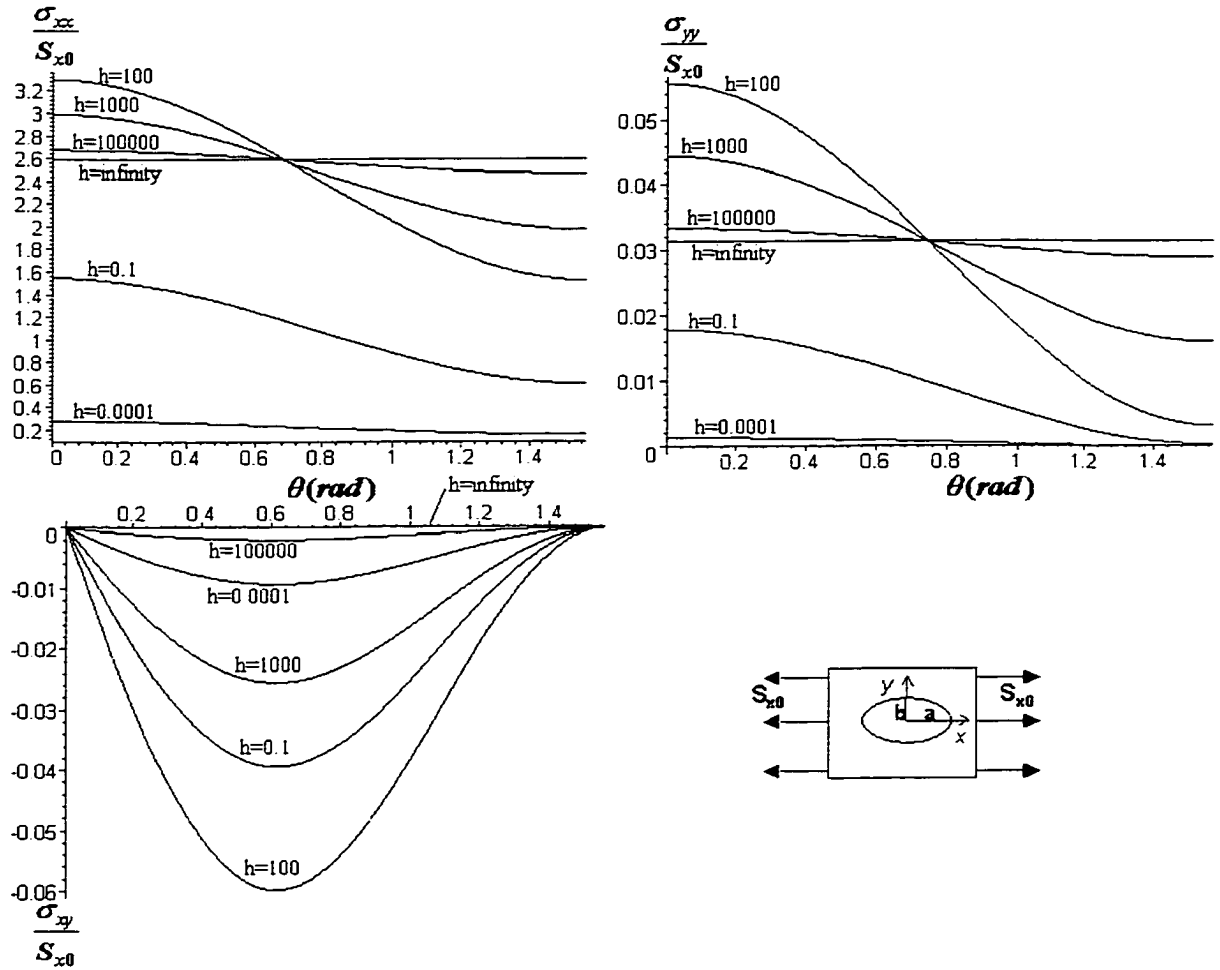


Figure 3.15: Non-uniformity of internal stresses along the interface when the remote stress is S_{x0} with $a/b=3.5$ for $h_1=h_2=h$

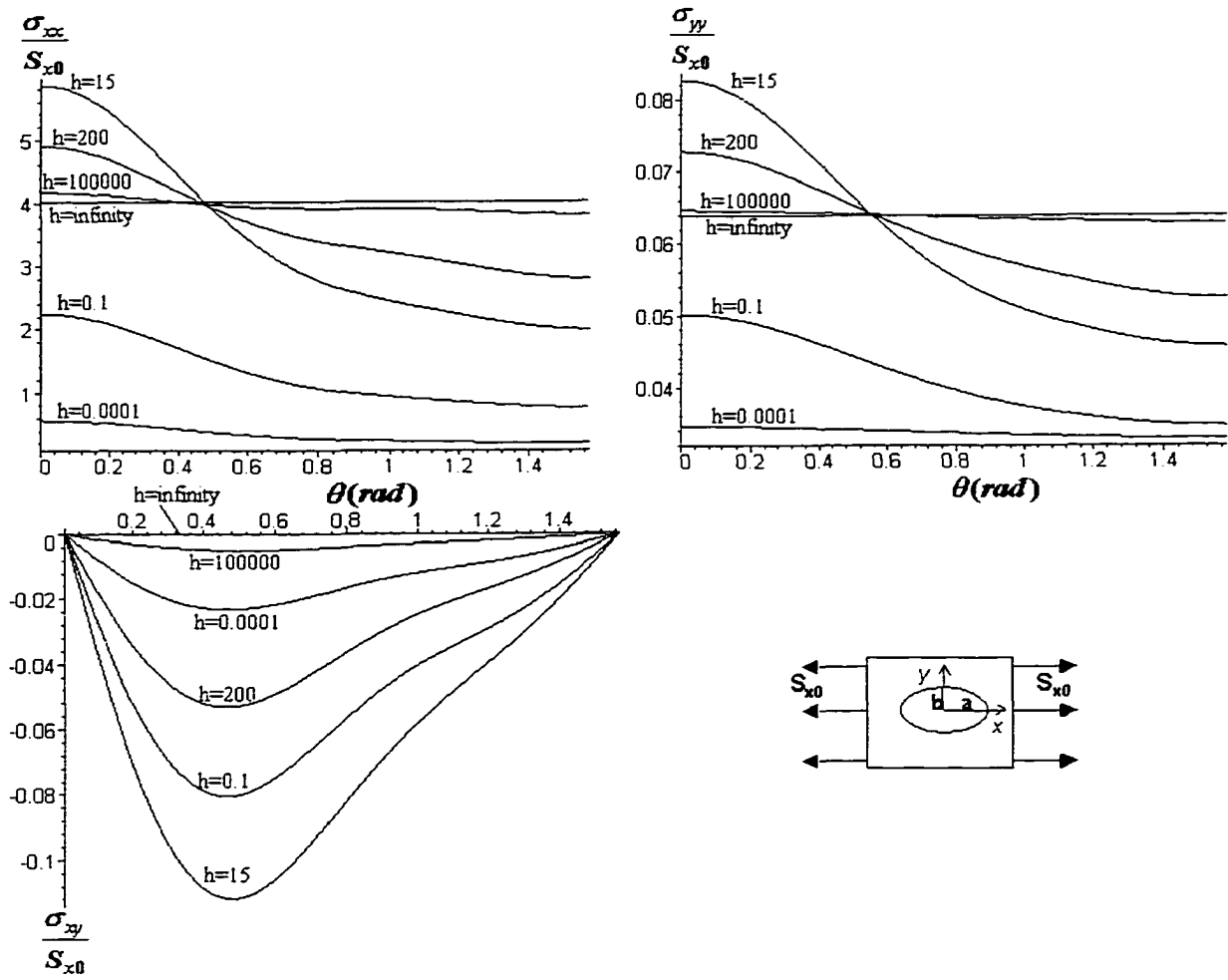


Figure 3.16: Non-uniformity of internal stresses along the interface when the remote stress is S_{x0} with $a/b=7$ for $h_1=h_2=h$

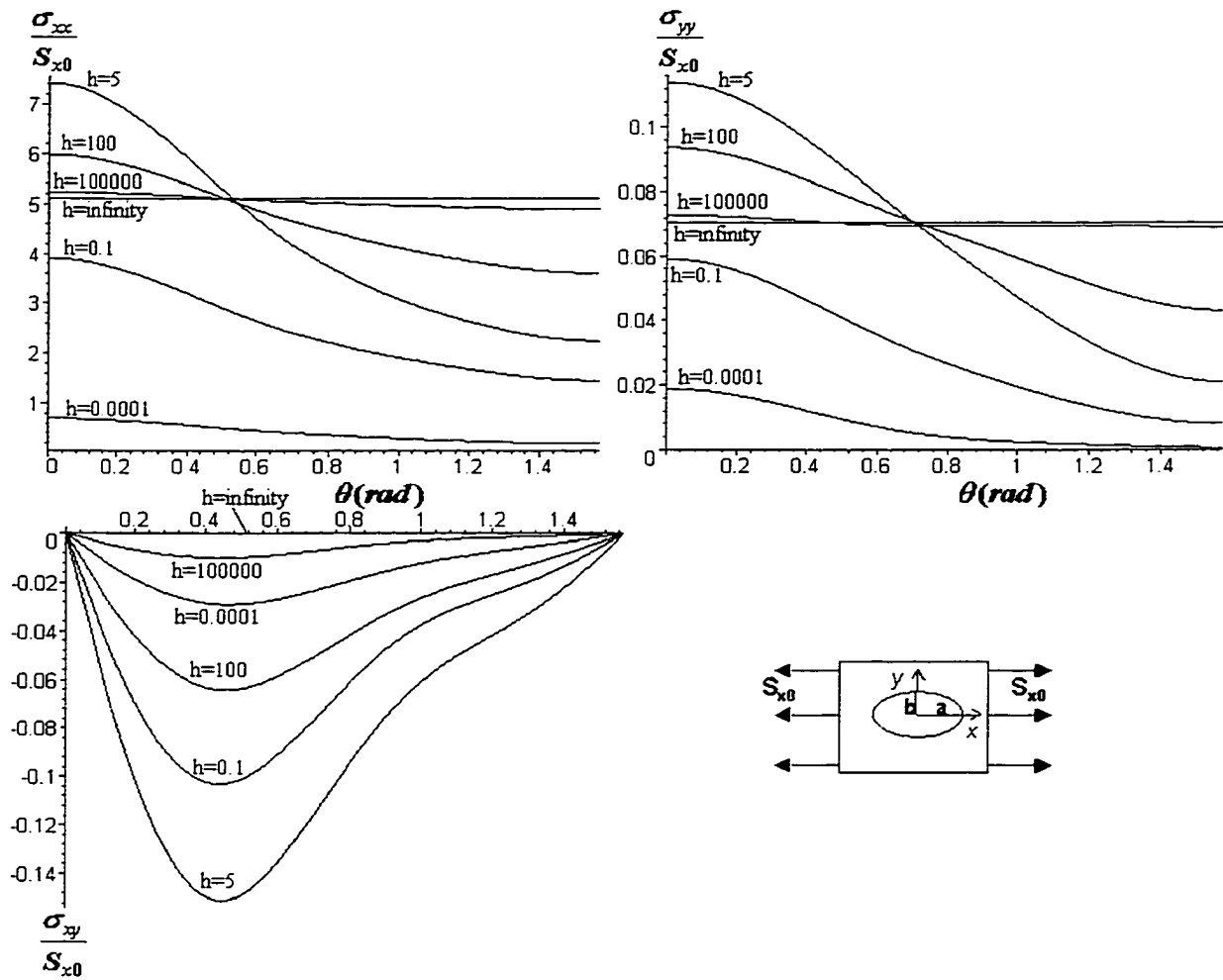


Figure 3.17: Non-uniformity of internal stresses along the interface when the remote stress is S_{x0} with $a/b=10$ for $h_1=h_2=h$

3.3.4 Mean Stresses and Von Mises Stresses

It is well known that the mean stress attains its maximum value on the boundary of the domain (Wheeler, 1996). However, there is no similar conclusion for von Mises stress (Wheeler, 1996). Despite this, the present calculation for the elliptic inclusion shows that the maximum value of the von Mises stress does indeed occur at the boundary. Figure 3.18 plots the stress distribution along the x and y axes for an elliptic inclusion with aspect ratio $a/b=3.5$ when the remote stress is S_{x0} . It is indicated that the maximum stresses in the case of σ_{xx} occur along the interface.

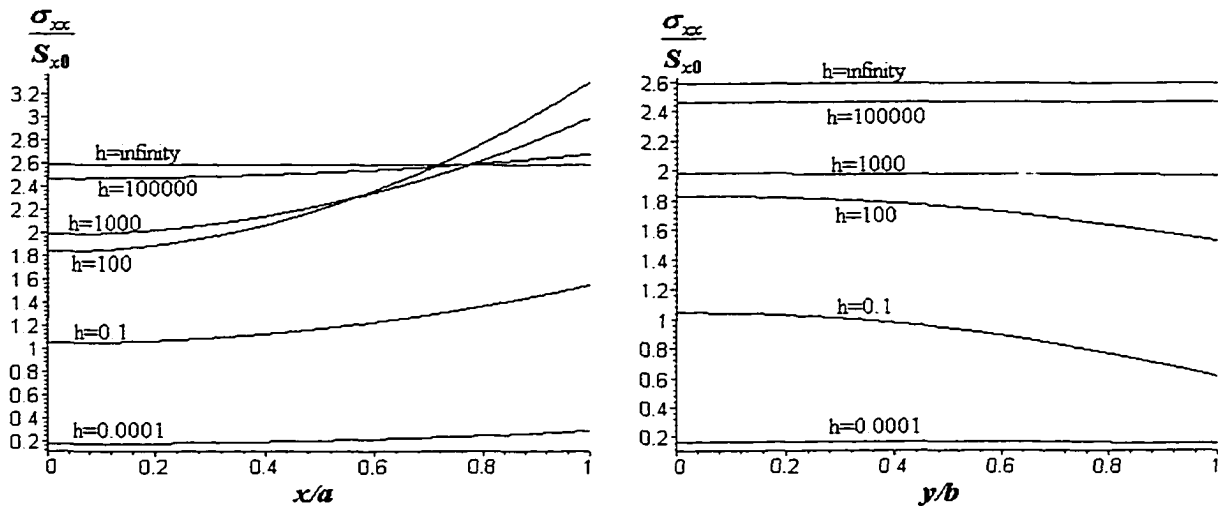


Figure 3.18: The stress distribution along the x and y axes for remote stress S_{x0} with $a/b=3.5$

Again, since there is no significant difference in the results obtained between the cases $h_1 = h_2 = h$ and $h_1 = 3h_2 = h$, the following discussions are based solely on the results from the case $h_1 = h_2 = h$.

We once again employ two different criteria to analyze and understand the relationship between the imperfect interface parameter h and the failure of the interface.

Firstly, we calculate the mean stress along the interface. We use the following definition of mean stress:

$$\sigma_{mean} = \sigma_{xx} + \sigma_{yy} \quad (3.45)$$

Figures 3.19, 3.20 and 3.21 plot the stress distributions for the mean stress for different values of a/b .

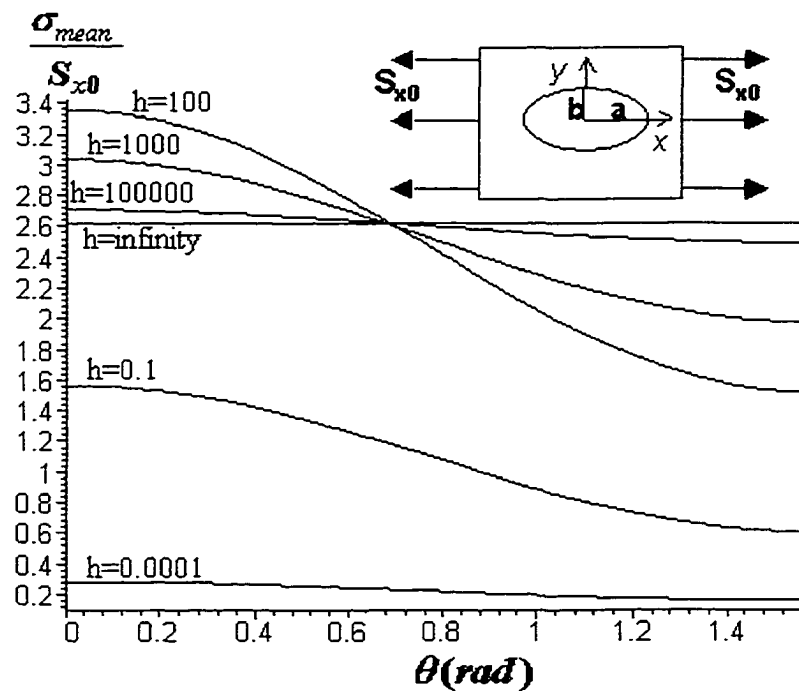


Figure 3.19: Non-uniformity of mean stress along the interface when the remote stress is

$$S_{x0} \text{ with } a/b=3.5 \text{ for } h_1=h_2=h$$

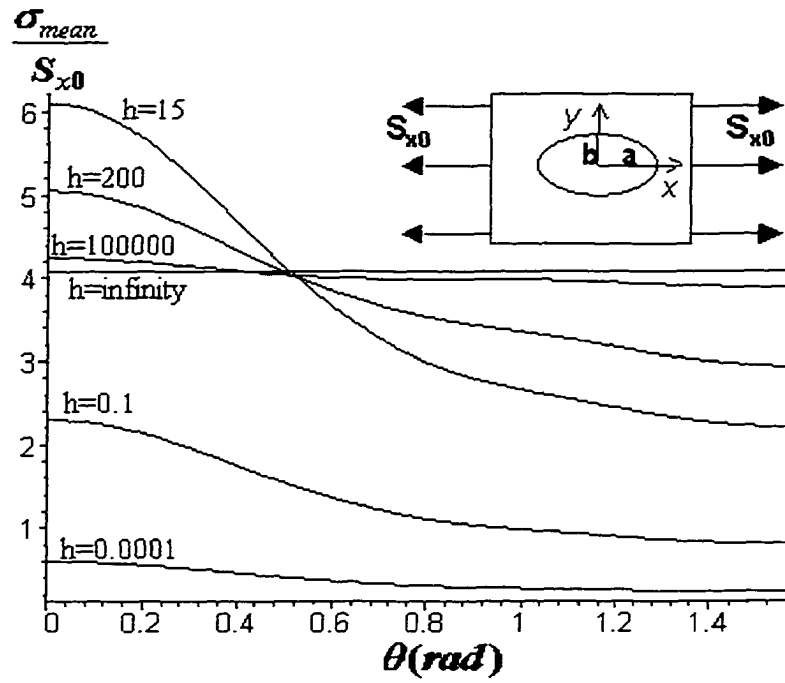


Figure 3.20: Non-uniformity of mean stress along the interface when the remote stress is S_{x0} with $a/b=7$ for $h_1=h_2=h$

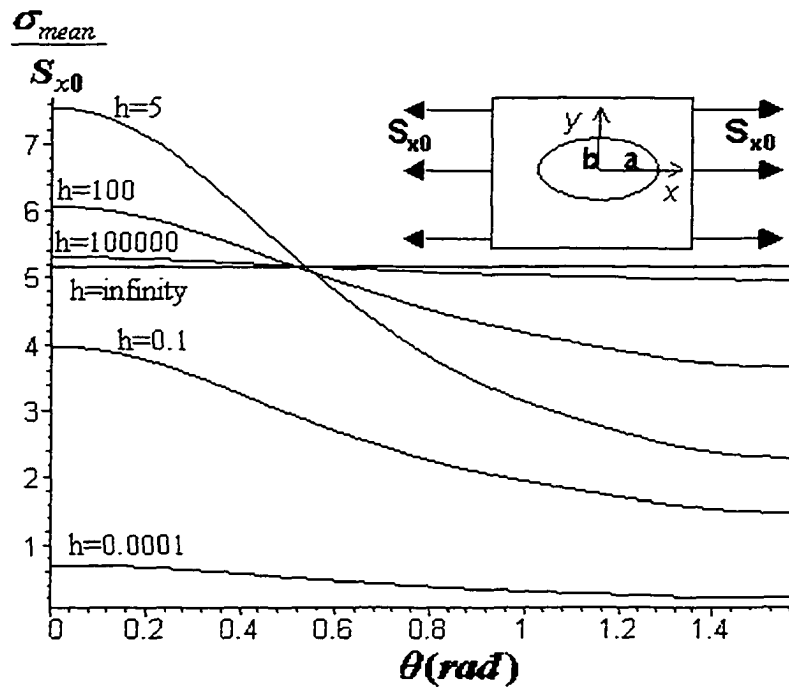


Figure 3.21: Non-uniformity of mean stress along the interface when the remote stress is S_{x0} with $a/b=10$ for $h_1=h_2=h$

From Figures 3.19, 3.20 and 3.21, it is clear that the mean stress inside the inclusion is non-uniform for different values of the imperfect interface parameter h ($\neq \infty$). The local mean stresses again reach peak values at $\theta = 0$. The specific values of h^* (corresponding to maximum peak stress) are the same as those obtained in Figures 3.15, 3.16 and 3.17 in

which we note that the values of $\frac{\sigma_{yy}}{S_{x0}}$ and $\frac{\sigma_{xy}}{S_{x0}}$ are much smaller than the corresponding

values $\frac{\sigma_{xx}}{S_{x0}}$ when the remote stress is S_{x0} . Consequently, the mean stresses are mainly

determined by $\frac{\sigma_{xx}}{S_{x0}}$.

Next, we calculate the von Mises equivalent stress. The von Mises equivalent stress is defined as (see Dowling, Norman E., 1993):

$$\sigma_{Von_Mises} = \sqrt{\frac{1}{6} [(\sigma_{xx} - \sigma_{yy})^2 + (\sigma_{yy} - \sigma_{zz})^2 + (\sigma_{zz} - \sigma_{xx})^2] + \sigma_{xy}^2 + \sigma_{yz}^2 + \sigma_{zx}^2} \quad (3.46)$$

For plane strain,

$$\sigma_{zz} = \nu(\sigma_{xx} + \sigma_{yy}); \sigma_{yz} = \sigma_{zx} = 0$$

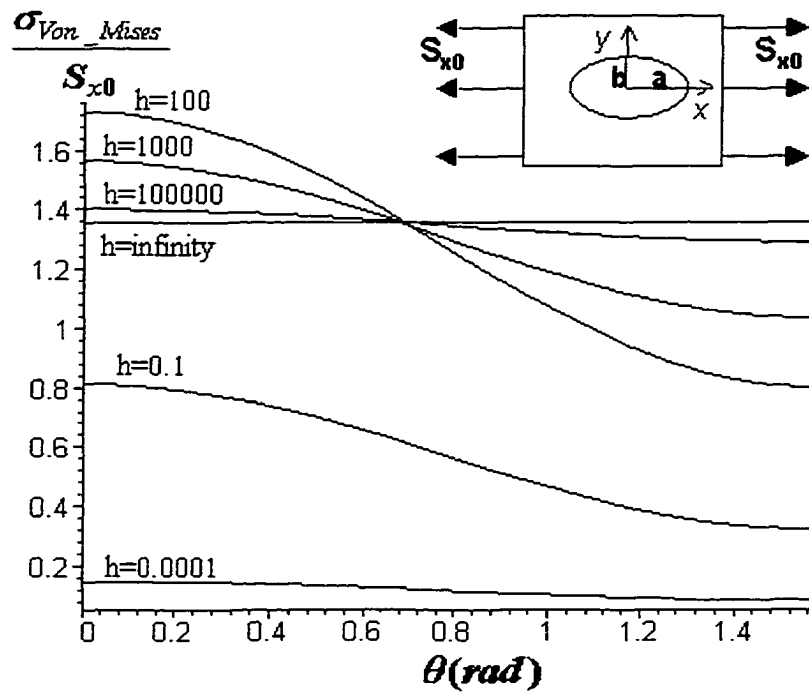


Figure 3.22: Non-uniformity of the von Mises stress along the interface when the remote stress is S_{x0} with $a/b=3.5$ for $h_1=h_2=h$

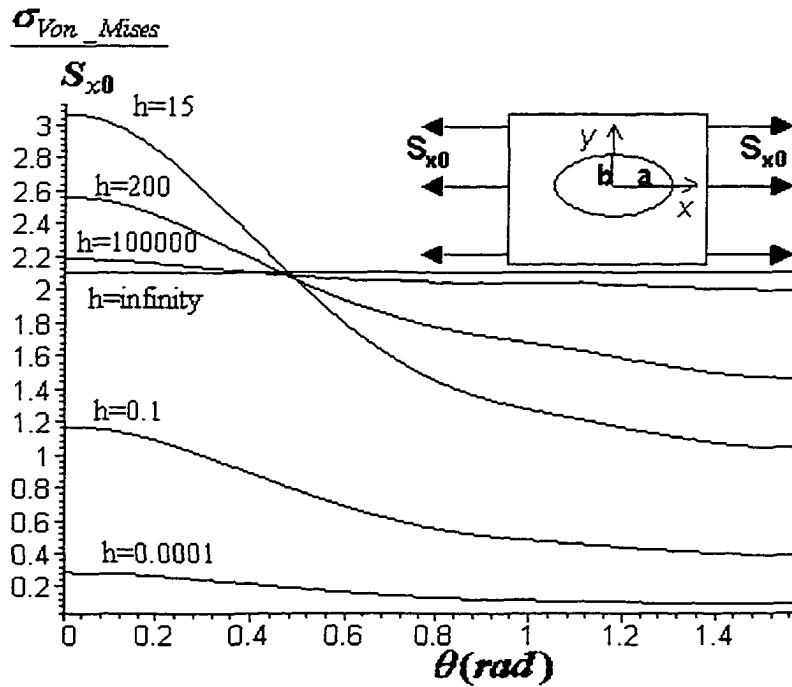


Figure 3.23: Non-uniformity of the von Mises stress along the interface when the remote stress is S_{x0} with $a/b=7$ for $h_1=h_2=h$

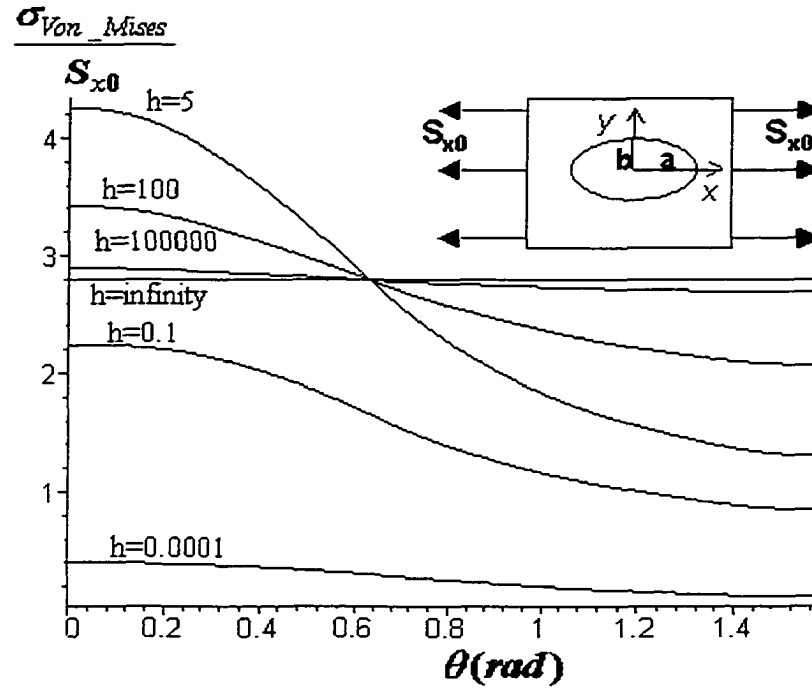


Figure 3.24: Non-uniformity of the von Mises stress along the interface when the remote stress is S_{x0} with $a/b=10$ for $h_1=h_2=h$

Figures 3.22, 3.23 and 3.24 plot the von Mises equivalent stress distributions along the interface for different values of the aspect ratio a/b . From Figures 3.22, 3.23 and 3.24, it is clear that the von Mises equivalent stresses inside the inclusion are non-uniform for different values of the imperfect interface parameter h ($\neq \infty$). The local von Mises equivalent stresses again attain peak values at $\theta = 0$. The specific values of h^* (corresponding to the maximum peak von Mises stress) are again the same as those in Figures 3.15, 3.16 and 3.17 in which we note that the values of $\frac{\sigma_{.xy}}{S_{x0}}$ and $\frac{\sigma_{.xy}}{S_{x0}}$ are much

smaller than the corresponding values $\frac{\sigma_{xx}}{S_{x0}}$ when the remote stress is S_{x0} . Consequently,

the von Mises stresses are mainly determined by $\frac{\sigma_{xx}}{S_{x0}}$.

All of the above results are based on the remote loading S_{x0} . We note that similar conclusions may be obtained for the remote loading S_{y0} . However, the case of the remote loading S_{xy0} , which characterizes pure shearing, merits individual attention. The corresponding results are presented in Figures 3.25 – 3.27.

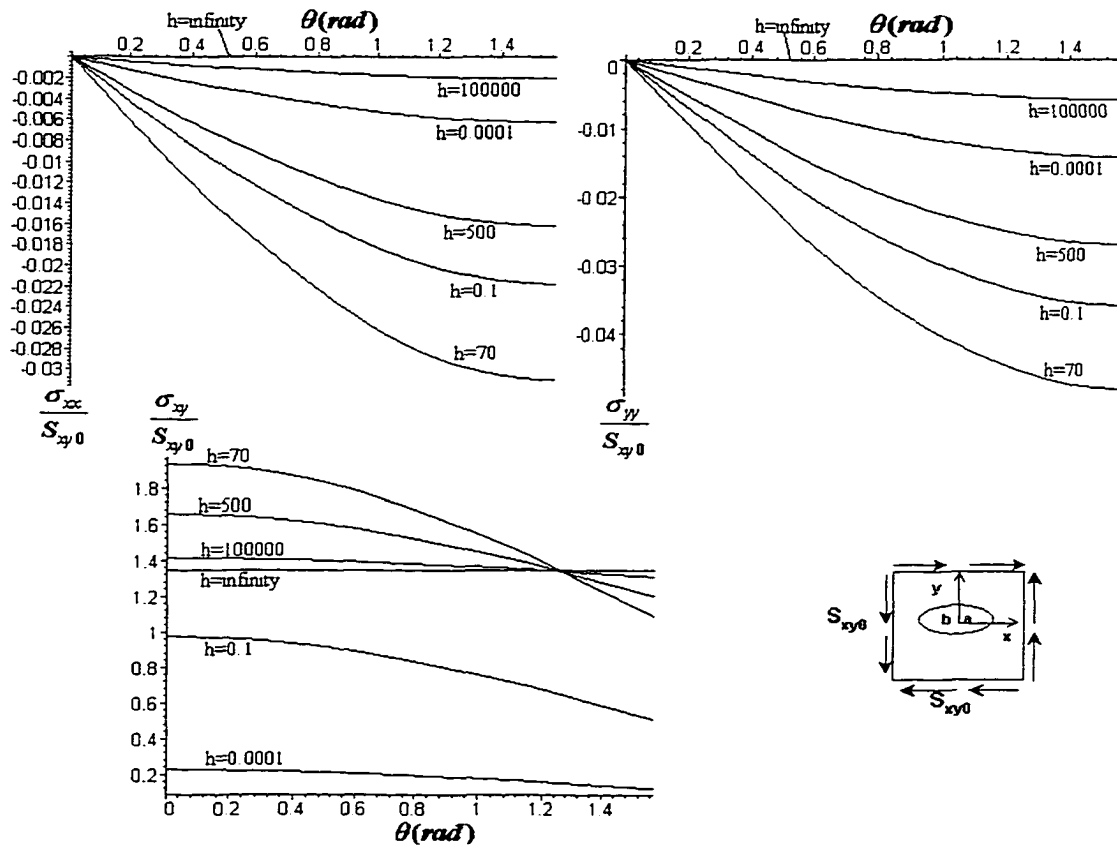


Figure 3.25: Non-uniformity of internal stresses along the interface when the remote stress is S_{xy0} with $a/b=3.5$ for $h_1=h_2=h$

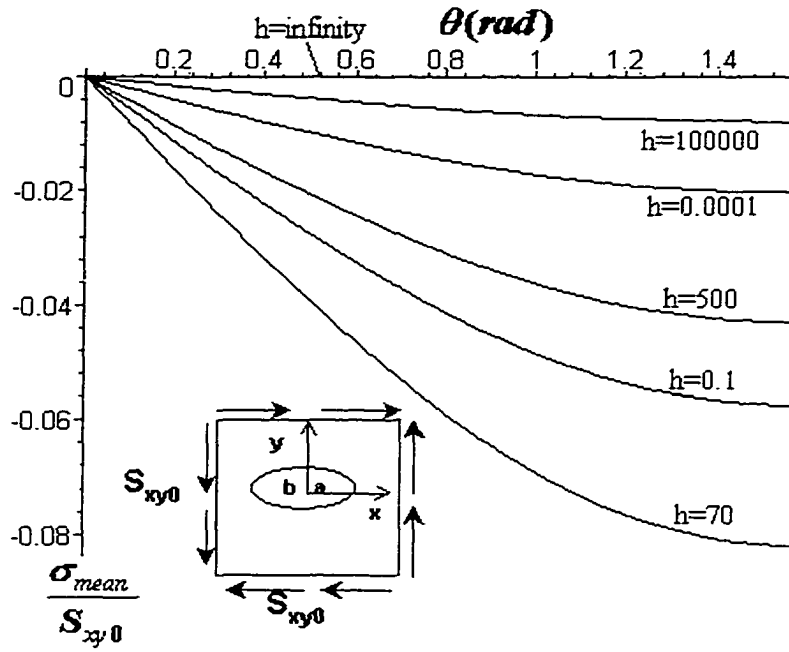


Figure 3.26: Non-uniformity of mean stress along the interface when the remote stress is

S_{xy0} with $a/b=3.5$ for $h_1=h_2=h$

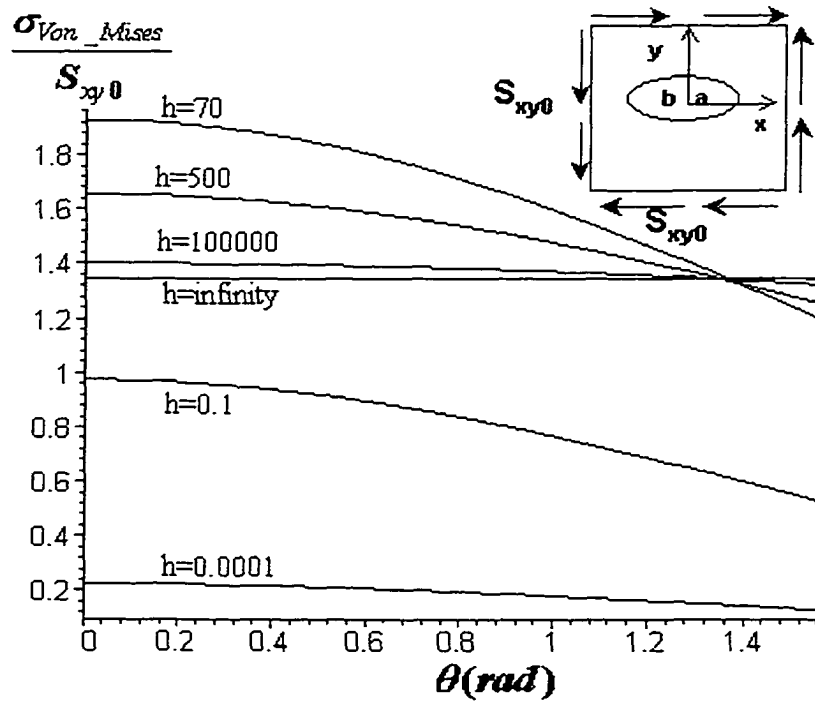


Figure 3.27: Non-uniformity of the von Mises stress along the interface when the remote

stress is S_{xy0} with $a/b=3.5$ for $h_1=h_2=h$

In Figure 3.25, the internal stress distribution at the interface is plotted for the value $a/b=3.5$ and different values of the parameter $h_1 = h_2 = h$ when the remote loading is S_{xy0} . Figures 3.26 and 3.27 plot the corresponding mean stress and von Mises equivalent stress distributions. It is clear that all stresses are largely controlled by $\frac{\sigma_{xy}}{S_{xy0}}$. When $h=70$, the local stress, mean stress and von Mises equivalent stress reach maximum peak values.

Since we obtain practically the same values of h^* for each of the different stress criteria (local stress, mean stress and von Mises equivalent stress), we need select only one of these to get the critical value h^* of the interface parameter. For example, Figure 3.28 plots the peak mean stress as a function of the imperfect interface parameter h . This peak mean stress is calculated at the value $\theta = 0$.

In Figures 3.15, 3.16 and 3.17, we note that the values of $\frac{\sigma_{xy}}{S_{x0}}$ are much smaller than

the corresponding values of $\frac{\sigma_{xx}}{S_{x0}}$ when the remote stress is S_{x0} . Thus, the mean is mainly

determined by $\frac{\sigma_{xx}}{S_{x0}}$.

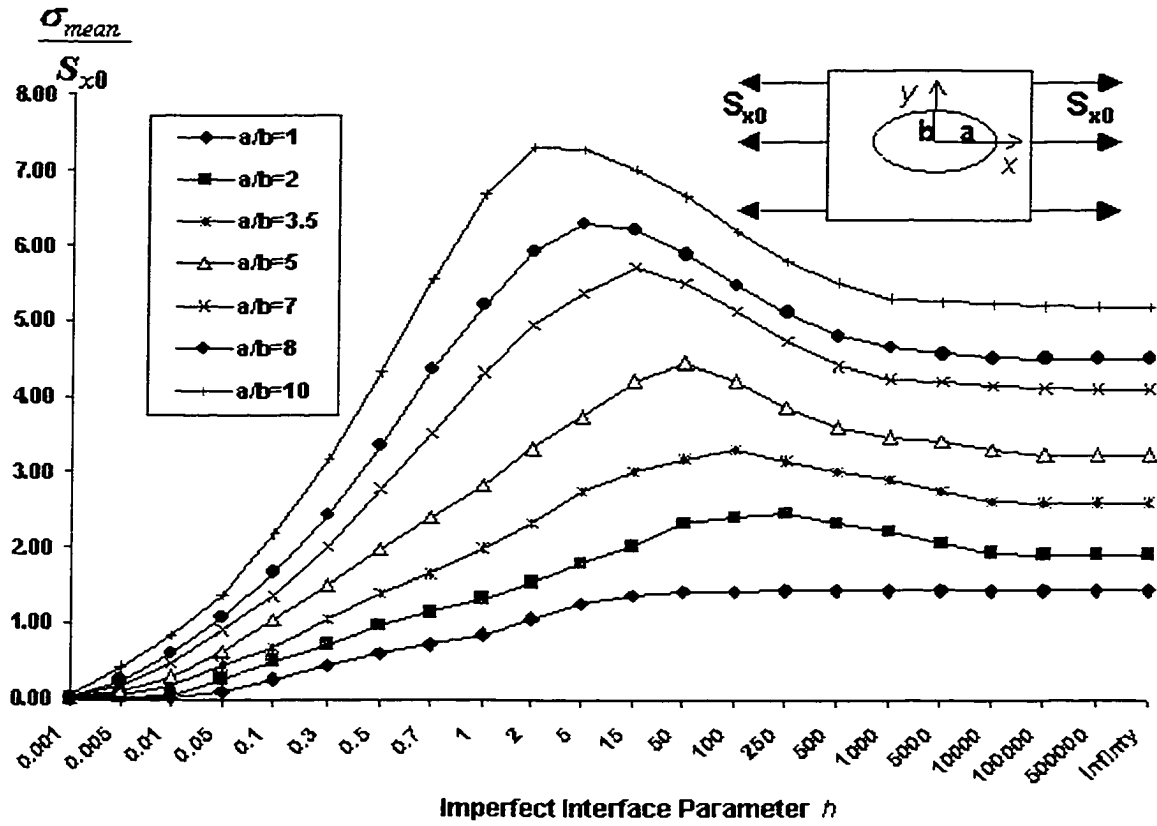


Figure 3.28: The peak mean stress along the interface varies as a function of the imperfect interface parameter h when the remote stress is S_{x0} for $h_1=h_2=h$

The maximum peak mean stress in Figure 3.28 corresponds to values of the parameter h^* . For the circular inclusion, we know that the maximum peak mean stress is realized at $h=\infty$ (see Ru, 1998b). However, for the elliptic inclusion, the maximum peak mean stress is related to the imperfect interface parameter and the aspect ratio of the inclusion. Again, since values of h^* correspond to local maximum peak stress and are related to the mechanical properties and thickness of the adhesive layer between the inclusion and the matrix, the parameter h^* may be used as a control parameter when designing composites involving elastic inclusions. For example, for the remote loading S_{x0} and aspect ratio $a/b=1$ (circular inclusion), the maximum peak stress in Figure 3.28 corresponds to the

value $h^* = \infty$ (perfect bonding). However, when $a/b = 3.5$, the maximum peak stress corresponds to $h^* = 100$. Since h^* is rendered dimensionless by division by μ_l/b , for a specific aspect ratio, we can avoid the maximum peak traction, or indeed minimize the maximum peak traction by adjusting mechanical properties and the thickness of the interphase layer. The relationship between the parameter h^* and the aspect ratio a/b is given in Figure 3.29.

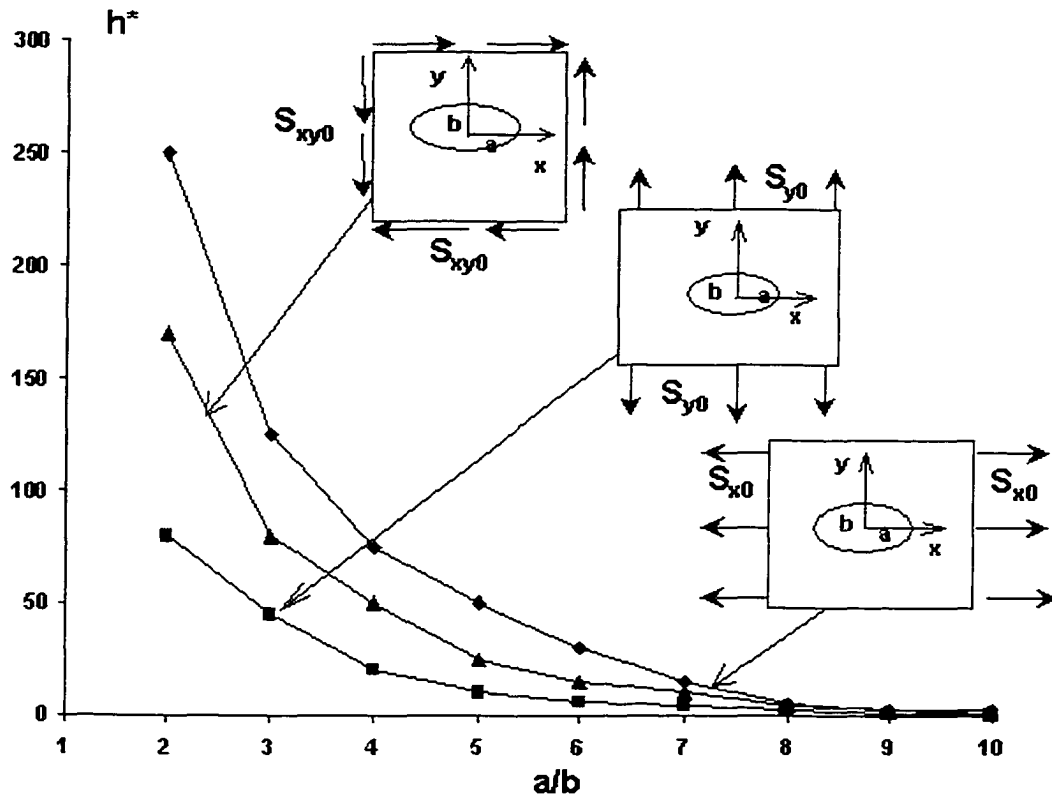


Figure 3.29: The relationship between h^* and a/b for $h_1 = h_2 = h$

3.4 SUMMARY OF RESULTS OBTAINED

This chapter presents a semi-analytic solution of the problem of an elliptic inclusion with homogeneously imperfect interface in plane elastostatics. Numerical computations and analysis of the subsequent results have led to the following conclusions:

1. The interface imperfection has a significant effect on stress fields inside the inclusion and near/along the interface. In addition, the corresponding stress distributions are closely related to the interface parameter describing the imperfection and the aspect ratio of the ellipse. It has also been indicated that the definition of the imperfect interface and the physical explanation of the interface parameters used in Hashin (1991b) are indeed suitable for describing the nature of the interface. Consequently, using only average stress is insufficient to describe the debonding and failure of the material interface since both are controlled by interfacial stresses which are themselves closely related to the imperfect interface parameter and the aspect ratio of the ellipse.
2. The effect of the imperfect interface parameter on the average stress inside the inclusion increases with the aspect ratio of the ellipse when the remote loading is along the major axis of the ellipse but decreases with the aspect ratio of the ellipse when the remote loading is either pure shear or along the minor axis of the ellipse. For all remote loadings, our numerical calculations indicate the average stresses inside the inclusion are monotonic functions of the imperfect interface parameter.
3. Our numerical results show that the peak interfacial traction and peak strain energy density are non-monotonic functions of the imperfect interface parameter h .

Consequently, for different aspect ratios, we have found a unique finite value h^* of the parameter $h(\neq 0, \infty)$ which corresponds to maximum peak traction or maximum peak strain energy density along the interface. Hence, since the parameter h characterizes the properties and thickness of the adhesive layer between the elliptic inclusion and the matrix, it is possible to predict and control the debonding and failure of the interface by identifying the value h^* for a given aspect ratio. In addition, this means that, for a specific aspect ratio, it is possible to minimize peak interfacial stress by adjusting the mechanical properties and thickness of the adhesive layer.

4. The strain energy density criterion used in this paper is suitable for very soft interphase layers. For slightly harder layers, we may use the relationship between peak interfacial traction and h^* to predict the failure of the interface.
5. The interface imperfection has a significant effect on the internal stresses. The internal stress distribution is closely related to the interface parameter h describing the imperfection and the aspect ratio of the ellipse.
6. Our numerical results show the peak mean stress and peak von Mises equivalent stress are both non-monotonic functions of the imperfect interface parameter. This allows us to find a finite value h^* of the parameter $h(\neq 0, \infty)$ which corresponds to the maximum peak mean stress or the maximum peak von Mises equivalent stress. Consequently, it is possible to predict and control the debonding and failure of the interface by identifying the h^* which depends on the aspect ratio of the ellipse and the properties and thickness of the adhesive layer between the inclusion and the matrix. This is a direct consequence of the fact that values of h^* correspond to maximum peak stress along the interface. Furthermore, we have shown that, for a specific aspect

ratio, it is possible to minimize peak stress by adjusting the mechanical properties and thickness of the adhesive layer.

7. For the cases discussed in this chapter, the mean stress and von Mises equivalent stress give practically the same value of h^* .

CHAPTER 4

THERMAL STRESS ANALYSIS OF AN ELLIPTIC INCLUSION WITH A COMPLIANT INTERPHASE LAYER IN PLANE ELASTICITY

4.1 INTRODUCTION

Mechanical failure resulting from residual stresses induced by thermal mismatch in composite materials and electromechanical devices has received considerable attention recently (see, for example, Wikstrom et al, 1999; Gouldstone et al, 1998; Ru, 1998a; Shen, 1998; Dao et al, 1997; Gleixner et al, 1997; Wu et al, 1996; Lee and Erdogan, 1995; Yeo et al, 1995; Williamson et al, 1993). Most of the existing studies have focused on multilayered material systems. However, many practical problems require a systematic study of the effects of interphase layers on thermal mismatch induced stresses in inclusion/matrix systems. For example, the failure of interconnect lines due to thermal stress-induced voiding has become a major issue in the design of reliable integrated circuits. In this case, the line is subjected to large tensile stresses upon cooling from high passivation deposition temperatures. For example, Niwa et al (1990) and Korhonen et al (1991) have modeled the passivated line as an elongated ellipsoid surrounded by an

infinite homogeneous matrix. One of the most effective procedures for the reduction of thermal stresses concerns the addition of an intermediate layer, with appropriate geometry and thermomechanical properties, between different material components where elevated thermal stresses occur. This procedure has been widely used in many practical problems where the thermal mismatch-induced stresses are of vital importance to mechanical integrity, such as thermal barrier coatings (see, for example, Lee and Erdogan, 1995), electromechanical devices (see, for example, Wu et al, 1996), and metal-ceramic composites (see, for example, Williamson et al, 1993). In doing so, the problem is reduced to one of the analysis of thermal stresses within an elliptic inclusion surrounded by an interphase layer. Unfortunately, in contrast to the well-known uniform stress state within a single elliptic inclusion perfectly bonded to the surrounding (infinite) matrix, as illustrated in this thesis, the stress field within an elliptic inclusion surrounded by an interphase layer is extremely complicated and intrinsically nonuniform (see also, for example, Shen et al, 1999a,b). Recently, for anti-plane shear deformations, Ru et al (1999) proved that the residual/thermal stress can be reduced to a fraction of its original value when a compliant interphase layer is inserted between the elliptic inclusion and its surrounding matrix. Of greater theoretical and practical interest, however, is the corresponding plane problem. Namely, the effect of a compliant interphase layer on the thermal stresses induced by the plane-strain deformations of an elliptic inclusion.

In many cases, the compliant layer between the inclusion and the surrounding material (matrix) may be considered to be a very thin interphase layer, or, in the context of this thesis, as an *imperfect interface*. To the author's knowledge, the solution of the problem associated with plane deformations of an elliptic inclusion with a

homogeneously imperfect interface (or compliant interphase layer) subjected to a uniform change in temperature has not been recorded in the literature.

In this chapter, we use the homogeneously imperfect interface model mentioned in Chapter 3 to study the effect of a compliant interphase layer on thermal stresses in an elliptic elastic inclusion embedded within an infinite matrix under a uniform change in temperature. Both elastic mismatch and thermal mismatch will be considered. Using complex variable techniques we obtain infinite series representations of the corresponding stresses which, when evaluated numerically, demonstrate how the peak thermal stress varies with the parameter h describing the imperfect interface (the interphase layer) (Shen et al, 1999c,e).

4.2 PROBLEM FORMULATION

As in Chapter 3, for plane deformations, the displacement components (u_x, u_y) , stress (or traction) components $(\sigma_{xx}, \sigma_{yy}, \sigma_{xy})$ and the components of the resultant force (F_x, F_y) in \mathcal{R}^2 referred to a Cartesian coordinate system are given in terms of two analytic functions $\phi(z)$ and $\psi(z)$ by (Muskhelishvili, 1963) :

$$2\mu(u_x + iu_y) = [\kappa\phi(z) - z\overline{\phi'(z)} - \overline{\psi(z)}] \quad , \quad (4.1)$$

$$\sigma_{xx} + \sigma_{yy} = 2[\phi'(z) + \overline{\phi'(z)}] \quad , \quad (4.2)$$

$$\sigma_{xx} - i\sigma_{xy} = \phi'(z) + \overline{\phi'(z)} - [z\overline{\phi''(z)} + \psi'(z)] \quad , \quad (4.3)$$

$$F_x + iF_y = -i[\phi(z) + z\overline{\phi'(z)} + \overline{\psi(z)}]_p^q \quad (4.4)$$

Here, $z=x+iy$ is the complex coordinate, ν is Poisson's ratio, $\kappa=3-4\nu$ for plane strain and, $\kappa=(3-\nu)/(1+\nu)$ for plane stress and $[]_p^q$ represents the change in the corresponding function in moving from point p to point q along any arc pq .

Across the interface Γ , the boundary displacements and tractions are written in normal-tangential ((n,t) -) coordinates as:

$$2\mu(u_n + iu_t) = [\kappa\phi(z) - z\overline{\phi'(z)} - \overline{\psi(z)}]e^{-i\rho(z)} \quad (4.5)$$

$$\sigma_{nn} - i\sigma_{nt} = \phi'(z) + \overline{\phi'(z)} - [z\overline{\phi''(z)} + \psi'(z)]e^{2i\rho(z)} \quad (4.6)$$

where n is the outward unit normal at $z \in \Gamma$ also represented, in complex form, by $e^{i\rho(z)}$ (where ρ defines the angle between the normal direction n and the positive x -axis). Assume that the elliptic inclusion is bonded to the matrix by a homogeneously imperfect interface. The interface conditions are then given by

$$[[\sigma_{nn} - i\sigma_{nt}]] = 0, \quad \sigma_{nn} = h_1(z)[[u_n]] - h_1(z)u_n^0, \quad \sigma_{nt} = h_2(z)[[u_t]] - h_2(z)u_t^0 \quad \text{on } \Gamma \quad (4.7)$$

Again, as in Chapter 3, here h_1 and h_2 are two non-negative interface parameters and $[[*]] = (*)_1 - (*)_2$ denotes the jump across Γ . u_n^0, u_t^0 are the displacements induced by the uniform (stress-free)eigenstrains $\{\epsilon_{xx}^0, \epsilon_{yy}^0, \epsilon_{xy}^0\}$.

If we consider only residual stresses resulting from eigen-strains, the stresses at infinity must be zero. Thus, the asymptotic conditions at infinity are given by

$$\phi_1(z) \equiv o(1), \quad \psi_1(z) \equiv o(1), \quad |z| \rightarrow \infty$$

From the second and third expressions in equation (4.7) we can now write

$$\sigma_{nn} - i\sigma_{nt} = \frac{h_1 - h_2}{2} [[u_n + iu_t]] + \frac{h_1 + h_2}{2} [[u_n - iu_t]] - [h_1 u_n^0 - ih_2 u_t^0] \quad , \quad (4.8)$$

where, from Equation (4.5), we have

$$2[[u_n + iu_t]] = \frac{e^{-i\rho(z)}}{\mu_1} [\kappa_1 \phi_1(z) - z\overline{\phi_1'(z)} - \overline{\psi_1(z)}] - \frac{e^{-i\rho(z)}}{\mu_2} [\kappa_2 \phi_2(z) - z\overline{\phi_2'(z)} - \overline{\psi_2(z)}], \quad \text{on } \Gamma \quad (4.9)$$

$$2[[u_n - iu_t]] = \frac{e^{i\rho(z)}}{\mu_1} [\kappa_1 \overline{\phi_1(z)} - \overline{z\phi_1'(z)} - \psi_1(z)] - \frac{e^{i\rho(z)}}{\mu_2} [\kappa_2 \overline{\phi_2(z)} - \overline{z\phi_2'(z)} - \psi_2(z)], \quad \text{on } \Gamma. \quad (4.10)$$

If the uniform eigen-strain in the inclusion is $\{\varepsilon_{xx}^0, \varepsilon_{yy}^0, \varepsilon_{xy}^0\}$, and we fix the corresponding displacement as follows

$$u_0 = x\varepsilon_{xx}^0 + y\varepsilon_{xy}^0, \quad v_0 = y\varepsilon_{yy}^0 + x\varepsilon_{xy}^0,$$

we may obtain

$$[u_n + iu_t]_0 = e^{-i\rho(z)} [\varepsilon_1 z + \varepsilon_2 \bar{z} + i\varepsilon_3 \bar{z}],$$

$$[u_n - iu_t]_0 = e^{i\rho(z)} [\varepsilon_1 \bar{z} + \varepsilon_2 z - i\varepsilon_3 z].$$

Here

$$\varepsilon_1 \equiv \frac{\varepsilon_{xx}^0 + \varepsilon_{yy}^0}{2}, \quad \varepsilon_2 \equiv \frac{\varepsilon_{xx}^0 - \varepsilon_{yy}^0}{2}, \quad \varepsilon_3 \equiv \varepsilon_{xy}^0. \quad (4.11)$$

Therefore we have

$$- [h_1 u_n^0 - i h_2 u_t^0] = -\frac{h_1 - h_2}{2} [\varepsilon_1 z + (\varepsilon_2 + i\varepsilon_3) \bar{z}] e^{-i\rho(z)} - \frac{h_1 + h_2}{2} [\varepsilon_1 \bar{z} + (\varepsilon_2 - i\varepsilon_3) z] e^{i\rho(z)}, \quad z \in \Gamma. \quad (4.12)$$

The geometry of the problem is simplified by mapping the ellipse into the unit circle using the same procedure as in Chapter 3. This time, however, the complex potentials $\phi_\alpha(\xi)$ and $\Omega_\alpha(\xi)$ are now expanded into their respective Laurent series in the matrix and in the inclusion as follows:

$$\phi_1(\xi) = \sum_{n=0}^{\infty} A_n \xi^{-(n+1)}, \quad \Omega_1(\xi) = \sum_{n=0}^{\infty} C_n \xi^{-(n+1)}, \quad (4.13)$$

$$\phi_2(\xi) = \sum_{n=0}^{\infty} (S_n \xi^{n+1} + T_n \xi^{-(n+1)}), \Omega_2(\xi) = \sum_{n=0}^{\infty} (D_n \xi^{n+1} + E_n \xi^{-(n+1)}). \quad (4.14)$$

Note that the constant terms have been omitted since they have no effect on the stress distribution. Furthermore, (3.17) combined with (4.13) and (4.14) yields the following relation (see Gong & Meguid, 1993):

$$T_n = \frac{S_n}{R^{2n+2}}, E_n = \frac{D_n}{R^{2n+2}} + (n+1) \frac{S_n}{R^{2n+4}} (R^4 - 1), \quad (n = 0, 1, 2, 3, \dots) \quad (4.15)$$

Consequently, (4.15) allows us to express the coefficients T_n , E_n in terms of the coefficients D_n , S_n . The traction continuity condition (see Eq. (3.20)) now becomes:

$$\sum_{n=0}^{\infty} A_n \xi^{-(n+1)} - \sum_{n=0}^{\infty} \bar{D}_n \bar{\xi}^{n+1} + \sum_{n=0}^{\infty} (\bar{C}_n - \bar{E}_n) \bar{\xi}^{-(n+1)} = \sum_{n=0}^{\infty} (S_n \xi^{n+1} + T_n \xi^{-(n+1)})$$

Noting that $\xi = e^{i\theta}$ on the interface, comparing coefficients, we obtain

$$\bar{C}_n = \bar{E}_n + S_n, C_n = E_n + \bar{S}_n \quad , \quad (n=0, 1, 2, 3, \dots), \quad (4.16)$$

$$A_n = T_n + \bar{D}_n, \bar{A}_n = \bar{T}_n + D_n \quad , \quad (n=0, 1, 2, 3, \dots), \quad (4.17)$$

Thus the coefficients A_n, C_n can be expressed in terms of the coefficients D_n, S_n . The only unknown coefficients are therefore D_n, S_n . These can be obtained from the interface condition (4.8) as follows.

By the same procedure of Eqs. (3.27)-(3.30) in Chapter 3, the interface condition (4.8) becomes

$$\begin{aligned}
[m'(\xi)]^2 [\overline{\phi'(\xi)} - e^{2i\theta} \Omega'(\xi)] = & \\
\frac{h_1 - h_2}{4} |m'(\xi)| \overline{m'(\xi)} m'(\xi) e^{-i\theta} & \left\{ \frac{1}{\mu_1} [\kappa_1 \phi_1(\xi) - \overline{\Omega_1(\xi)}] - \frac{1}{\mu_2} [\kappa_2 \phi_2(\xi) - \overline{\Omega_2(\xi)}] \right\} + \\
\frac{h_1 + h_2}{4} |m'(\xi)| [m'(\xi)]^2 e^{i\theta} & \left\{ \frac{1}{\mu_1} [\kappa_1 \overline{\phi_1(\xi)} - \Omega_1(\xi)] - \frac{1}{\mu_2} [\kappa_2 \overline{\phi_2(\xi)} - \Omega_2(\xi)] \right\} \\
- |m'(\xi)| \overline{m'(\xi)} & \left\{ \frac{h_1 - h_2}{2} \overline{m'(\xi)} e^{-i\theta} [\varepsilon_1 m + (\varepsilon_2 + i\varepsilon_3) \overline{m}] + \frac{h_1 + h_2}{2} m'(\xi) e^{i\theta} [\varepsilon_1 \overline{m} + (\varepsilon_2 - i\varepsilon_3) m] \right\}.
\end{aligned} \tag{4.18}$$

For thermal stresses resulting from a uniform change in temperature,

$$\varepsilon_{xx}^0 = \varepsilon_{yy}^0, \varepsilon_{xy}^0 = 0 \Rightarrow \varepsilon_1 = \varepsilon_{xx}^0 = \varepsilon_{yy}^0, \varepsilon_2 = \varepsilon_3 = 0$$

Using (3.11), we can eliminate ξ from the right-hand side of this expression and obtain:

$$[m'(\xi)]^2 [\overline{\phi'(\xi)} - e^{2i\theta} \Omega'(\xi)] =$$

$$\begin{aligned}
& m' \sqrt{1 + b^* \sin^2 \theta} \frac{b}{4} \left\{ (h_1 - h_2) \overline{m'} e^{-i\theta} \left[\frac{\kappa_1 \phi_1 - \overline{\Omega_1}}{\mu_1} - \frac{\kappa_2 \phi_2 - \overline{\Omega_2}}{\mu_2} - 2\varepsilon_1 m \right] \right. \\
& \left. + (h_1 + h_2) m' e^{i\theta} \left[\frac{\kappa_1 \overline{\phi_1} - \Omega_1}{\mu_1} - \frac{\kappa_2 \overline{\phi_2} - \Omega_2}{\mu_2} - 2\varepsilon_1 \overline{m} \right] \right\} \quad z \in \Gamma,
\end{aligned}$$

where $b^* = (a^2 - b^2)/b^2$. From (4.13)-(4.17), noting that $\xi = e^{i\theta}$ on the interface, we obtain the final form of the interface condition (4.8):

$$\begin{aligned}
& [m'(\xi)]^2 [\overline{\phi'(\xi)} - e^{2i\theta} \Omega'(\xi)] = \\
& m' \sqrt{1 + b^* \sin^2 \theta} \frac{Rbl}{8} \left\{ (h_1 - h_2) \mathcal{Q}_n + (h_1 + h_2) \overline{\mathcal{Q}_n} \right\} \quad z \in \Gamma, \quad (4.19)
\end{aligned}$$

where

$$\left. \begin{aligned}
& \mathcal{Q}_n = g_1 - g_2 e^{2i\theta} - g_3 e^{-2i\theta} + \sum_{n=0}^{\infty} M_n e^{-i(n+2)\theta} - \sum_{n=0}^{\infty} N_n e^{in\theta} \\
& - \sum_{n=0}^{\infty} M_n R^{-2} e^{-in\theta} + \sum_{n=0}^{\infty} N_n R^{-2} e^{i(n+2)\theta} \\
& g_1 = -\varepsilon_1 lR + \frac{\varepsilon_1 l}{R^3}, g_2 = -\frac{l\varepsilon_1}{R}, g_3 = \frac{l\varepsilon_1}{R}, M_n = (\Lambda_2 \overline{D}_n + \Lambda_3 T_n) \\
& N_n = (\Lambda_4 \overline{E}_n + \Lambda_5 S_n), \Lambda_1 = \frac{1}{\mu_1} (1 + \kappa_1), \Lambda_2 = \frac{\kappa_1}{\mu_1} + \frac{1}{\mu_2}, \\
& \Lambda_3 = \frac{\kappa_1}{\mu_1} - \frac{\kappa_2}{\mu_2}, \Lambda_4 = \frac{1}{\mu_1} - \frac{1}{\mu_2}, \Lambda_5 = \frac{1}{\mu_1} + \frac{\kappa_2}{\mu_2}.
\end{aligned} \right\} \quad (4.20)$$

Furthermore, in this case, we have

$$\varepsilon_1 = \frac{(\alpha_2 - \alpha_1)\Delta T}{2} = \frac{\Delta\alpha\Delta T}{2}, \quad (4.21)$$

where ΔT is the uniform change (cooling) in temperature, and α denotes the coefficient of thermal expansion.

From (3.11) and (4.13)-(4.17), the interface condition (4.19) becomes

$$\begin{aligned} & \left\{ d_0 + d_1 e^{-i\theta} + d_2 e^{i\theta} + d_3 e^{-2i\theta} + d_4 e^{2i\theta} + d_5 e^{-3i\theta} + d_6 e^{-4i\theta} + \sum_{n=0}^{\infty} U_n e^{i(n+2)\theta} + \sum_{n=0}^{\infty} V_n e^{-i(n+4)\theta} \right\} \\ & = \Lambda \sqrt{1 + b^* \sin^2 \theta} \times \\ & \left[+ \sum_{n=0}^{\infty} P_n e^{i(n+2)\theta} + \sum_{n=0}^{\infty} O_n e^{-i(n+4)\theta} + c_0 + c_1 e^{-i\theta} + c_2 e^{i\theta} + f_2 e^{i2\theta} + c_3 e^{-i2\theta} + c_4 e^{-i3\theta} + f_4 e^{-i4\theta} \right] \end{aligned} \quad (4.22)$$

where

$$\begin{aligned} U_n &= 2l^2 \left[-R^4 (\bar{T}_n + D_n)(n+1) + 2R^2 (\bar{T}_{n+2} + D_{n+2})(n+3) - (\bar{T}_{n+4} + D_{n+4})(n+5) \right] \\ V_n &= 2l^2 \left[-2R^2 (T_{n+1} + \bar{D}_{n+1})(n+2) + 2(T_{n+3} + \bar{D}_{n+3})(n+4) + \right. \\ & \left. R^4 (E_{n+4} + \bar{S}_{n+4})(n+5) - 2R^2 (E_{n+2} + \bar{S}_{n+2})(n+3) + \right. \\ & \left. (E_n + \bar{S}_n)(n+1) + 2R^2 (T_n + \bar{D}_n)(n+1) + (T_{n+2} + \bar{D}_{n+2})(n+3) \right] \end{aligned} \quad (4.23)$$

$$\left. \begin{aligned}
P_n &= L_{n+4} + G_{n+2} + J_n, O_n = F_{n+2} - H_{n+4} - K_n, \\
F_n &= 2(h_1 + h_2)R^{-2}\bar{N}_n + (h_1 - h_2)(1 + R^{-4})M_n, \\
G_n &= 2(h_1 + h_2)R^{-2}\bar{M}_n + (h_1 - h_2)(1 + R^{-4})N_n, \\
H_n &= (h_1 + h_2)\bar{N}_n + (h_1 - h_2)R^{-2}M_n, J_n = (h_1 + h_2)\bar{M}_n + (h_1 - h_2)R^{-2}N_n, \\
K_n &= \left[(h_1 + h_2)R^{-2}\bar{N}_n + (h_1 - h_2)M_n \right] R^{-2}, \\
L_n &= \left[(h_1 + h_2)R^{-2}\bar{M}_n + (h_1 - h_2)N_n \right] R^{-2}, \\
f_1 &= (h_1 + h_2)(\bar{g}_1 - \bar{g}_3 R^{-2}) + (h_1 - h_2)(g_1 + g_2 R^{-2}), \\
f_2 &= (h_1 + h_2)\bar{g}_3 - (h_1 - h_2)g_2, \\
f_3 &= (h_1 + h_2)(-\bar{g}_2 - \bar{g}_1 R^{-2}) + (h_1 - h_2)(g_3 - g_1 R^{-2}), \\
f_4 &= \left[(h_1 + h_2)\bar{g}_2 - (h_1 - h_2)g_3 \right] R^{-2}, \\
c_0 &= f_1 + L_2 + G_0 + H_0, c_1 = L_1 + H_1, c_2 = L_3 + G_1, \\
c_3 &= L_0 + F_0 + H_2 + f_3, c_4 = F_1 + H_3,
\end{aligned} \right\} \quad (4.24)$$

$$\left. \begin{aligned}
\Lambda &= \frac{b(a+b)^3}{2(a-b)}, \\
d_0 &= 4l^2 R^2 (\bar{T}_0 + D_0) - 6l^2 (\bar{T}_2 + D_2) + 2l^2 R^4 (E_0 + \bar{S}_0) \\
d_1 &= -4l^2 (\bar{T}_1 + D_1) + 4l^2 (T_0 + \bar{D}_0) + 4l^2 R^4 (E_1 + \bar{S}_1) \\
d_2 &= 8l^2 R^2 (\bar{T}_1 + D_1) - 8l^2 (\bar{T}_3 + D_3) \\
d_3 &= -2l^2 (\bar{T}_0 + D_0) + 4l^2 (T_0 + \bar{D}_0) + 8l^2 (T_1 + \bar{D}_1) + \\
& 6l^2 R^4 (E_2 + \bar{S}_2) - 4l^2 R^2 (E_0 + \bar{S}_0) \\
d_4 &= 0 \\
d_5 &= -4l^2 R^2 (T_0 + \bar{D}_0) + 8l^2 (T_1 + \bar{D}_1) + 8l^2 R^4 (E_3 + \bar{S}_3) \\
& - 8l^2 R^2 (E_1 + \bar{S}_1) + 12l^2 (T_2 + \bar{D}_2) \\
d_6 &= 0
\end{aligned} \right\} \quad (4.25)$$

In the above expressions, the coefficients T_i and E_i can be written in terms of S_i and D_i by using (4.15). Hence, the only remaining unknown coefficients are again S_i and D_i .

Next, we employ a method similar to that used in Chapter 2 by substituting the following expression (see Appendix) into (4.22):

$$\begin{aligned}
\sqrt{1+b^* \sin^2 \theta} &= \sum_{k=-\infty}^{\infty} I_{2k} e^{i2k\theta} \approx \sum_{k=0}^{M-1} I_{2k} (e^{i2k\theta} + e^{-i2k\theta}) + I_{2M} \frac{e^{i2M\theta} + e^{-i2M\theta} - \eta(e^{i2(M-1)\theta} + e^{i2(1-M)\theta})}{1 + \frac{1}{R^4} - \frac{e^{i2\theta} + e^{-i2\theta}}{R^2}} \\
&= \sum_{k=0}^{M-1} I_{2k} (e^{i2k\theta} + e^{-i2k\theta}) + I_{2M} \frac{e^{i2M\theta} + e^{-i2M\theta} - \eta(e^{i2(M-1)\theta} + e^{i2(1-M)\theta})}{1 + \eta^2 - \eta(e^{i2\theta} + e^{-i2\theta})} \\
&= \sum_{k=0}^{M-1} I_{2k} (e^{i2k\theta} + e^{-i2k\theta}) + I_{2M} \frac{e^{i2M\theta} + e^{-i2M\theta} - \eta(e^{i2(M-1)\theta} + e^{i2(1-M)\theta})}{x - \eta(e^{i2\theta} + e^{-i2\theta})}
\end{aligned}$$

We obtain

$$\begin{aligned}
&\left[x_2 e^{-i\theta} + x_4 e^{-2i\theta} + x_6 e^{-3i\theta} + x_8 e^{-4i\theta} - x_{10} e^{-5i\theta} - x_{11} e^{-6i\theta} + x \sum_{n=0}^{\infty} V_n e^{-i(n+4)\theta} - \eta \sum_{n=0}^{\infty} V_n e^{-i(n+2)\theta} - \eta \sum_{n=0}^{\infty} V_n e^{-i(n+6)\theta} \right] \\
&+ x_1 + \left[x_3 e^{i\theta} + x_5 e^{2i\theta} - x_7 e^{3i\theta} - x_9 e^{4i\theta} + x \sum_{n=0}^{\infty} U_n e^{i(n+2)\theta} - \eta \sum_{n=0}^{\infty} U_n e^{i(n+4)\theta} - \eta \sum_{n=0}^{\infty} U_n e^{in\theta} \right] = \\
&\Lambda \left\{ \left[\sum_{k=0}^{M-1} I_{2k} (e^{i2k\theta} + e^{-i2k\theta}) (x - \eta(e^{i2\theta} + e^{-i2\theta})) + I_{2M} (e^{i2M\theta} + e^{-i2M\theta} - \eta(e^{i2(M-1)\theta} + e^{i2(1-M)\theta})) \right] \right. \\
&\left. \left[\sum_{n=0}^{\infty} P_n e^{i(n+2)\theta} + \sum_{n=0}^{\infty} O_n e^{-i(n+4)\theta} + c_0 + c_1 e^{-i\theta} + c_2 e^{i\theta} + f_2 e^{i2\theta} + c_3 e^{-i2\theta} + c_4 e^{-i3\theta} + f_4 e^{-i4\theta} \right] \right\} \quad (4.26)
\end{aligned}$$

where

$$\left. \begin{aligned}
&\eta = 1/R^2, x = 1 + \eta^2, x_1 = xd_0 - \eta d_3 - \eta d_4, x_2 = xd_1 - \eta d_5 - \eta d_2, \\
&x_3 = xd_2 - \eta d_1, x_4 = xd_3 - \eta d_0, x_5 = -\eta d_0, x_6 = xd_5 - \eta d_1, \\
&x_7 = \eta d_2, x_8 = -\eta d_3, x_9 = \eta d_4 = 0, x_{10} = \eta d_5, x_{11} = 0
\end{aligned} \right\} \quad (4.27)$$

Furthermore, by equating coefficients of $e^{in\theta}$ in (4.26), we finally obtain

$$\sum_{k=0}^M W_{nk} I_{2k} = Q_n \quad (4.28)$$

Hence W_{nk} and Q_n are finally related to coefficients S_i and D_i . For example, for $M=5$ and $e^{i3\theta}$, we obtain

$$\left. \begin{aligned} W_{30} &= xP_1 - 2\eta P_3 - c_2\eta, W_{31} = xP_3 - 2\eta P_1 - \eta P_5 + c_2x - c_1\eta \\ W_{32} &= xP_5 - \eta P_3 - \eta P_7 - c_4\eta + c_1x - c_2\eta \\ W_{33} &= xP_7 - \eta P_5 - \eta P_9 + c_4x - c_1\eta - \eta O_1 \\ W_{34} &= xP_9 - \eta P_7 - \eta P_{11} - c_4\eta + xO_1 - \eta O_3 \\ W_{35} &= P_{11} - \eta P_9 - \eta O_1 + O_3, Q_3 = \frac{-x_7 + xU_1 - \eta U_3}{\Lambda} \end{aligned} \right\} \quad (4.29)$$

Depending on the level of accuracy required, we may select different values of M corresponding to a set of M linear equations and finally obtain the coefficients S_i and D_i .

4.3 NUMERICAL EXAMPLES AND DISCUSSION

4.3.1 Interfacial Stress

It is well known that the interphase layer is often the site of nucleation of damage and voids or cracks. In some instances, interfacial separation leads directly to catastrophic failure, while in other circumstances failure results from void nucleation as a result of a

sequence of inclusion decohesion events. Consequently, it is of practical interest to examine the interfacial stresses in the presence of a compliant interphase layer.

Let $b = 1$ and consider the case of a silicon matrix surrounding an aluminum inclusion. The material properties are described by (see Pottinger et al, 1994; Evans et al, 1991):

$$\alpha_1 = 2.5 \times 10^{-6} / ^\circ\text{C}; E_1 = 190 \text{ Gpa}; \nu_1 = 0.28, \mu_1 = 74.22 \text{ Gpa},$$

$$\alpha_2 = 25 \times 10^{-6} / ^\circ\text{C}; E_2 = 62 \text{ Gpa}; \nu_2 = 0.33, \mu_2 = 23.31 \text{ Gpa}$$

where, E is Young's modulus and ν is Poisson's ratio.

By the same procedure in Chapter 3, we obtain the corresponding stress field.

CASE 1 When $1 < a/b \leq 3.5$, only the coefficients $S_0(D_0)$, $S_1(D_1)$ and $S_2(D_2)$ are necessary to achieve the desired accuracy. From (4.14) and (4.15), considering (3.11), it is easy to find ϕ_2 and Ω_2 expressed in terms of $S_0(D_0)$, $S_1(D_1)$ and $S_2(D_2)$. Furthermore, ψ_2 can be obtained from (3.19). For example, in the present case

$$\phi_2(\xi) \cong -\frac{2S_1}{R^2} + \left(\frac{S_0}{R} - \frac{3S_2}{R^3}\right)\left(\frac{2z}{l}\right) + \left(\frac{S_1}{R^2}\right)\left(\frac{2z}{l}\right)^2 + \left(\frac{S_2}{R^3}\right)\left(\frac{2z}{l}\right)^3 \quad (4.30)$$

Once ϕ_2 and ψ_2 are obtained, we can calculate the stress distribution inside the inclusion . In Figures 4.1 and 4.2, the stress distribution along the interface (normal and tangential directions) in the two cases $h_1=h_2$ and $h_1=3h_2$ is plotted for the value $a/b=3.5$ and

different values of the parameter h . When $h=50$, the local stresses reach maximum values for both cases. The present computations also indicate that there is no significant difference between the cases $h_1=h_2$ and $h_1=3h_2$. Hence, for practical inclusion (structural) design, to satisfy the basic requirements we need only consider the case $h_1=h_2$.

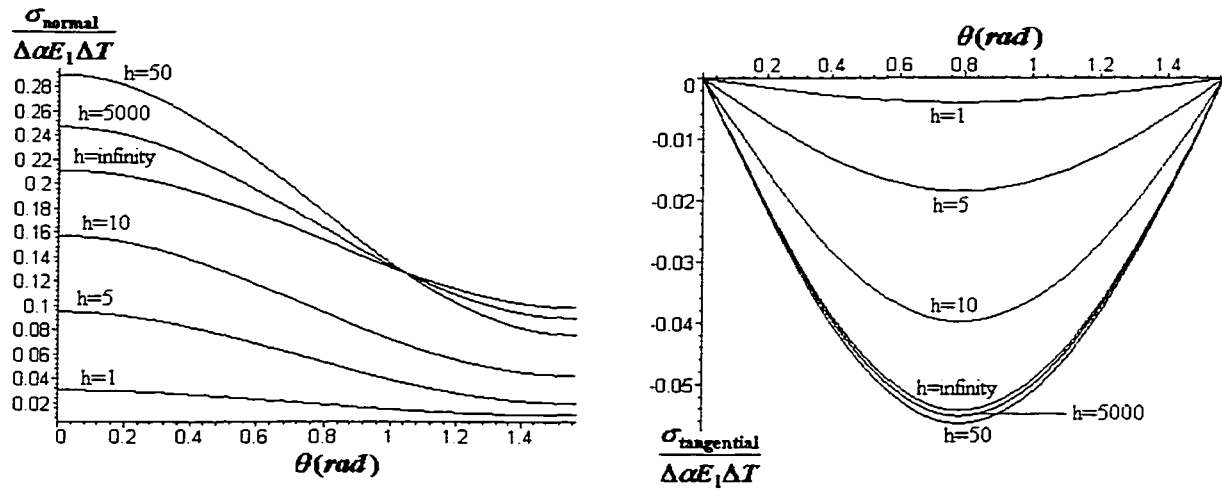


Figure 4.1: Normal and tangential stresses along the interface for $a/b=3.5$ in plane strain under a uniform change in temperature for $h_1=h_2=h$

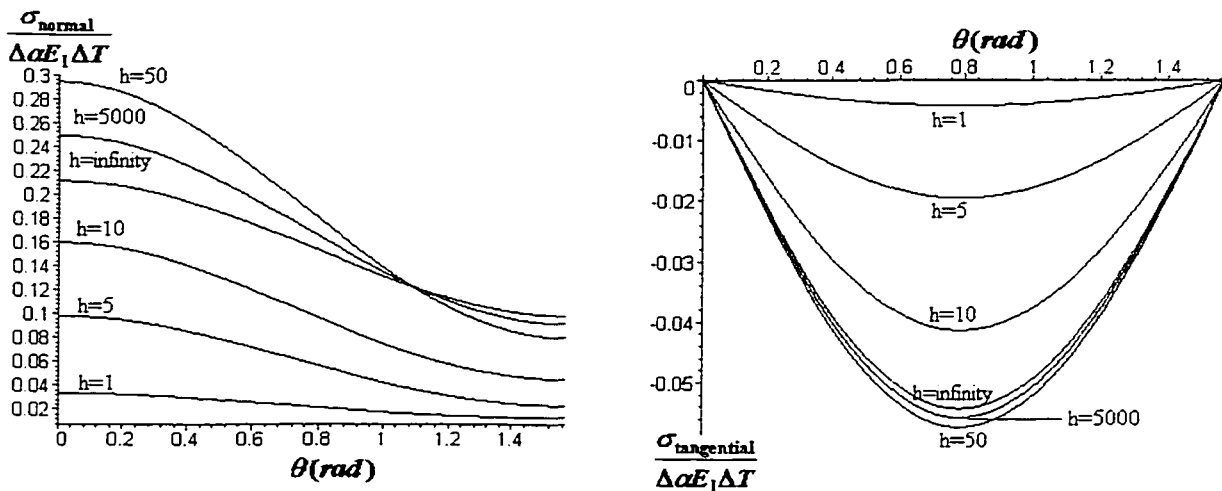


Figure 4.2: Normal and tangential stresses along the interface for $a/b=3.5$ in plane strain under a uniform change in temperature for $h_1=3h_2=h$

CASE 2 When $3.5 < a/b \leq 7$, only the coefficients $S_0(D_0)$, $S_1(D_1)$, $S_2(D_2)$ and $S_3(D_3)$ are necessary to achieve the desired accuracy. As above, we can obtain ϕ_2 , Ω_2 and ψ_2 expressed in terms $S_0(D_0)$, $S_1(D_1)$, $S_2(D_2)$ and $S_3(D_3)$. The corresponding interfacial stress distributions are presented in Figures 4.3 and 4.4.

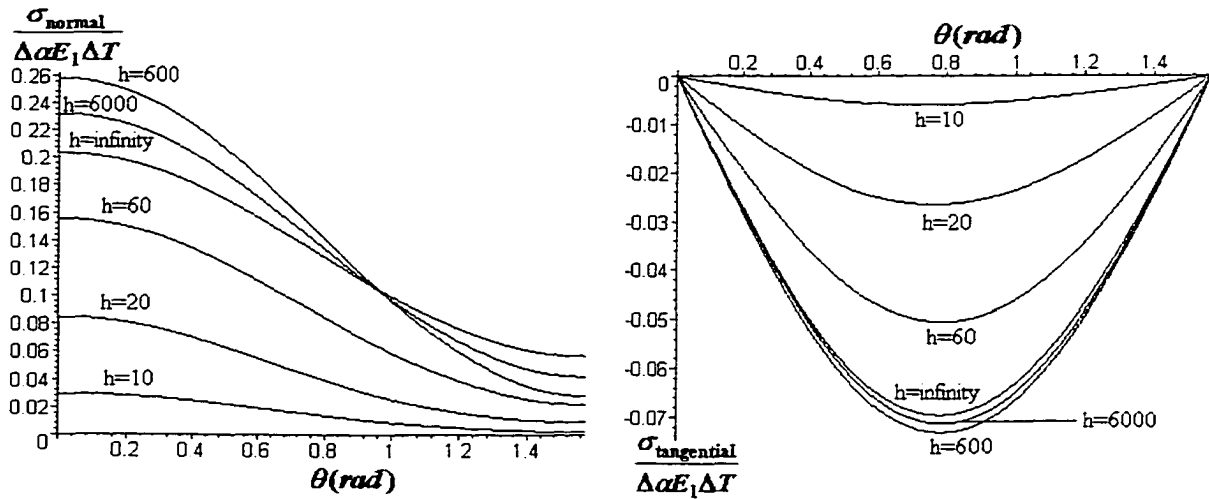


Figure 4.3: Normal and tangential stresses along the interface for $a/b=7$ in plane strain under a uniform change in temperature for $h_1=h_2=h$

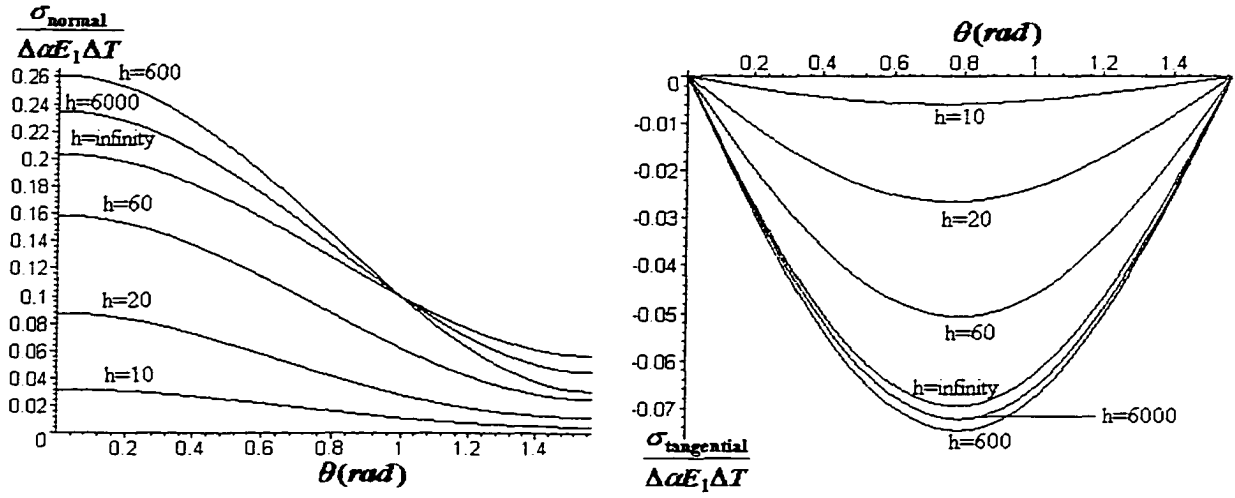


Figure 4.4: Normal and tangential stresses along the interface for $a/b=7$ in plane strain under a uniform change in temperature for $h_1=3h_2=h$

CASE 3 When $7 < a/b \leq 10$, only the coefficients $S_0(D_0)$, $S_1(D_1)$, $S_2(D_2)$, $S_3(D_3)$ and $S_4(D_4)$ are necessary to achieve the desired accuracy. Again, we can obtain ϕ_2 , Ω_2 and ψ_2 expressed in terms of $S_0(D_0)$, $S_1(D_1)$, $S_2(D_2)$, $S_3(D_3)$ and $S_4(D_4)$. The corresponding interfacial stress distributions are presented in Figures 4.5 and 4.6.

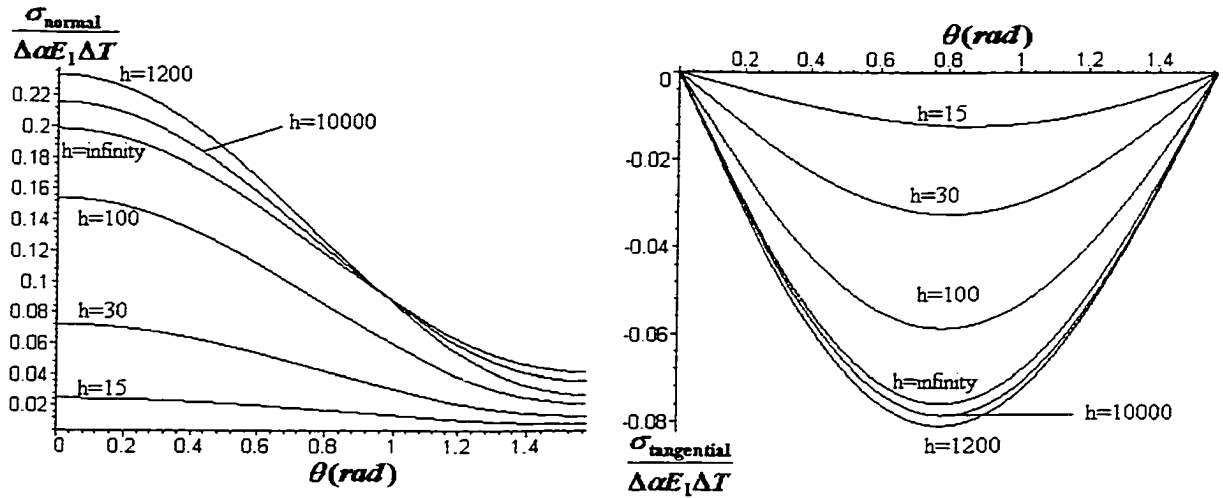


Figure 4.5: Normal and tangential stresses along the interface for $a/b=10$ in plane strain under a uniform change in temperature for $h_1=h_2=h$

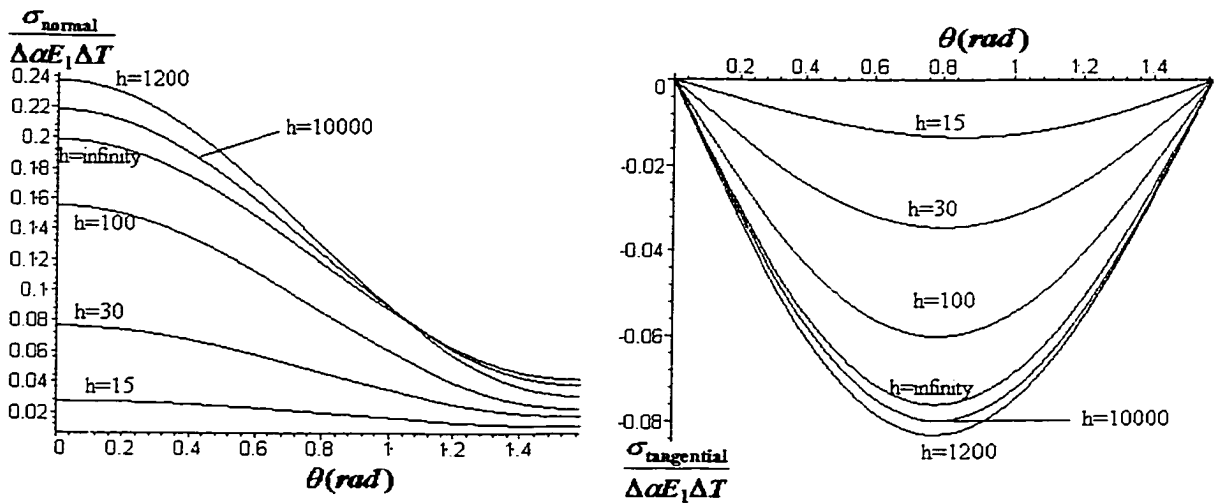


Figure 4.6: Normal and tangential stresses along the interface for $a/b=10$ in plane strain under a uniform change in temperature for $h_1=3h_2=h$

It is noted that for values $a/b > 10$ of the aspect ratio, the procedure is similar although a much larger number of coefficients is required to evaluate the corresponding series to the desired accuracy.

From Figures 4.1 to 4.6, it is clear that the homogeneously imperfect interface parameter h significantly influences the stress distribution although the aspect ratio of the elliptic inclusion does not significantly change the locations of the maximum normal and tangential tractions along the interface and their magnitudes. It is found that the normal stresses are always positive along the entire interface. Consequently, any possible overlapping associated with the imperfect interface model used in this chapter (see, Achenbach & Zhu 1990 and Hashin 1991b) cannot occur in the present thermal stress problem.

Again, since Figures 4.1 to 4.6 show no significant difference in the results obtained between the cases $h_1 = h_2$ and $h_1 = 3h_2$, the following discussions are based on the results from the case $h_1 = h_2$ or $h_1 = 3h_2$.

By using the same procedure in Chapter 3, we first calculate the peak resultant traction (stress) along the interface (henceforth referred to as the peak traction).

The peak traction is found by calculating the maximum value of the resultant traction $\sigma_{\text{resultant}} / \Delta\alpha E_1 \Delta T$ (see, Hu 1991) along the interface for a given aspect ratio and a given value of the parameter h . Here, $\sigma_{\text{resultant}}$ is defined by the relation

$$\sigma_{\text{resultant}} = \sqrt{\sigma_{\text{normal}}^2 + \sigma_{\text{tangential}}^2} \quad (4.31)$$

and $\Delta\alpha E_1 \Delta T$ represents the stress induced by the uniform change (cooling) in the matrix temperature. This peak traction is found always to occur at the point $\theta = 0$. Figure 4.7 plots the peak traction as a function of the imperfect interface parameter h for different aspect ratios.

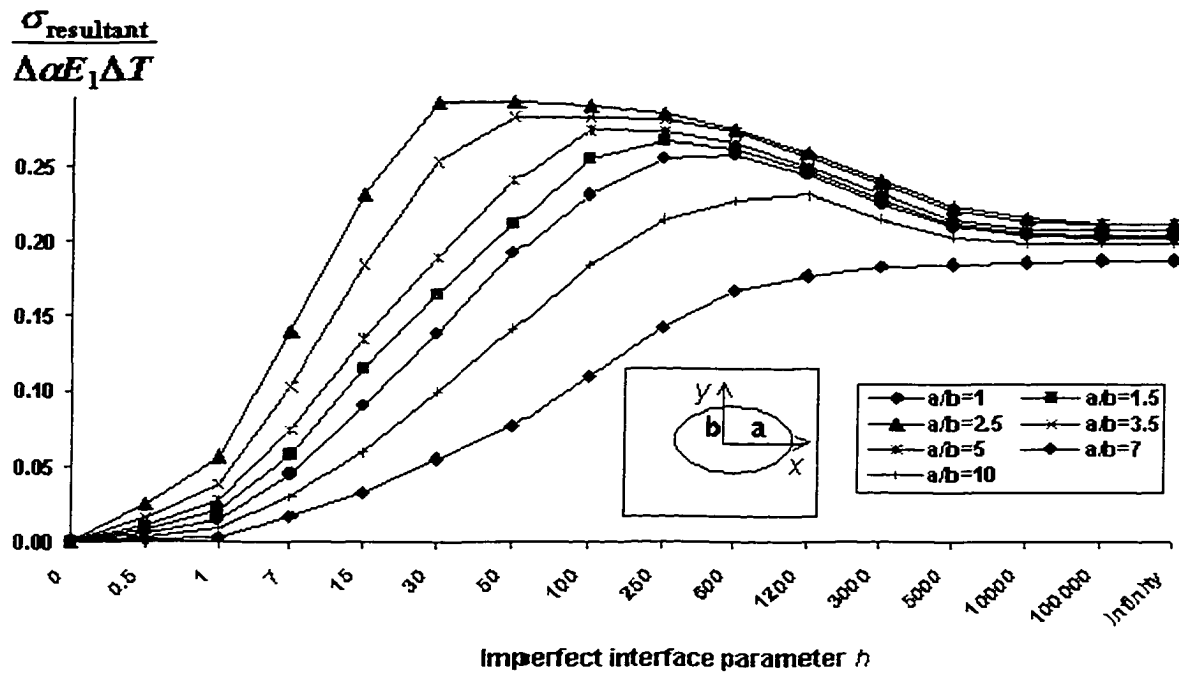


Figure 4.7: The peak resultant traction along the interface varies as a function of the imperfect interface parameter h in plane strain under a uniform change in temperature for

$$h_1 = 3h_2 = h$$

From Figure 4.7, we may obtain the same conclusions as in Chapter 3: for each aspect ratio (except $a/b=1$), the peak traction is a non-monotonic function of the interface parameter h . Consequently, for each aspect ratio, there is a unique value of the interface

parameter h which corresponds to maximum peak traction. The collection of these values of h define the parameter h^* (see Figure 4.12).

Next we consider the strain energy density criterion used by Achenbach & Zhu (1990). As mentioned before, for the simple interphase model considered here, the strain energy criterion is particularly appropriate since it includes the effects of both normal and shear tractions across the interphase. The energy per unit interphase, U , is defined as:

$$U = \frac{\sigma_{\text{normal}}^2}{2h_1} + \frac{\sigma_{\text{tangential}}^2}{2h_2}$$

By introducing $\bar{\sigma}_{\text{normal}} = \sigma_{\text{normal}} / \Delta\alpha E_1 \Delta T$ and $\bar{\sigma}_{\text{tangential}} = \sigma_{\text{tangential}} / \Delta\alpha E_1 \Delta T$, we obtain, in dimensionless form:

$$\bar{U} = \frac{\bar{\sigma}_{\text{normal}}^2}{2h_1} + \frac{\bar{\sigma}_{\text{tangential}}^2}{2h_2} \quad (4.32)$$

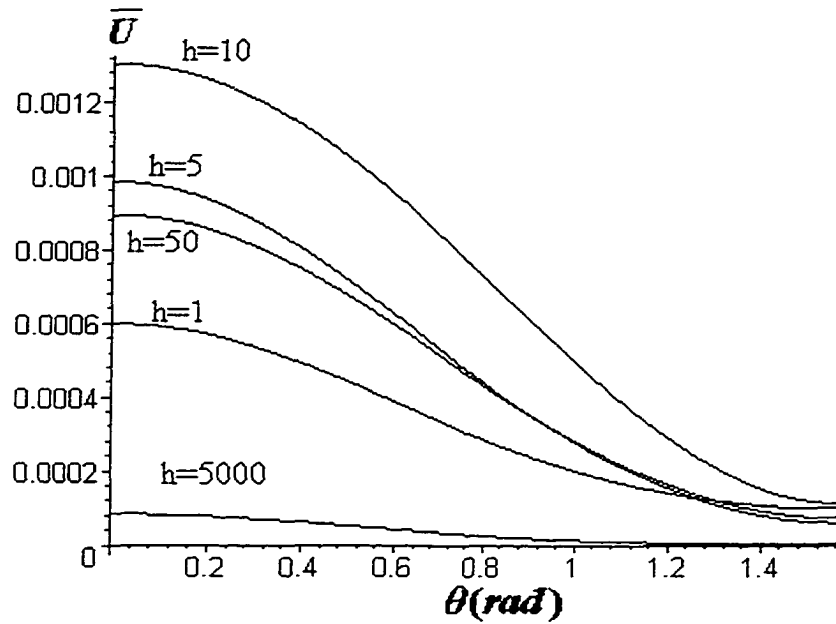


Figure 4.8: The interfacial strain energy (\bar{U}) along the interface for $a/b=3.5$ in plane strain under a uniform change in temperature for $h_1=3h_2=h$

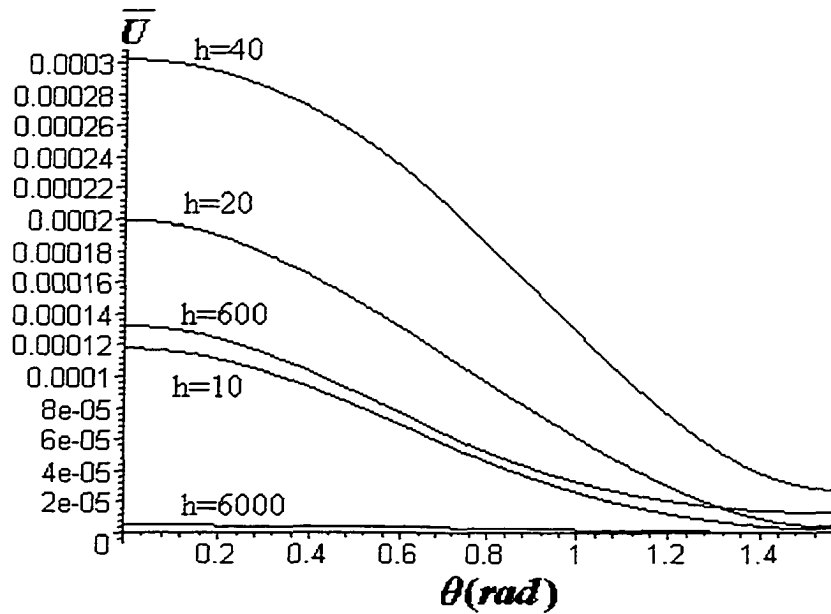


Figure 4.9: The interfacial strain energy (\bar{U}) along the interface for $a/b=7$ in plane strain under a uniform change in temperature for $h_1=3h_2=h$

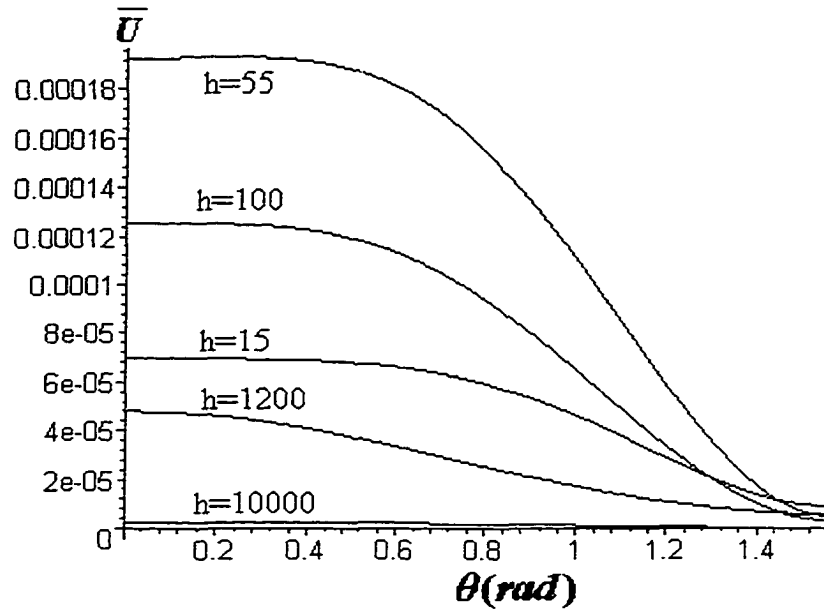


Figure 4.10: The interfacial strain energy (\bar{U}) along the interface for $a/b=10$ in plane strain under a uniform change in temperature for $h_1=3h_2=h$

It is now reasonable to assume that the interface will fail when \bar{U} reaches a critical value, \bar{U}_{cr} , which depends on the material properties. Figures 4.8, 4.9, 4.10 plot the interfacial strain energy distribution along the interface for different aspect ratios of the ellipse in the case $h=h_1=3h_2$. It is shown that the compliant layer (described by the homogeneously imperfect interface parameter h) does significantly influence the interfacial strain energy distribution. In particular, when h reaches a specific value, the peak interfacial strain energy reaches its maximum value.

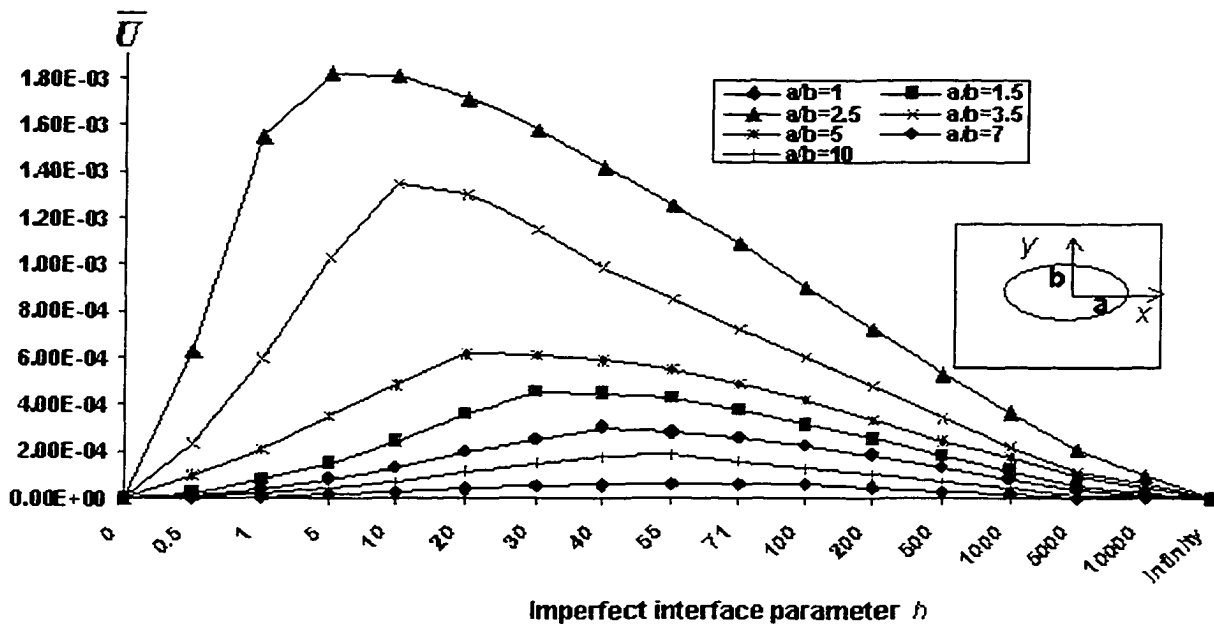


Figure 4.11: The interfacial strain energy density varies as a function of the imperfect interface parameter h in plane strain under a uniform change in temperature for $h_1=3h_2=h$

Figure 4.11 plots the peak (defined as in the case of peak traction above) strain energy per unit interphase \bar{U} as a function of the imperfect interface parameter $h(=h_1=3h_2)$. It is clear from Figure 4.11 that \bar{U} is again a non-monotonic function of the interface parameter h . This means that we can again define a new parameter h^* defined by values of h which correspond to maximum values of the peak strain energy per unit interphase along the inclusion-matrix interface (see Figure 4.13).

Since values of h^* correspond to local maximum peak stresses and maximum peak values of \bar{U} and are related to the mechanical properties and thickness of the adhesive layer between the inclusion and the matrix, the parameter h^* may be used as a control parameter when designing "thermal inclusions"(see Hu 1991). For example, in the case of

a uniform change (cooling) in temperature and the aspect ratio $a/b=1$ (circular inclusion), the peak traction in Figure 4.7 corresponds to the value $h^*=\infty$ (perfect bonding). However, when $a/b=3.5$, the peak traction corresponds to $h^*=50$. Since h^* is rendered dimensionless by division by μ_1/b , for a specific aspect ratio, we can avoid the maximum peak traction, or indeed minimize the maximum peak traction by adjusting mechanical properties and the thickness of the interphase layer (related to b).

In addition, from Figures 4.7 and 4.11, we note that the effect of the interphase layer (the interface parameter h) on the peak traction and peak strain energy density is sensitive to small aspect ratios (≤ 5) of the elliptic inclusion, but not to larger values of a/b . It should be emphasized that in the present case, the normal stresses are always dominant compared to the shear stresses (see Figures 4.1-4.7). This explains why other parameters such as the interfacial strain energy are not significantly affected when we use different values of h_2 (which is related to the shear stress).

The relationship between the parameter h^* and the aspect ratio a/b is presented in Figures 4.12 and 4.13 for the two different failure criteria.

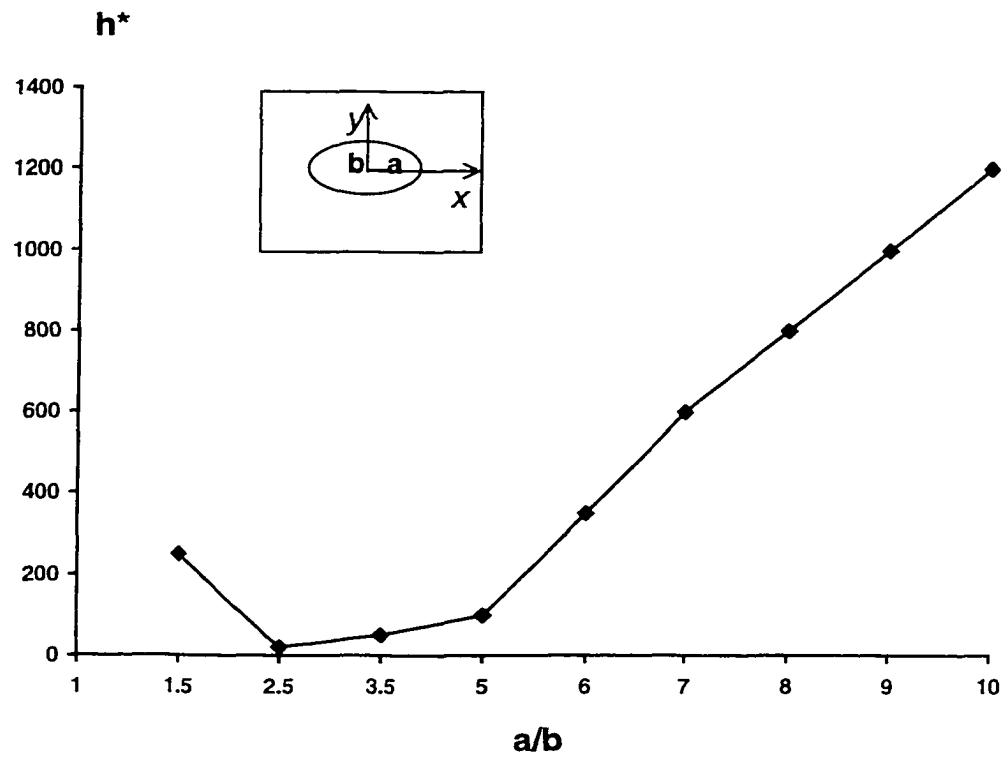


Figure 4.12: The relationship between h^* and a/b using the resultant traction criterion

when $h_1 = 3h_2 = h$.

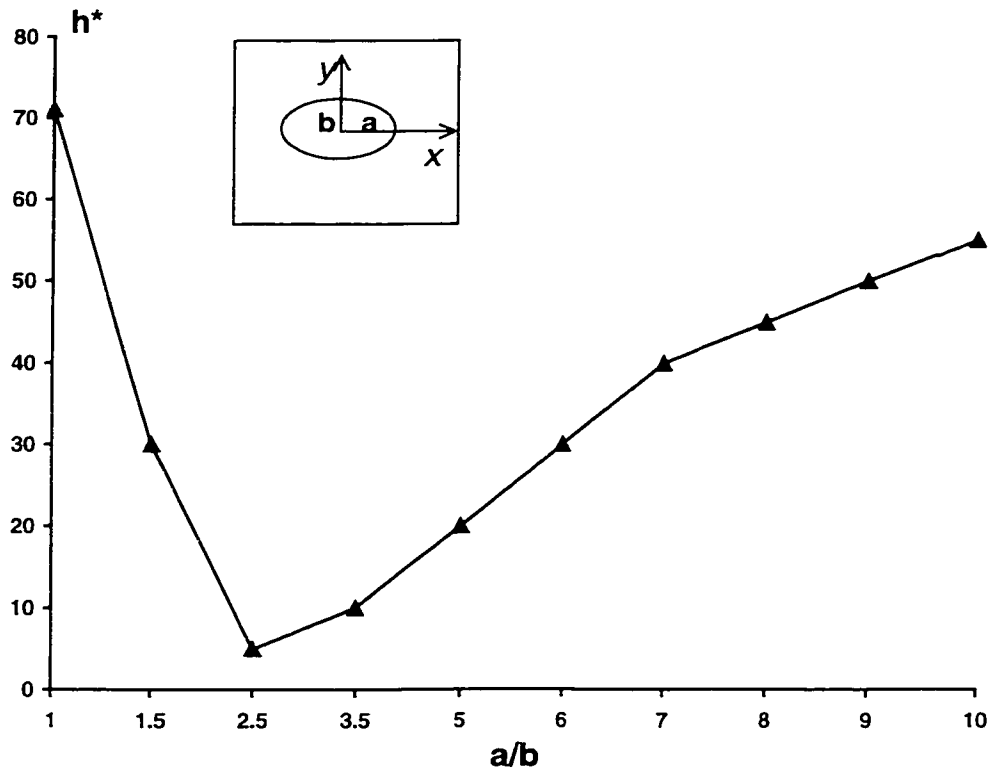


Figure 4.13: The relationship between h^* and a/b using the interfacial strain energy density criterion for $h_1 = 3 h_2 = h$.

4.3.2 Internal Stress Distribution

The thermal mismatch induced residual internal stresses which arise in thin metal layers can be extremely large (see, for example, Spaepen & Shull, 1996; Thompson, 1996; Thouless et al, 1993; Besser et al, 1994; Venkatraman et al, 1990). These stresses are sensitive to variables such as layer thickness, thermal treatment and the presence of a passivation (see, for example, Shull & Spaepen, 1996; Venkatraman et al, 1990). For example, the reliability of microelectronic devices is strongly influenced by the internal stresses which develop in the interconnect structures. Sources of such internal stresses include: (a) thermal expansion/contraction mismatch between dissimilar materials, such as the interconnect, dielectric and passivation layers, caused by temperature excursions introduced during processing, manufacture and service, (b) non-equilibrium conditions, (c) various mechanical processes used to create geometrical and topological changes during etching and patterning of interconnect lines and during planarization, (d) diffusion and chemical reactions which occur at and across interfaces during thermal excursions, (e) the passage of electric current in the conduction lines which introduces nonuniform atomic transport and (f) the absorption of substances such as water vapor. Consequently, in the present section, we consider the effect of a compliant interphase layer on internal thermal stresses arising from a uniform change in temperature. Using complex variable techniques, we obtain infinite series representations of both the thermal mean stress and von Mises equivalent stress which, when evaluated numerically, demonstrate how each varies with the parameter h describing the compliant layer. Remarkably, both the peak mean stress and peak von Mises stress are found to be non-

monotonic functions of h . This allows us to identify, in each case, a specific value h^* of the interface parameter h which corresponds to maximum peak stress. We also obtain another value h^R of h below which the peak (mean or von Mises) stress within the inclusion is smaller than that corresponding to a perfect interface. In particular, when the interphase layer is designed so that the value of h is close to unity, the internal peak thermal stress is reduced to a fraction of its original value in the absence of the interphase layer.

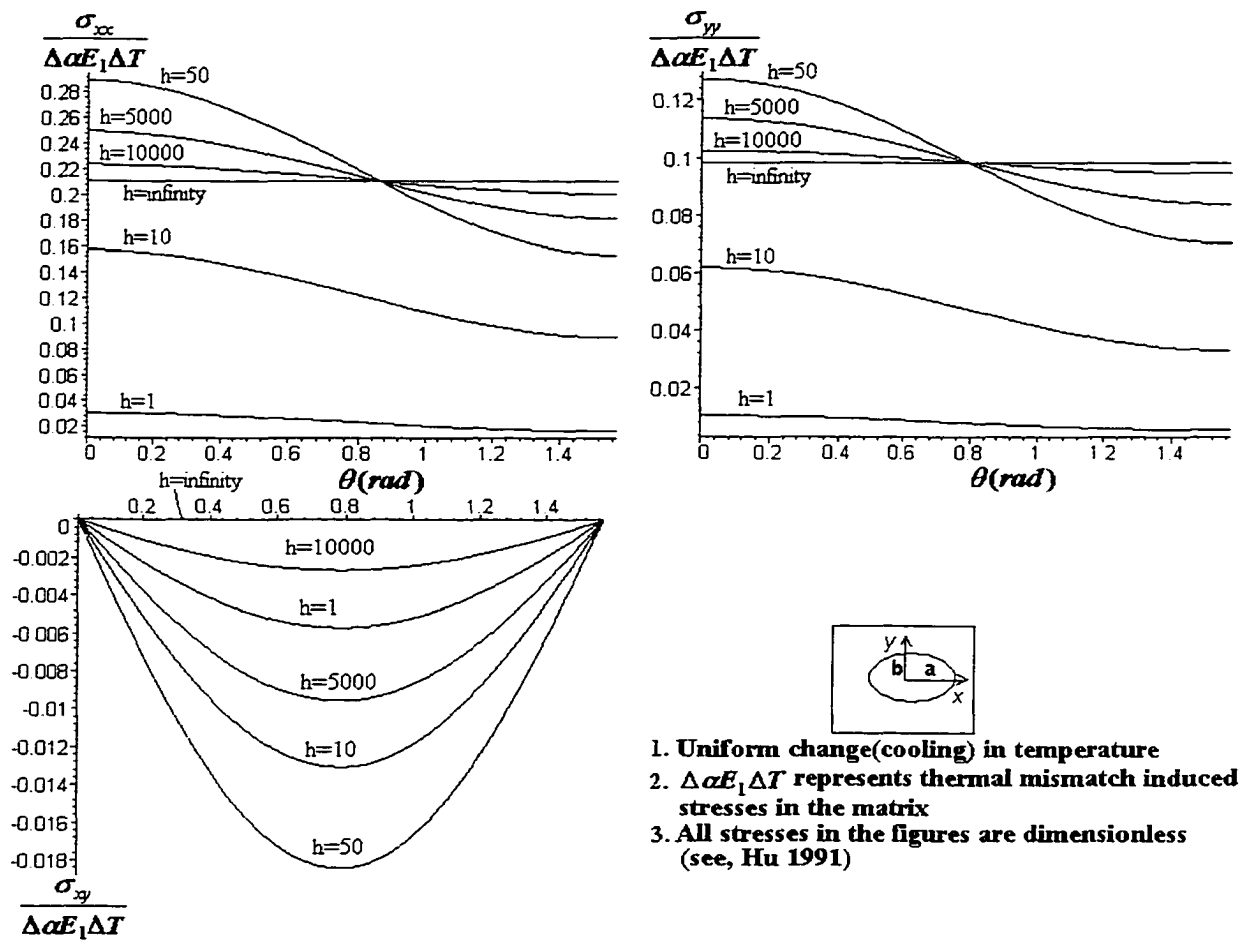
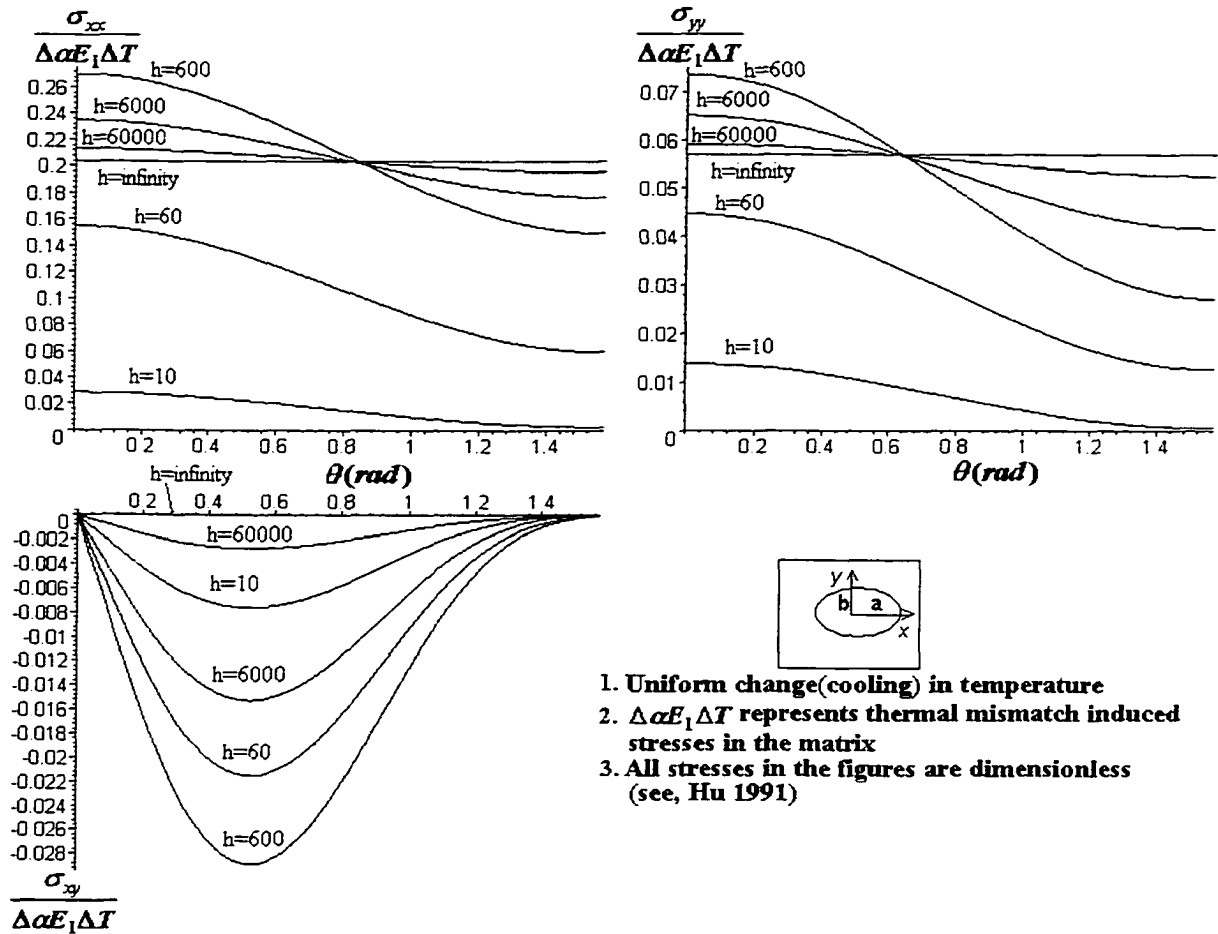


Figure 4.14: Non-uniformity of internal stresses along the interface for $a/b=3.5$ in plane strain under a uniform change in temperature for $h_1=h_2=h$



1. Uniform change (cooling) in temperature
2. $\Delta\alpha E_1 \Delta T$ represents thermal mismatch induced stresses in the matrix
3. All stresses in the figures are dimensionless (see, Hu 1991)

Figure 4.15: Non-uniformity of internal stresses along the interface for $a/b=7$ in plane strain under a uniform change in temperature for $h_1=h_2=h$

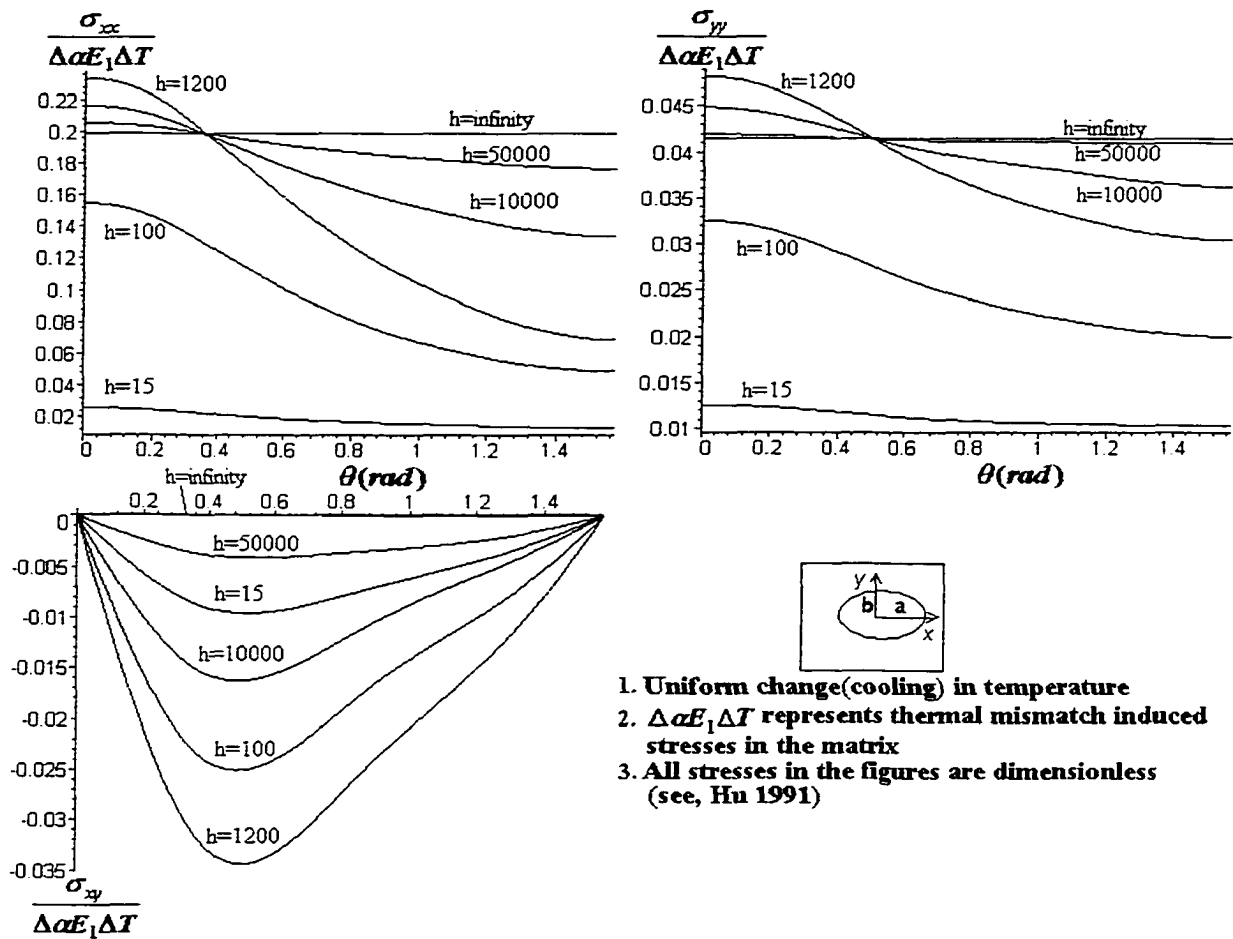


Figure 4.16: Non-uniformity of internal stresses along the interface for $a/b=10$ in plane strain under a uniform change in temperature for $h_1=h_2=h$

From Figures 4.14 – 4.16, it is clear that the non-uniformity of the stresses inside the inclusion is very strong and that the homogeneously imperfect interface parameter h ($\neq \infty$) significantly changes the stress distribution inside the inclusion. The local stresses reach peak value at $\theta = 0$. Henceforth, we denote by h^* the particular value of the imperfect interface parameter h corresponding to maximum peak stress. For

example, for $a/b=3.5$, from Figure 4.14, the maximum peak stress corresponds to the value $h=h^*=50$.

4.3.3 Mean Stresses and Von Mises Stresses

By using the same procedure in Section 3.3.4 in Chapter 3, we obtain the mean stress and von Mises stress. Figure 4.17 plots the stress distribution along the x and y axes for an elliptic inclusion with aspect ratio $a/b=3.5$ under a uniform change in temperature. It is indicated that the maximum stresses in the case of σ_{xx} occur along the interface.

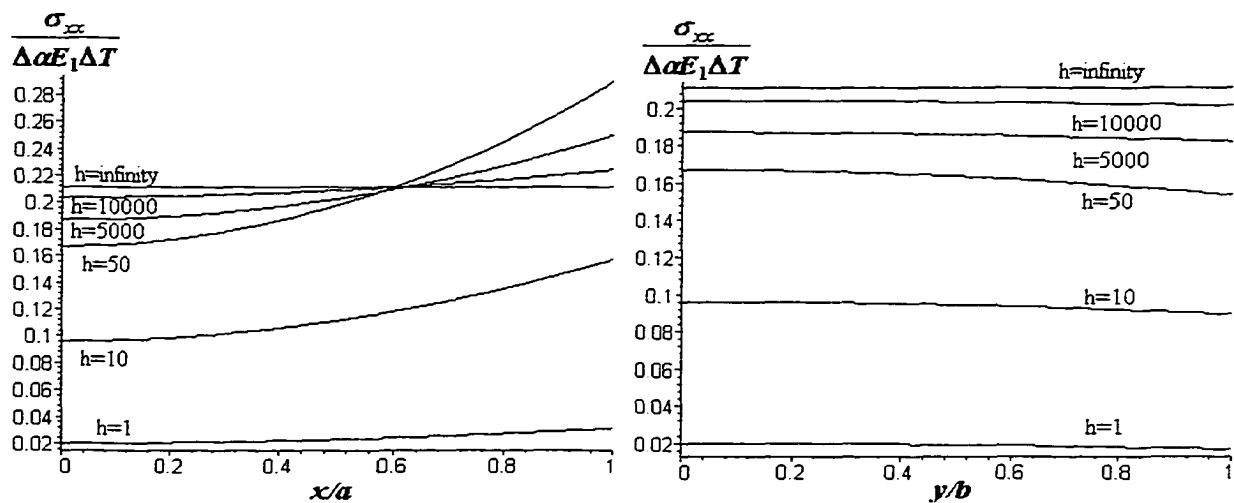


Figure 4.17: The stress distribution along the x and y axes for $a/b=3.5$ in plane strain under a uniform change in temperature for $h_1=h_2=h$

Firstly, we calculate the mean stress (defined in Eq. (3.45)) along the interface. Figures 4.18, 4.19 and 4.20 plot the stress distributions for the mean stress for different values of a/b . Again, from Figures 4.18, 4.19 and 4.20, it is clear that the mean stress inside the inclusion is non-uniform for different values of the imperfect interface parameter h ($\neq \infty$). The local mean stresses again reach peak values at $\theta = 0$. The specific values of h^* (corresponding to maximum peak stress) are the same as those obtained in Figures 4.14, 4.15 and 4.16.

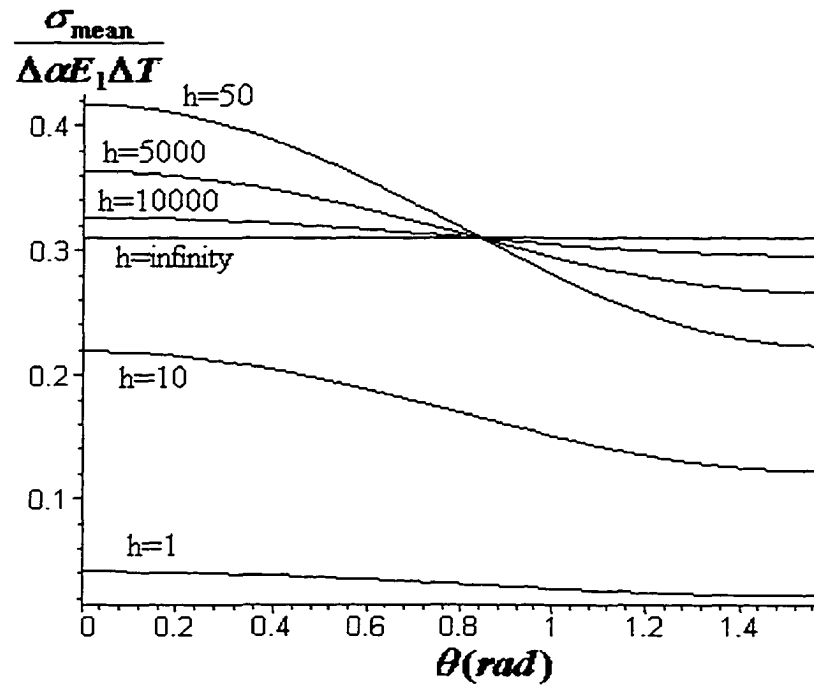


Figure 4.18: Non-uniformity of mean stresses along the interface for $a/b=3.5$ in plane strain under a uniform change in temperature for $h_1=h_2=h$

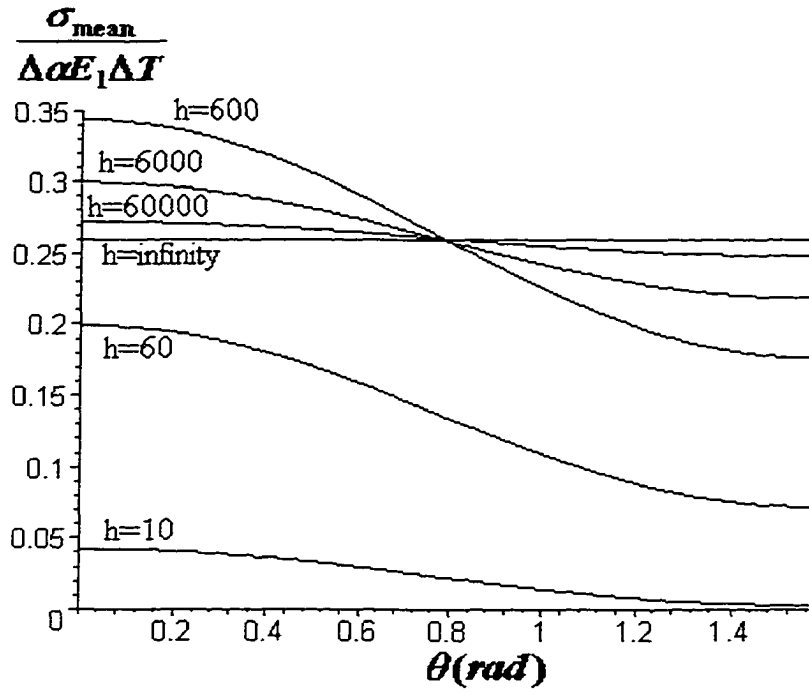


Figure 4.19: Non-uniformity of mean stresses along the interface for $a/b=7$ in plane strain under a uniform change in temperature for $h_1=h_2=h$

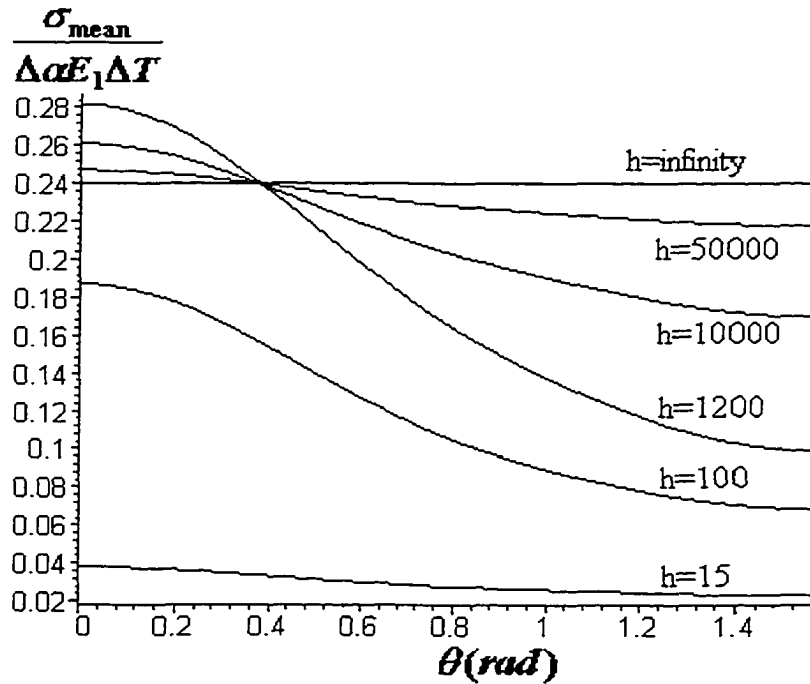


Figure 4.20: Non-uniformity of mean stresses along the interface for $a/b=10$ in plane strain under a uniform change in temperature for $h_1=h_2=h$

Similarly, next, we calculate the von Mises equivalent stress (defined in Eq. (3.46)). Figures 4.21, 4.22 and 4.23 plot the von Mises equivalent stress distributions along the interface for different values of the aspect ratio a/b . From Figures 4.21, 4.22 and 4.23, it is clear that the von Mises equivalent stresses inside the inclusion are non-uniform for different values of the imperfect interface parameter h ($\neq \infty$). The local von Mises equivalent stresses again attain peak values at $\theta = 0$. The specific values of h^* (corresponding to maximum peak von Mises stress) are different from those in Figures 4.14 – 4.16.

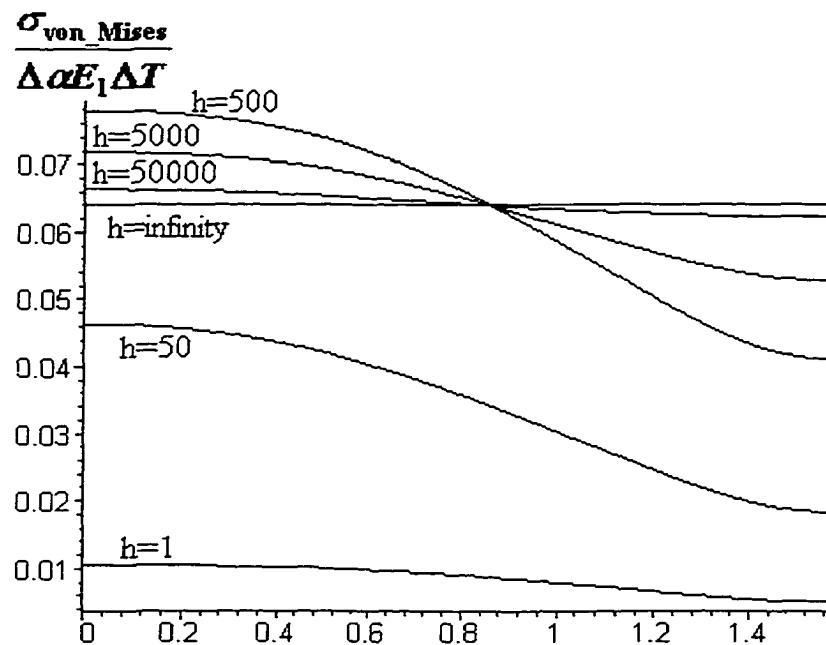


Figure 4.21: Non-uniformity of the von Mises stresses along the interface for $a/b=3.5$ in plane strain under a uniform change in temperature for $h_1=h_2=h$

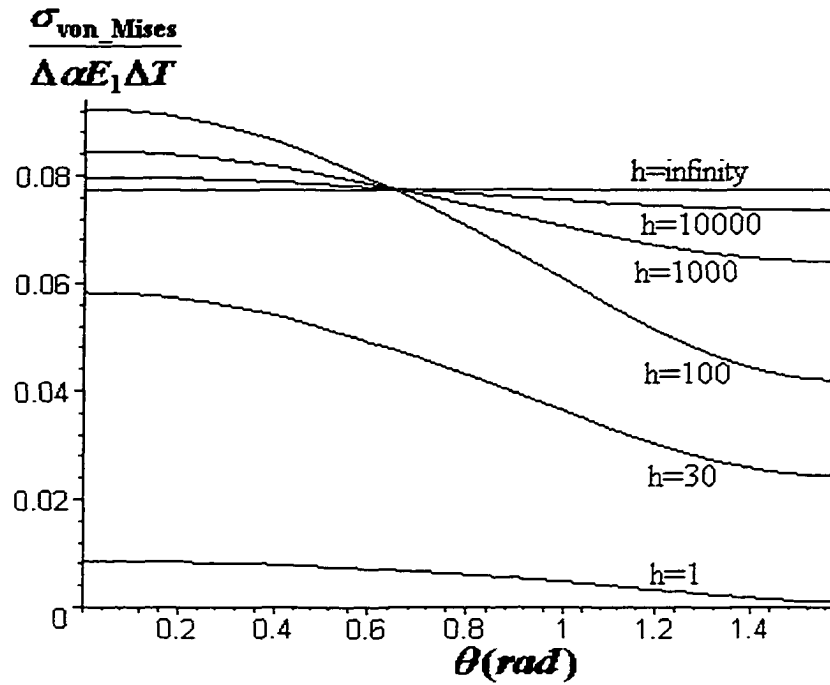


Figure 4.22: Non-uniformity of the von Mises stresses along the interface for $a/b=7$ in plane strain under a uniform change in temperature for $h_1=h_2=h$

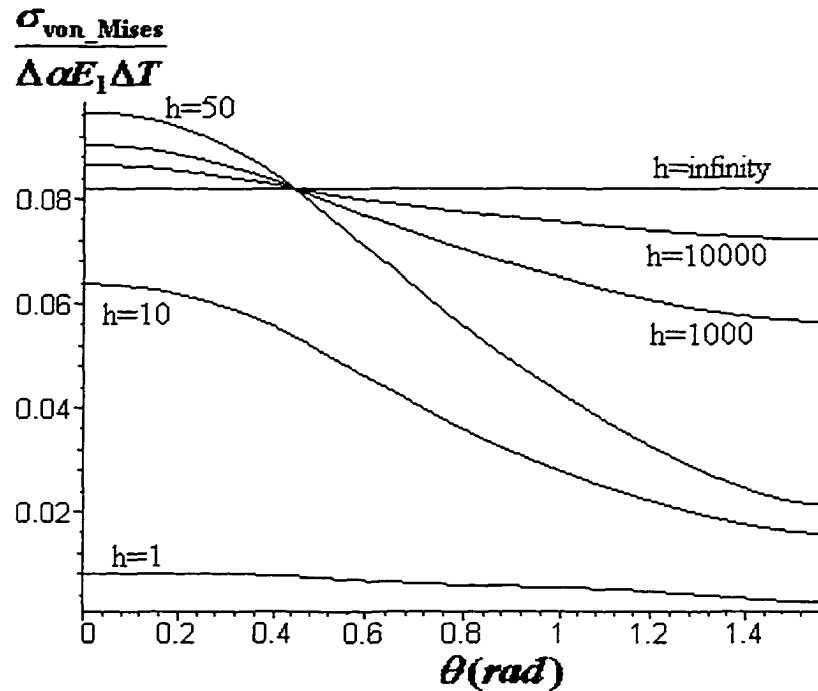


Figure 4.23: Non-uniformity of the von Mises stresses along the interface for $a/b=10$ in plane strain under a uniform change in temperature for $h_1=h_2=h$

Again, Figure 4.24 plots the peak mean stress as a function of the imperfect interface parameter h . This peak mean stress is calculated at the value $\theta = 0$. However, using the von Mises stress criteria, we obtain very different values of h^* when using mean stress and local stress criteria. Figure 4.25 plots the peak von Mises stress as a function of the imperfect interface parameter h . This peak von Mises stress is calculated at the value $\theta = 0$.

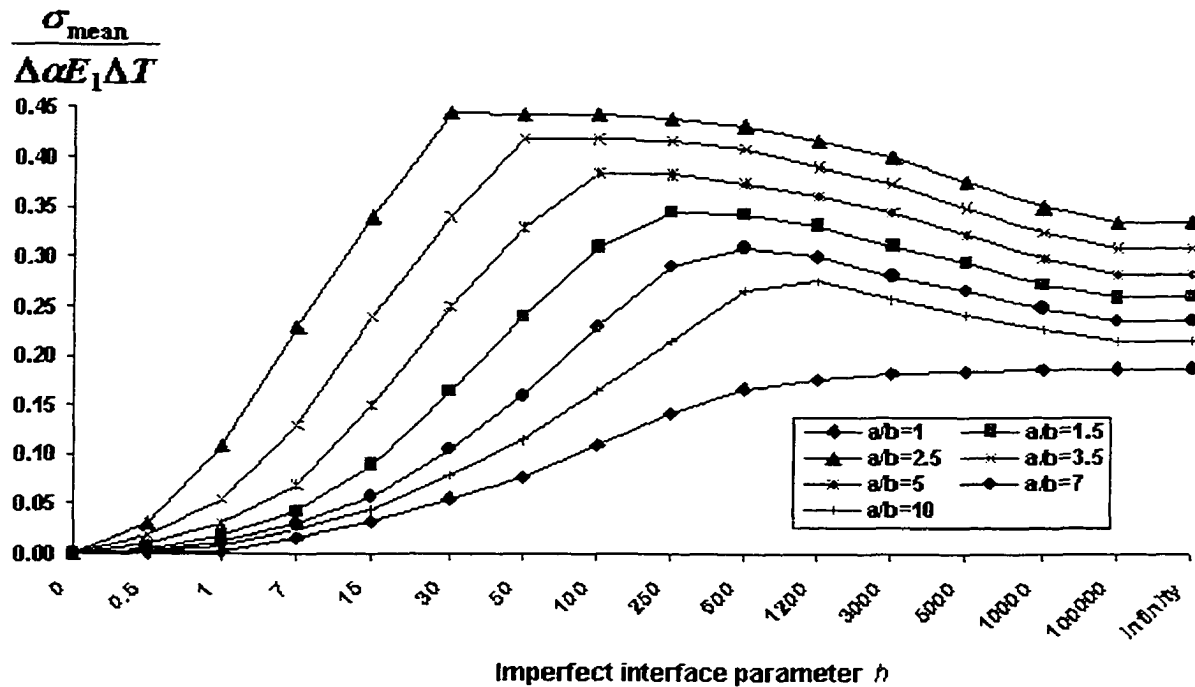


Figure 4.24: The peak mean stress at the interface varies as a function of the imperfect interface parameter h in plane strain under a uniform change in temperature for $h_1=h_2=h$

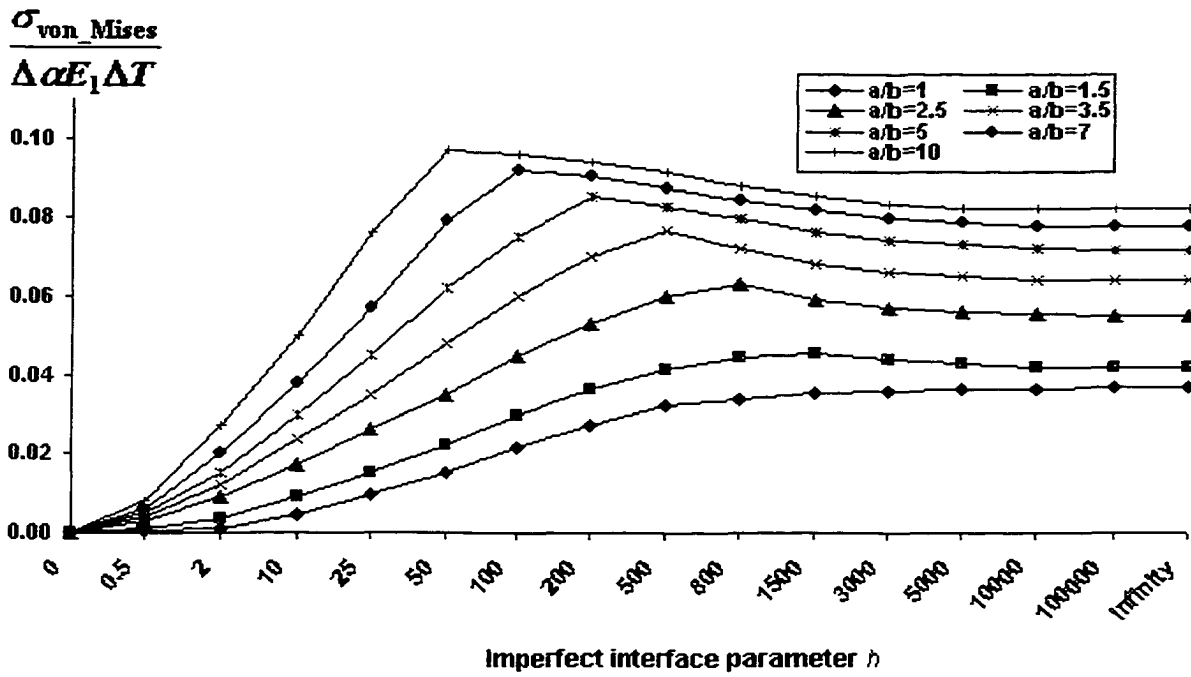


Figure 4.25: The peak von_Mises stress at the interface varies as a function of the imperfect interface parameter h in plane strain under a uniform change in temperature for

$$h_1=h_2=h$$

The maximum peak mean and von Mises stress in Figures 4.24,4.25 corresponds to values of the parameter h^* . For the circular inclusion, we know that the maximum peak mean and von Mises stress is realized at $h = \infty$ (see Ru 1998b). However, for the elliptic inclusion, the maximum peak mean and von Mises stress is related to the imperfect interface parameter and the aspect ratio of the inclusion.

Again, since values of h^* correspond to local maximum peak stresses (mean and von Mises stresses) and are related to the mechanical properties and thickness of the adhesive layer between the inclusion and the matrix, the parameter h^* may be used as a control parameter when designing "thermal inclusions" (see Hu 1991). For example, in the case

of a uniform change (cooling) in temperature and the aspect ratio $a/b=1$ (circular inclusion), the peak mean traction in Figure 4.24 corresponds to the value $h^*=\infty$ (perfect bonding). However, when $a/b=3.5$, the peak traction corresponds to $h^*=50$.

It should be noted that our computations indicate that the mean stress is a non-monotonic function of the aspect ratio a/b (see Figure 4.24), but that the von Mises stress is indeed a monotonic function of a/b (see Figure 4.25).

In order to study how we might reduce the thermal stresses, we will compare the results presented in Figures 4.24 and 4.25 with the corresponding results from the case of perfect bonding. It is noted that the peak mean and peak von Mises stresses go through the same values as they do in the case of perfect bonding before reaching maximum values. The corresponding value of h is denoted by h^R . This implies that we can reduce the thermal stress as long as we keep $h < h^R$. For example, for $a/b=2.5$, when we select $h=1$ (corresponding to a reasonably thick interphase layer, i.e. a thickness of about 1/5 the size of the inclusion), the thermal stress may be reduced to a fraction of its original value (obtained in the case of perfect bonding). This conclusion is the same as in Ru et al (1999) for anti-plane shear. This conclusion also proves that by inserting a compliant (very soft) layer between the inclusion and the matrix we can significantly reduce the thermal stress. Figures 4.26 and 4.27 are plotted using the same values obtained in the case of perfect bonding once h reaches h^R .

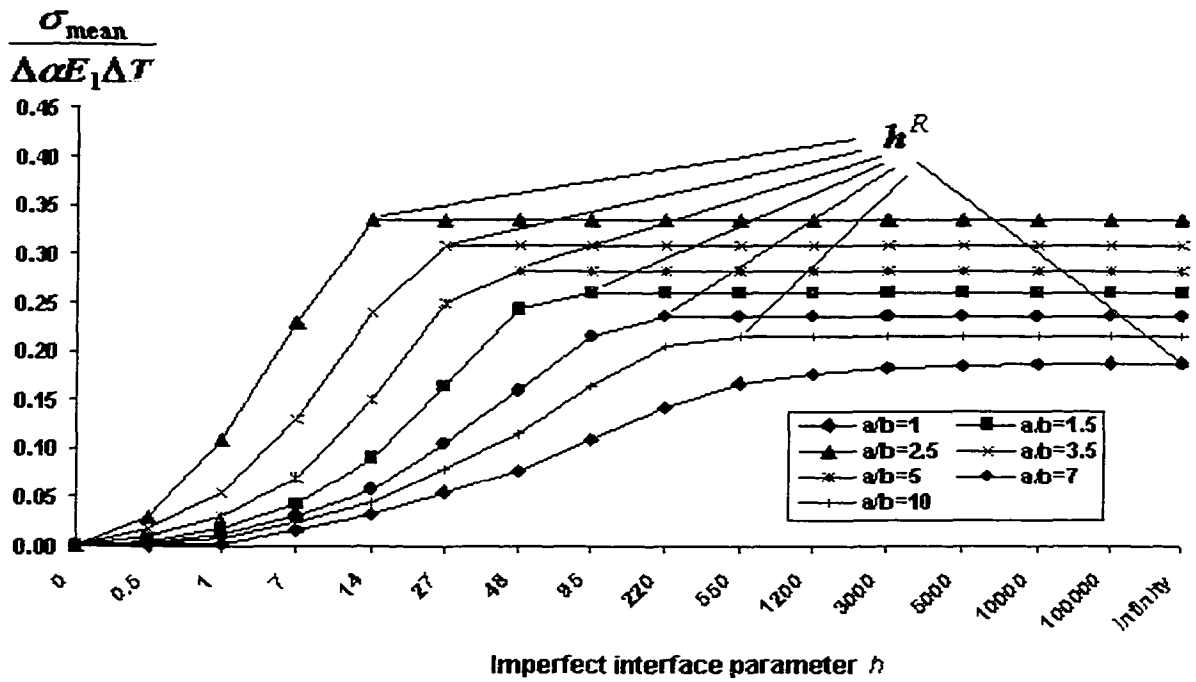


Figure 4.26: The critical mean stress (corresponding to h^R) at the interface varies as a function of the imperfect interface parameter h in plane strain under a uniform change in temperature for $h_1=h_2=h$

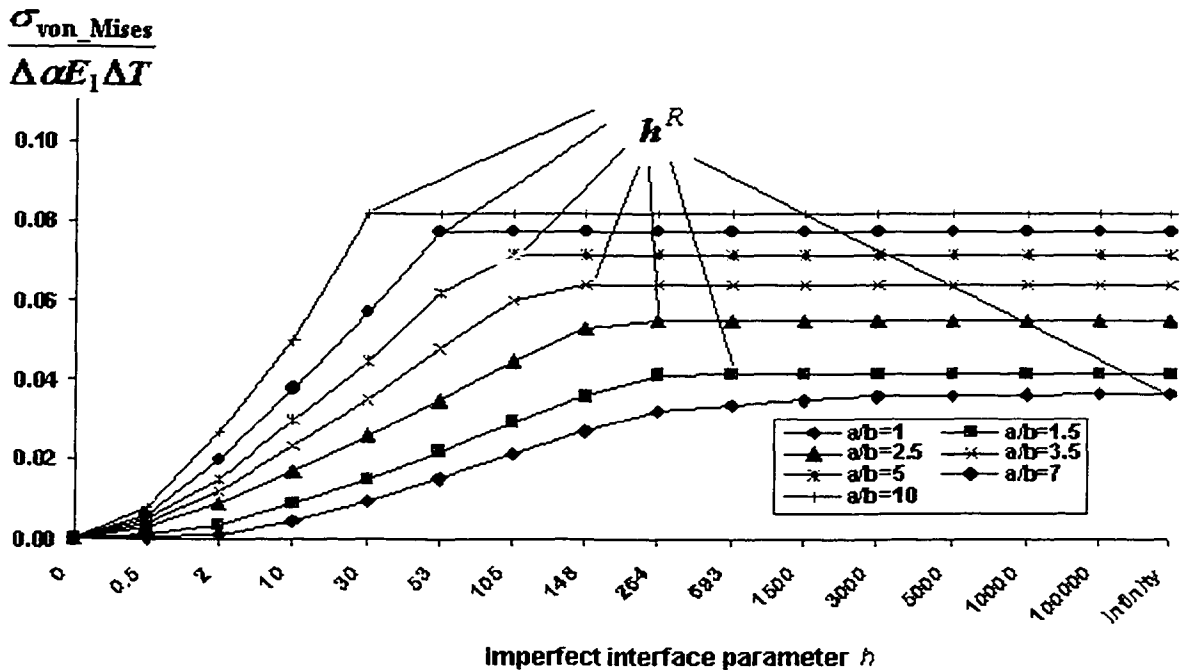


Figure 4.27: The critical von_Mises stress (corresponding to h^R) at the interface varies as a function of the imperfect interface parameter h in plane strain under a uniform change in temperature for $h_1=h_2=h$

Since h^* is rendered dimensionless by division by μ_1/b , for a specific aspect ratio, we could avoid the maximum peak stress, or indeed minimize the maximum peak stress by adjusting mechanical properties and the thickness of the interphase layer (related to b). The relationship between the parameter h^* and the aspect ratio a/b is given in Figures 4.28 and 4.29.

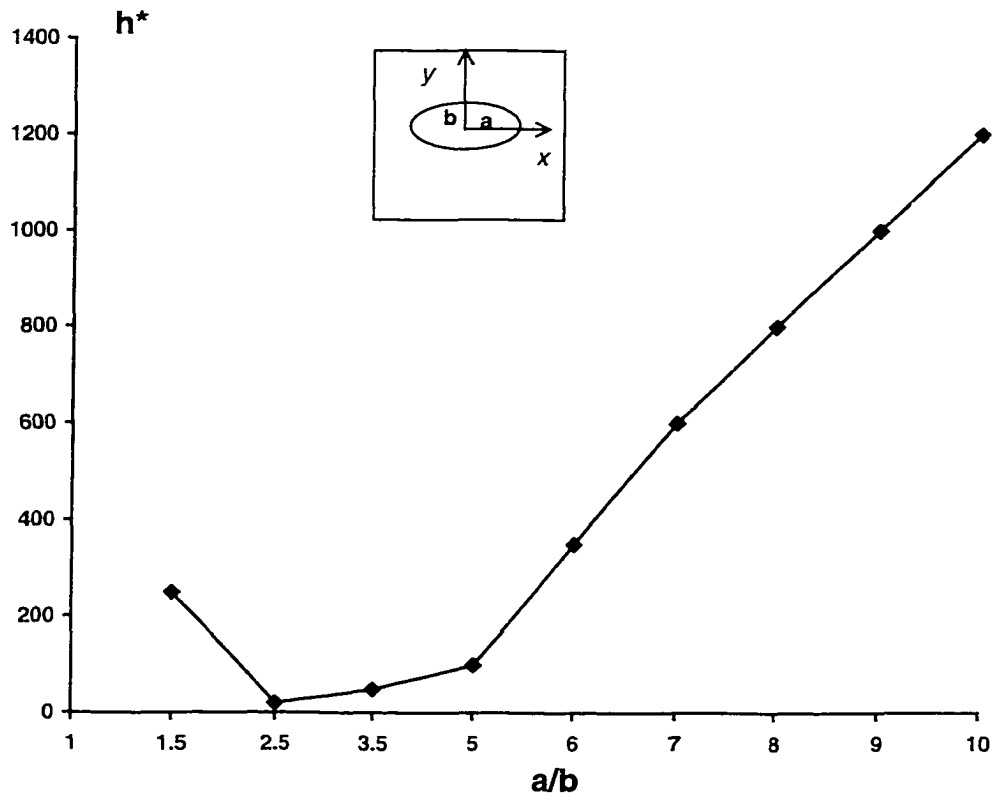


Figure 4.28: The relationship between h^* and a/b for the mean stress' criterion

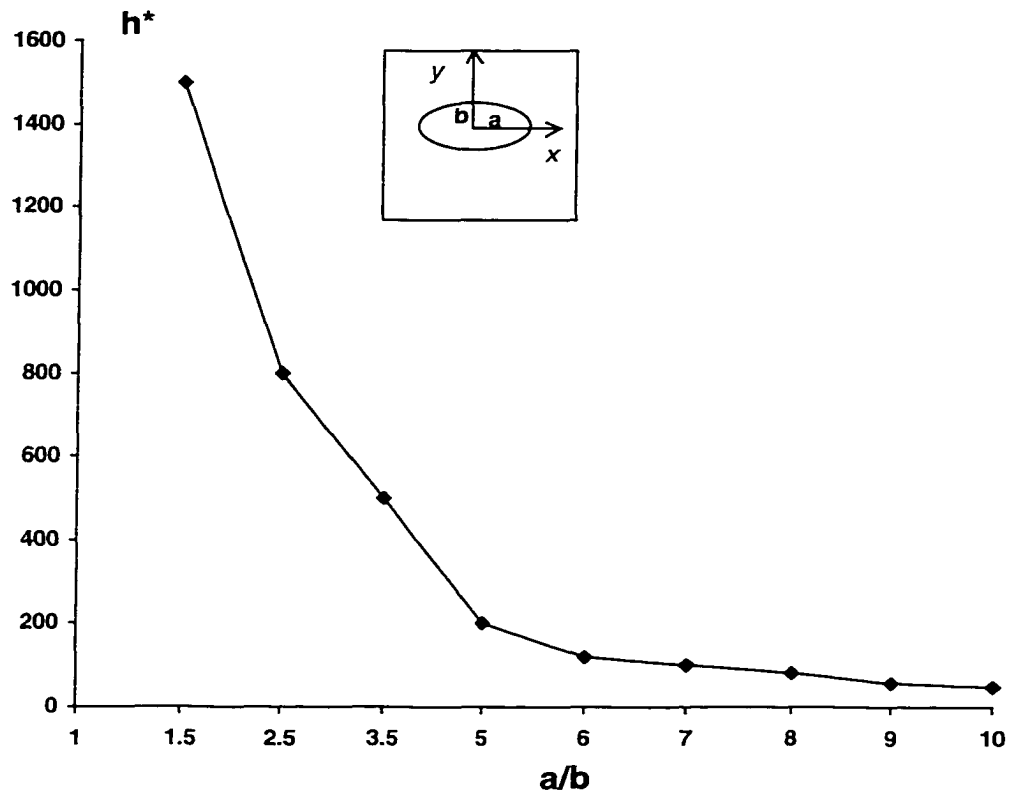


Figure 4.29: The relationship between h^* and a/b for von_Mises' stress criterion

Since h^R is rendered dimensionless by division by μ_l/b and represents a critical value in reducing the thermal stress, for a specific aspect ratio, we could decrease the value of h^R by reducing the shear moduli of the interphase layer (very soft), and adjusting the thickness of the interphase layer. The relationship between the parameter h^R and the aspect ratio a/b is given in Figures 4.30,4.31.

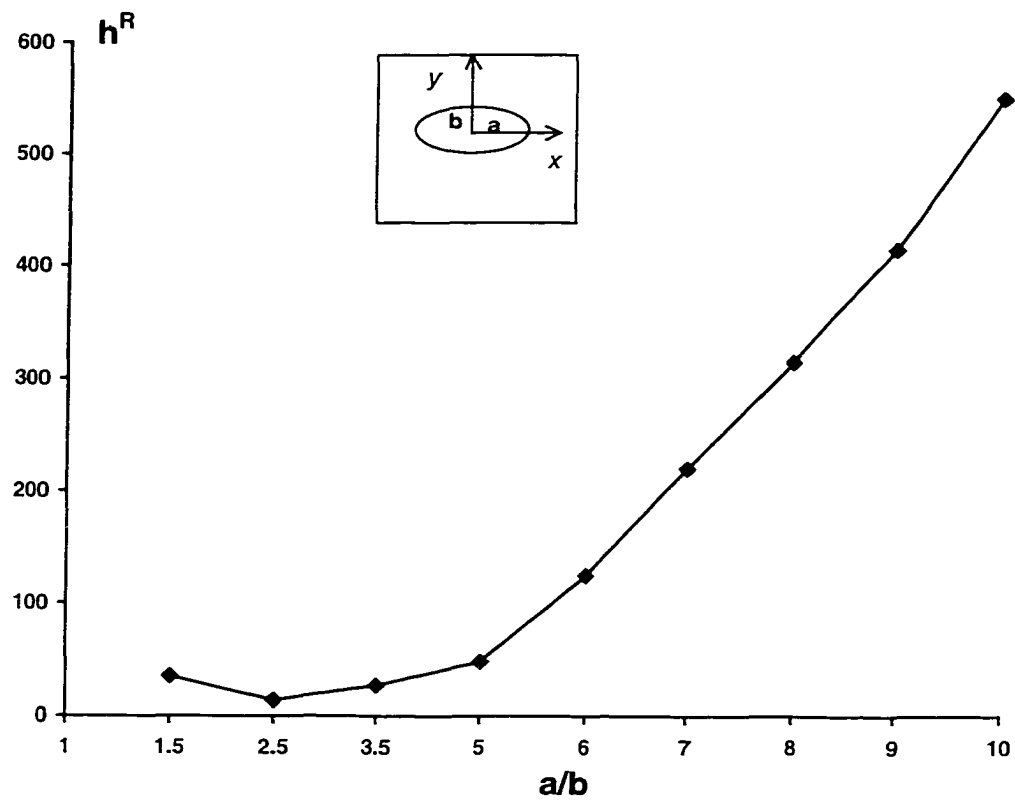


Figure 4.30: The relationship between h^R and a/b for the mean stress' criterion

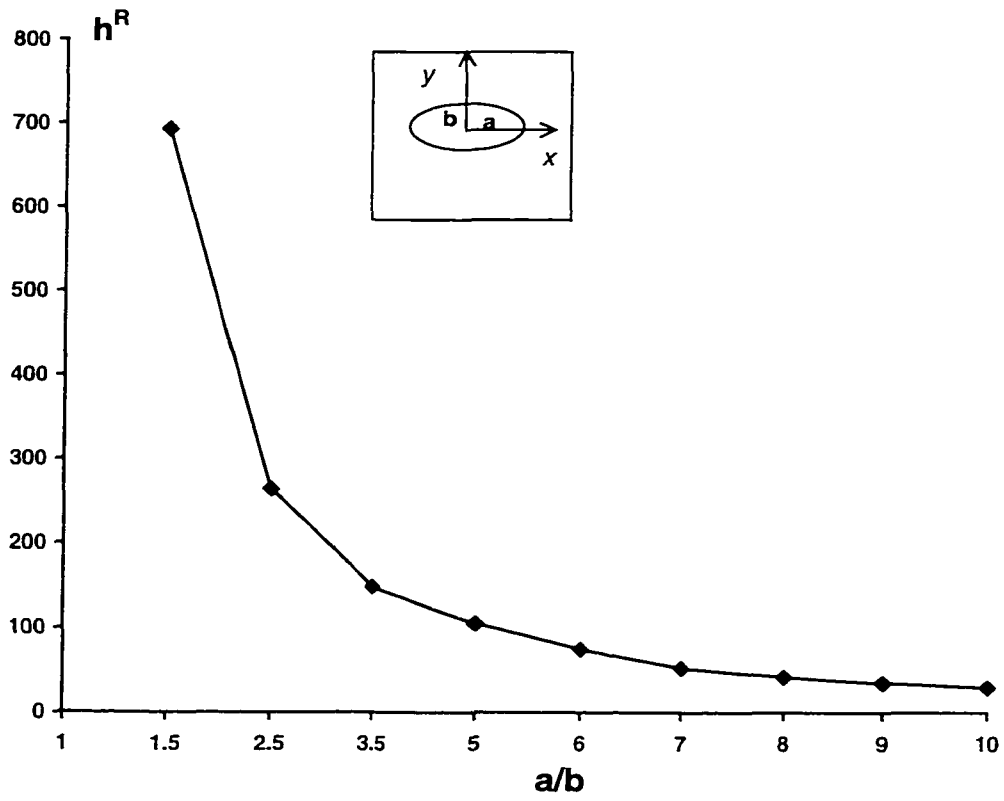


Figure 4.31: The relationship between h^R and a/b for von_Mises' stress criterion

4.3.4 Average Stress Inside Inclusion

As a comparison, Figures 4.32 and 4.33 plot the effect of the interphase layer on the average stress (defined in Eq.(2.25)) inside the inclusion in plane strain under a uniform change in temperature. It is indicated that the average stresses are increasing with parameter h for different aspect ratios a/b . This is in a strong contrast to peak mean stress and von Mises stress which have been found not to increase with h (see Figures 4.24, 4.25). In addition, for all cases, our results indicate that the average stresses inside the inclusion are monotonic functions of the imperfect interface parameter h .

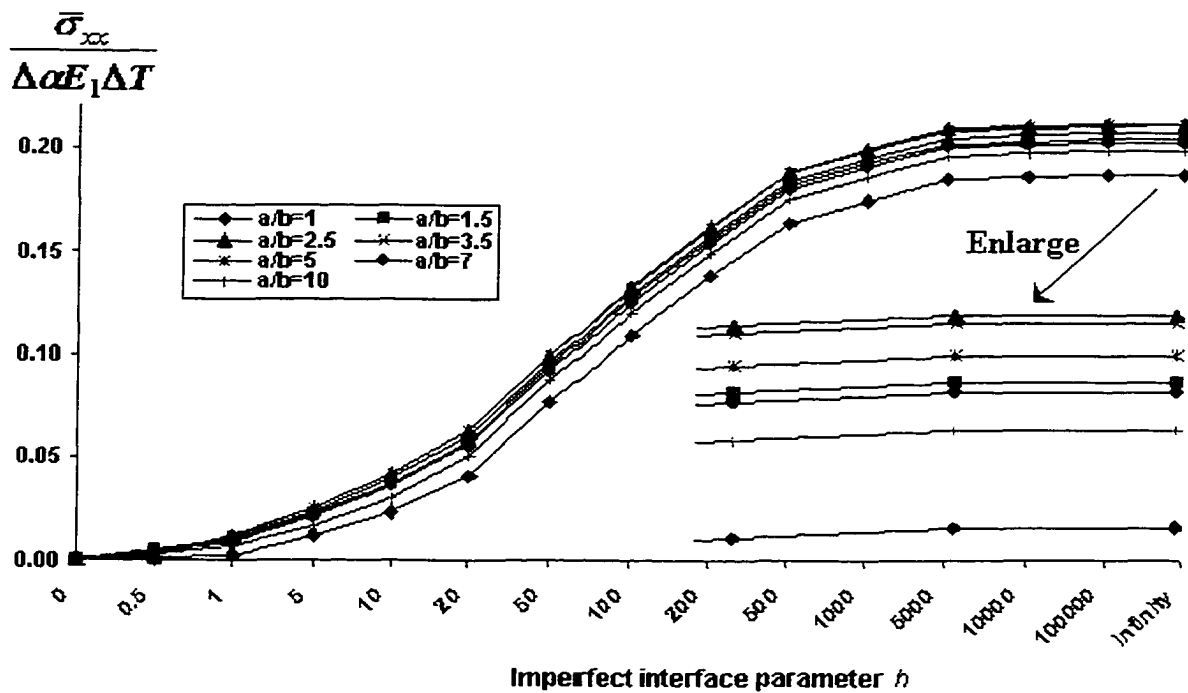


Figure 4.32: Effect of the imperfect interface parameter h on the average stress

$(\frac{\bar{\sigma}_{xx}}{\Delta\alpha E_1 \Delta T})$ inside inclusion in plane strain under a uniform change in temperature

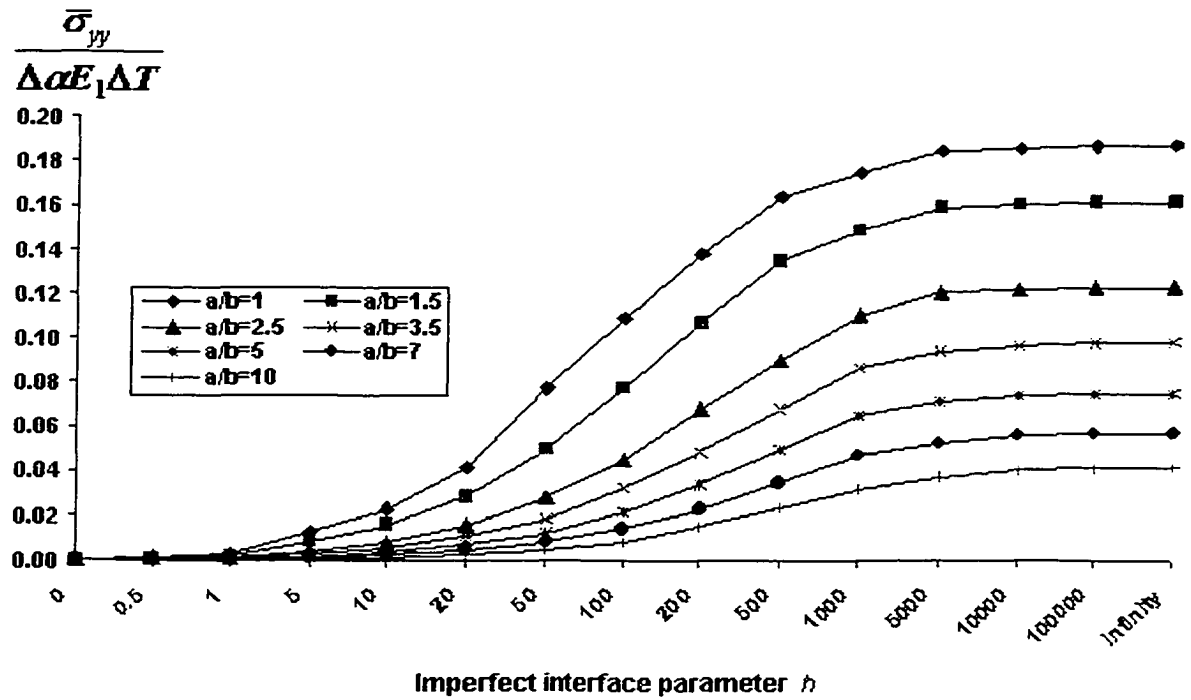


Figure 4.33: Effect of the imperfect interface parameter h on the average stress

$(\frac{\bar{\sigma}_{yy}}{\Delta\alpha E_1 \Delta T})$ inside inclusion in plane strain under a uniform change in temperature

4.4 SUMMARY OF RESULTS OBTAINED

This chapter presents a study of the effects of a compliant interphase layer and the aspect ratio on the thermal mismatch induced residual internal stresses inside an elliptic inclusion embedded within an elastic matrix subjected to a uniform change in temperature. Numerical computations and analysis of the subsequent results have led to the following conclusions:

1. The compliant interphase layer has a significant effect on the thermal stress distribution along the interface and the internal thermal stresses. In particular, it has been shown that the effect of the interphase layer (described by the interface parameter h) on the peak traction and peak interfacial strain energy density is particularly significant for an elliptic inclusion with relatively small aspect ratio (≤ 5), but not for larger values of a/b .
2. Our numerical results show the peak interfacial traction and peak interfacial strain energy density are non-monotonic functions of the interface parameter(h) describing the compliant interphase layer. Consequently, for different aspect ratios, we have identified a unique finite value h^* of the parameter $h(\neq 0, \infty)$ which corresponds to maximum peak traction or maximum peak interfacial strain energy density along the interface. Hence, since the parameter h is determined by the properties and thickness of the adhesive layer between the elliptic inclusion and the matrix, it is possible to control the debonding and failure of the interface by designing the value h for a given aspect ratio. This means that, for a specific aspect ratio, it is possible to minimize peak interfacial stress by adjusting the mechanical properties or thickness of the adhesive layer.
3. It has been indicated that the normal stresses are always positive along the entire interface. Therefore, any possible overlapping associated with the imperfect interface model used in this chapter cannot occur in the present problem. This result shows that the imperfect interface model is particularly suitable for thermal stress analysis of elastic inclusions with a compliant interphase layer.

4. The present computations also indicate that there is no significant difference between the cases $h_1=h_2$ and $h_1=3h_2$. This is due to the fact that the interfacial stresses caused by thermal contraction of the inclusion are dominated by the normal component so that the tangential interface parameter h_2 plays an insignificant role.
5. Our numerical results show the peak mean stress and peak von Mises equivalent stress are both non-monotonic functions of the parameter h . This allows us to find a finite value h^* of the parameter h ($\neq 0, \infty$) which corresponds to the maximum peak mean stress or the maximum peak von Mises equivalent stress. Consequently, it is possible to predict and control the debonding and failure of the interface by identifying the value h^* which depends on the aspect ratio of the ellipse and the properties and thickness of the adhesive layer between the inclusion and the matrix. This is a direct consequence of the fact that values of h^* correspond to maximum peak stress along the interface. Furthermore, we have shown that, for a specific aspect ratio, it is possible to reduce peak thermal stresses by adjusting the mechanical properties and thickness of the adhesive layer. We have also obtained another value h^R of h below which the peak (mean or von Mises) stress within the inclusion is smaller than that corresponding to a perfect interface. By designing the interphase layer so that h is close to unity, we may reduce the peak internal thermal stress to a fraction of its original value obtained in the absence of the interphase layer.
6. For an elliptic inclusion with moderate aspect ratio, a reasonably thick interphase layer (for example, a thickness of about 1/5 the size of the inclusion) can reduce the thermal stress to a fraction of its original value (perfect bonding) if the interphase layer is much more compliant than the matrix. However, the peak stresses in the

presence of an interphase layer could be even bigger than those obtained in the corresponding case of perfect bonding if the interphase layer is not sufficiently compliant and/or not sufficiently thick. In other words, inserting a compliant interphase layer will not unconditionally reduce the peak thermal stress within the inclusion.

7. Our computations indicate that the mean stress is a non-monotonic function of the aspect ratio a/b , while the von Mises stress is a monotonic function of the aspect ratio a/b . These results also show that the effect of the interphase layer on the mean stress is sensitive to small aspect ratios (<5) of the elliptic inclusion. For the cases discussed in this chapter, the mean stress and von Mises equivalent stress give different values of h^* . Thus we have a choice of two different failure criteria to characterize the internal failure of the inclusion.

CHAPTER 5

CONCLUSIONS AND SUGGESTIONS FOR FUTURE STUDY

In this dissertation, the problems of an elliptic inclusion with an imperfect interface, representing an interphase layer, subjected to several different types of loading are studied using a spring-type interface model. Such a spring-type interface model allows displacement discontinuities across the inclusion/matrix interface. By using complex variable techniques, we obtain infinite series representations of the stresses which, when evaluated numerically, demonstrate how the stress field inside the inclusion varies with the aspect ratio of the ellipse and parameters describing the imperfect interface.

In the present study, the interphase is modeled by a distribution of mechanical springs. The constants h (for anti-plane), h_1 and h_2 (for plane deformations) are the coefficients of these springs. Within this approach the composite is modeled as a two-phase material with imperfect interfacial conditions applied along the interface between the single inclusion and its surrounding matrix. The single-cell model adopted in the analysis is a much simpler model than other available multi-cell composite models commonly used by others. This model, as discussed in Schmauder et al, 1992, is suitable for modeling composites with fiber volume fractions up to 40%. Under this condition, the

interaction among neighboring fibers and its influence on the stress fields of the overall composite system can be neglected. Therefore a single fiber model should describe the stress and displacement fields inside and around the inclusion reliably for low or medium fiber volume content composites.

In Hill 1961,1972, Hill indicated that the possible displacement discontinuities across the inclusion/matrix interface are governed by the local rather than by the global material properties of the composite. Under the present model, this conclusion still holds. The analyses presented in this dissertation are for anti-plane and planar elastic systems. Though the last two problems discussed are formulated under the plane strain conditions, plane stress solutions for the same problems can be readily found by adjusting the material constants of the composite (Timoshenko,1970).

As shown in this study, it is straightforward to use the spring-type interface model to simulate the complex behavior of the interface. It is, however, rather difficult to physically measure these parameters. Certain techniques have been proposed to characterize these interactions (Narkis et al,1988), but further studies are needed to gain a better understanding of interfacial bonding so that the interfacial bonding stiffness defined in this study can be correlated to measurable interphase material properties. The focus of this study is based upon the mathematical merit of such interface parameters rather than their physical characteristics.

In addition, all the solutions discussed in this dissertation are based on the single inclusion model. For large fiber volume fraction composites, the solutions are less reliable and other modeling techniques such as the periodically spaced hexagonal array model proposed by Achenbach and Zhu,1990, may be considered. It should also be noted

that interfacial decohesion is assumed to occur within the elastic regime without taking into account any plastic deformation.

The understanding of the localized elastic field of a composite provides the necessary vehicle for calculating its effective properties. Such methods as proposed in Chuistensen and Lo,1979; Hashin,1990; Jun and Jasiuk,1993, may be applied in this regard. The exact evaluation of the effective elastic properties of composites will help to improve the design of such structures. Since in this dissertation we are interested in the local elastic field of the composite, the calculation of the effective (global) properties are not included in the framework of this research.

It was noted in Section 3.3.1 of Chapter 3 that a possible negative normal displacement jump is an issue of major concern for the present imperfect interface model. There are two different methods available to address this issue. The first one is to modify the imperfect interface model by assuming the continuity of normal displacement at all points where a compressive normal traction occurs (Achenbach & Zhu,1989,1990). The second one tolerates a limited negative normal displacement jump bounded by the original thickness of the interphase layer (Hashin, 1991b). As explained in Section 3.3.1 of Chapter 3, the interphase layer can sustain a tensile normal traction as well as a compressive normal traction. Consequently, a negative normal displacement jump is acceptable provided it is smaller than the original interphase thickness. It is readily seen that the negative normal displacement jump appearing in all figures of the present research is sufficiently small and therefore acceptable.

In summary, the problems of an elliptic inclusion embedded in an infinite matrix with a homogeneously imperfect interface subjected to mechanical and thermal loading

are studied. A spring-type imperfect interface model is proposed. Complex variable techniques are used to obtain infinite series representations of the stresses which, when evaluated numerically, demonstrate how the stress field inside the inclusion varies with the aspect ratio of the ellipse and parameters describing the imperfect interface. For the first time, we investigate systematically the role of the imperfect interface parameters on the stress field and average stress. Numerical results are presented to show the validity of the analyses along with a discussion of the implication of the localized elastic field to the possible failure mechanism of the composite. The following observations can be drawn from the numerical examples studied in this research:

- The interface imperfection has a significant effect on stress fields in and near the inclusion (along the interface). The non-uniformity of stress is closely related to the interface parameter describing the imperfection and the aspect ratio of the ellipse. It has also been indicated that the definition of the imperfect interface and the physical explanation of the interface parameters used in Hashin (1991b) are indeed suitable for describing the nature of the interface. Consequently, using only average stress is insufficient to describe the debonding and failure of the material interface since both are controlled by interfacial stresses which are themselves closely related to the imperfect interface parameter and the aspect ratio of the ellipse.
- It is possible to predict and control the debonding and failure of the interface by identifying a distinct value (h^*) of the interface parameter which depends on the aspect ratio of the ellipse and the properties and thickness of the adhesive layer between the elliptic inclusion and the matrix. This is a direct consequence of the fact that values of h^* correspond to maximum peak stress (including mean and von Mises

stress) along the interface. Furthermore, we have shown that, for a specific aspect ratio, it is possible to avoid or minimize peak stress by adjusting mechanical properties and the thickness of the interphase layer.

- For plane deformation, the peak interfacial traction and peak strain energy density have been found to be non-monotonic functions of the imperfect interface parameter h . Consequently, for different aspect ratios, we have found a unique finite value h^* of the parameter $h(\neq 0, \infty)$ which corresponds to maximum peak traction or maximum peak strain energy density along the interface. Hence, since the parameter h characterizes the properties and thickness of the adhesive layer between the elliptic inclusion and the matrix, it is possible to predict and control the debonding and failure of the interface by identifying the value h^* for a given aspect ratio. In addition, this means that, for a specific aspect ratio, it is possible to minimize peak interfacial stress by adjusting the mechanical properties and thickness of the adhesive layer.
- In the case of mechanical loading (Chapter 3), the magnitudes and ranges of the negative normal stresses are very small, thus any possible overlapping associated with the imperfect interface model used in this chapter can be considered to be reasonable (interphase has a thickness).
- In the case of thermal loading (Chapter 4), the normal stresses are always positive along the entire interface. Therefore, any possible overlapping associated with the imperfect interface model used in this chapter cannot occur. This result shows that the imperfect interface model is particularly suitable for thermal stress analysis of elastic inclusions with a compliant interphase layer.

- In the case of thermal loading (Chapter 4), we also obtain another value h^R of h below which the peak (mean or von Mises) stress within the inclusion is smaller than that corresponding to a perfect interface. By designing the interphase layer so that h is close to unity, we may reduce the peak internal thermal stress to a fraction of its original value obtained in the absence of the interphase layer. However, the peak stresses in the presence of an interphase layer could be even bigger than those obtained in the corresponding case of perfect bonding if the interphase layer is not sufficiently compliant and/or not sufficiently thick. In other words, inserting a compliant interphase layer will not unconditionally reduce the peak thermal stress within the inclusion.

REFERENCES

- Aboudi, J., 1987, Damage in Composites-Modeling of Imperfect Bonding.
Composites Science and Technology, Vol.28, pp. 103-128.
- Achenbach, J.D. and Zhu, H., 1989, Effect of Interfacial Zone on Mechanical Behavior and Failure of Fiber-reinforced Composites. *Journal of The Mechanics and Physics of Solids*, Vol.37, pp. 381-393.
- Achenbach, J.D. and Zhu, H., 1990, Effect of Interphases on Micro and Macromechanical Behavior of Hexagonal-Array Fiber Composites. *ASME Journal of Applied Mechanics*, Vol.57, pp.956-963.
- Achenbach, J.D. and Choi, H., 1991, Matrix Cracking and Interphase Failure in Fiber Composites. *Local Mechanics Concepts for Composite Material Systems*, J.N. Reddy and K.L. Reifsnider Eds., pp. 149-163, Springer-Verlag, New York.
- Agarwal, B.D and Bansal, R.K., 1979, Effect of an Interfacial Layer on the Properties of Composites. *Fiber Science and Technology*, Vol.12, pp.149-158.
- Benveniste, Y., 1984, On the Effect of Bonding on the Overall Behavior of Composite Materials. *Mechanics of Materials*, Vol. 3, pp. 349-358.
- Benveniste, Y., 1985, The Effective Mechanical Behavior of Composite Materials with Imperfect Contact Between Constituents. *Mechanics of Materials*, Vol.4, pp. 197-208.
- Benveniste, Y. and Miloh, T., 1986, The Effective Conductivity of Composites with Imperfect Thermal Contact at Constituent Interfaces. *International Journal of*

- Engineering Science*, Vol.24, pp. 1537-1552.
- Benveniste, Y., Dvorak, G.J. and Chen, T., 1989, Stress Fields in Composites with Coated Inclusions. *Mechanics of Materials*, Vol.7, pp. 305-317.
- Besser, P.R., Brennan, S. and Bravman, J.C., 1994, An X-Ray Method for Direct Determination of the Strain State and Strain Relaxation in Micron-Scale Passivated Metallization Lines During Thermal Cycling. *J. Mater. Res.* 9, pp.13-24.
- Brennan, J.J., 1988, Interfacial Chemistry and Bonding in Fiber Reinforced Glass and Glass-Ceramic Matrix Composites. *Ceramic Microstructures and Role of Interface*, J.A. Pask and A.G. Evans Eds., pp.387-399, Plenum Press, New York.
- Chulistensen, R.M. and Lo, N.H., 1979, Solutions for Effective Shear Properties in Three Phase Sphere and Cylinder Models. *Journal of The Mechanics and Physics of Solids*, Vol.27, pp. 315-330.
- Dasgupta, A. and Sirkis, J.S., 1992, Importance of Coatings to Optical Fiber Sensors Embedded in Smart Structures. *AIAA Journal*, Vol.30, pp.1337-1343.
- Dhingra, A.K. and Fishman, S.G., 1986, *Interfaces in Metal-Matrix Composites*, The Metallurgical Society, Inc., Cleveland, Ohio.
- Dokos, S.J., 1949, A Force Applied in the Median Plane at the Center of a Circular Insert in a Plate. *ASME Journal of Applied Mechanics*, Vol.19, pp.411-413.
- Dowling , Norman, E.,1993, *Mechanical Behavior of Materials: Engineering Methods for Deformation, Fracture, and Fatigue*. Prentice-Hall, Inc.
- Dundurs, J. and Zienkiewicz, O.C., 1964, Stresses Around Circular Inclusions Due to Thermal Gradients with Particular Reference to Reinforced Concrete. *Journal of The American Concrete Institute*, pp. 1523-1533.

- Dundurs, J., 1989, Cavities vis-a-vis Rigid Inclusions and Some Related General Results in Plane Elasticity. *ASME Journal of Applied Mechanics*, Vol.56, pp.786-790.
- England, A. H.,1971, *Complex variable methods in elasticity*. London:Wiley-Interscience.
- Eshelby,J. D., 1957,The Determination of the Elastic Field of an Ellipsoidal Inclusion and Related Problems. *Proc. R. Soc. London. A*, 241, pp.376-396.
- Eshelby, J. D., 1959, The Elastic Field Outside an Ellipsoidal Inclusion. *Proc. R. Soc. London. A*, **252**, pp.561-569.
- Evans, A.G. and Hutchinson, J.W., 1995, The Thermomechanical Integrity of Thin Films and Multilayers. *Acta Metall. Mater.* 43,pp.2507-2530.
- Evans, J. Y. and Evans. J. W.,1991, Electronic Materials and Properties, *Handbook of Electronic Package Design*. M. Pecht, ed. Marcel Dekker, New York.
- Gao, J., 1995, A Circular Inclusion with Imperfect Interface: Eshelby's Tensor and Related Problems. *ASME Journal of Applied Mechanics*, Vol. 62, pp.860-866.
- Gleixner, R. J., Clements, B. M. and Nix, W. D., 1997, Void Nucleation in Passivated Interconnect Lines: Effect of Site Geometries, Interfaces, and Interface Flaws. *J. Mater. Res.* 12(8), pp.2081-2090.
- Gong, S.X. and Meguid, S.A., 1993, On the Elastic Fields of an Elliptical Inhomogeneity Under Plane Deformation. *Proc. R. Soc. London.A*, 443, pp.457-471.
- Gouldstone, A., Shen, Y-L, Suresh, S. and Thompson, C. V., 1998, Evolution of Stress in Passivated and Unpassivated Metal Interconnects. *J. Mater. Res.* 13(7), pp.1956-1966.

- Hashin, Z., 1983, Analysis of Composite Materials- A Survey. *ASME Journal of Applied Mechanics*, Vol.50, pp.481-505.
- Hashin, Z., 1990, Thermoelastic Properties of Fiber Composites with Imperfect Interface. *Mechanics of Materials*, Vol.8, pp.333-348.
- Hashin, Z., 1991a, Thermoelastic Properties of Particulate Composites with Imperfect Interface. *J. Mech. Phys. Solids* 39, pp.745-762.
- Hashin, Z., 1991b, The Spherical Inclusion with Imperfect Interface. *J. Appl. Mech.* 58, pp.444-449.
- Hashin, Z., 1992, Extremum Principles for Elastic Heterogeneous Media with Imperfect Interfaces and Their Application to Bounding of Effective Moduli. *J. Mech. Phys. Solids* 40, pp.767-781.
- Hill, R., 1961, Discontinuity Relation in Mechanics of Solids. *Progress in Solid Mechanics*, Vol.2, Chapter VI, North Holland Publishing Co., Amsterdam, Netherlands.
- Hill, R., 1972, An Invariant Treatment of Interfacial Discontinuities. *Continuum Mechanics and Related Problems of Analysis*, pp.594-604, Moscow.
- Honein, T. and Herrmann, C., 1990, On Bonded Inclusions with Circular or Straight Boundaries in Plane Elastostatics. *ASME Journal of Applied Mechanics*, Vol.57, pp. 850-856.
- Horgan, C. O., 1995, Anti-Plane Shear Deformations in Linear and Nonlinear Solid Mechanics. *SIAM REVIEW*, Vol. 37, No. 1, pp. 53-81.
- Hu, S. M., 1991, Stress-Related Problems in Silicon Technology. *J. Appl. Phys.* 70, R53-R80.

- Huang, Y., Hu, K. X., 1995, A Generalized Self-Consistent Mechanics Method for Solids Containing Elliptical Inclusion. *J. Appl. Mech.* **62**, pp.566-572.
- Jasiuk, I., Chen, J. and Thorpe, M.F., 1992, Elastic Moduli of Composites with Rigid Sliding Inclusions. *Journal of The Mechanics and Physics of Solids*, Vol.40, No.2, pp.373-391.
- Jasiuk, I. and Tong, Y., 1989, The Effect of Interface on the Elastic Stiffness of Composites. *Mechanics of Composite Materials and Structures*, J.N.Reddy et al. ed., ASME AMD-Vol. 100, pp.49-54.
- Jasiuk, I. and Kouider, M. W., 1993, The Effect of an Inhomogeneous Interphase on the Elastic Constants of Transversely Isotropic Composites. *Mech. Mater.* 15, pp.53-63.
- Jayaraman, K., Gao, Z. and Reifsnider, K.L., 1992, The Interphase in Unidirectional Fiber-Reinforced Epoxies: Effects on Local Stress Fields. *Journal of Composite Technology and Research*, Vol.16, No.1, pp.21-31.
- Jayaraman, K. and Reifsnider, K.L., 1991, Stress Fields in Continuous Fiber Composites with Interphasial Property Gradients. *Interfaces*, Vol. 10, pp.759-768.
- Jayaraman, K., Reifsnider, K.t. and Swain, R.E., 1993a, Elastic and Thermal Effects in the interphases: Part I. Comments on Characterization Methods. *Journal of Composite Technology and Research*, Vol.15, No.1, pp.3-13.
- Jayaraman, K., Reifsnider, K.L. and Swain, R.E., 1993b, Elastic and Thermal Effects in the interphases: Part II. Comments on Modeling Studies. *Journal of Composite Technology and Research*, Vol.15, No.1, pp.14-22.
- Jones, J.P. and Whittier, J.S., 1967, Waves at a Flexibly Bonded Interface. ASME *Journal of Applied Mechanics*, Vol.34, pp.905-909.

- Jun, S. and Jasiuk, I., 1993, Elastic Moduli of Two-Dimensional Composites with Sliding Inclusions-A Comparison of Effective Medium Theories. *International Journal Solids and Structures*, Vol.30, No.18, pp.2501-2523.
- Keer, L.M., Dundurs, J. and Kiattikomol, K., 1973, Separation of a Smooth Circular Inclusion From a Matrix. *International Journal of Engineering Science*, Vol.11, pp.1221-1233.
- Kim, J.O. and Bau, H.H., 1992, A Study of the Fiber-Matrix Interface in Composite Materials. *ASME Journal of Applied Mechanics*, Vol.59, pp. S163-S165.
- Korhonen, M.A., Paszkiet, C.A. and Li, C.Y., 1991, Mechanisms of Thermal Stress Relaxation and Stress-Induced Voiding in Narrow Aluminum-Based Metallizations. *J. Appl. Phys.* 69, pp.8083-8091.
- Kouris, D.A. and Mura, T., 1989, The Elastic Field of a Hemispherical Inhomogeneity at the Free Surface of an Elastic Half Space. *Journal of The Mechanics and Physics of Solids*, Vol.37, pp.365-379.
- Kouris, D. and Tsuchida, E., 1992, An Analytical Solution for the Fiber Indentation Problem. *European Journal of Mechanics and Solids*, Vol.11, No.3, pp.323-334.
- Lee, Y.D. and Erdogan, F., 1995, Residual/thermal Stresses in FGM and Laminated Thermal Barrier Coatings. *Int. J. Fract.* 69, pp.145-165.
- Lerch, B.A., Hull, D.R. and Leonhardt, T.A., 1990, Microstructure of a SiC/Ti-15-3 Composite. *Composites*, Vol.21, pp.216-224.
- Levy, A.J., 1991, The Debonding of Elastic Inclusions and Inhomogeneities. *Journal of The Mechanics and Physics of Solids*, Vol.39, No. 4, pp.477-505.

- Lu, I-Ping, 1993, On Interfaces and Interphases in Modeling Optical Fiber Sensors Embedded in Graphite/Epoxy Systems. M.S. Thesis, University of Maryland at College Park, College Park, MD.
- Mal, A.N. and Bose, S.K., 1975, Dynamic Elastic Moduli of a Suspension of Imperfectly Bonded Spheres. *Proceedings of The Cambridge Philosophical Society*, Vol.76, pp.587-600.
- Mikata, Y. and Taya, M., 1985, Stress Field in a Coated Continuous Fiber Composite Subjected to Thermo-mechanical Loadings. *Journal of Composite Materials*, Vol.19, pp.554-578.
- Muskhelishvili, N. I., 1963, *Some basic problems of the mathematical theory of elasticity*. Groningen: Noodhoff.
- Narkis, M., Chen, E.J.H. and Pipes, R.B., 1988, Review of Methods for Characterization of Interfacial Fiber-Matrix Interaction. *Polymer Composites*, Vol.9, pp.245-251.
- Needlerman A., 1990, An Analysis of Decohesion Along an Imperfect Interface. *International Journal of Fracture*, Vol.42, pp.21-40.
- Niwa., H., Yagi, H. and Tsuchikawa, H., 1990, Stress Distribution in an Aluminum Interconnect of Very Large Scale Integration. *J. Appl. Phys.* 68, pp.328-333.
- Noble, B. and Hussain, M.A., 1969, Exact Solution of Certain Dual Series for Indentation and Inclusion Problems. *International Journal of Engineering Science*, Vol.7, pp. 1149-1161.
- Osiroff, R. and Hasselman, D.P.H., 1991, Effect of Interfacial Thermal Barrier on the Thermal Stresses Near Spherical Inclusion in Matrix Subjected to Linear Heat Flow. *Journal of Composite Materials*, Vol.25, pp.1589-1598.

- Pagano, N.J. and Tandon, G.P., 1990, Modeling of Imperfect Bonding in Fiber Reinforced Brittle Matrix Composites. *Mechanics of Materials*, Vol. 9, pp. 49-64.
- Pottinger, M., Coburn, J. and Edman, I., 1994, *Journal of Polymer Science-Part B, Polymer Physics* 32(5).
- Qu, J., 1993a, Eshelby Tensor for an Elastic Inclusion with Slightly Weakened Interface. *J. Appl. Mech.* 60, pp.1048-1050.
- Qu, J., 1993b, The Effect of Slightly Weakened Interface on the Overall Elastic Properties of Composite Materials. *Mech. Mater.* 14, pp.269-281.
- Ru, C. Q. & Schiavone, P., 1996, On the Elliptic Inclusion in Anti-Plane Shear. *Math. Mech. Solids* 1, pp.327-333.
- Ru, C. Q. & Schiavone, P., 1997, A Circular Inclusion with Circumferentially Inhomogeneous Interface in Anti-Plane Shear. *Proc. R. Soc. London A*, 453, pp.2551-2572.
- Ru, C. Q., 1998a, Effect of Interphase Layers on Thermal Stresses within an Elliptical Inclusion. *J. Appl. Phys.* 84, pp.4872-4879.
- Ru, C. Q., 1998b, A Circular Inclusion with Circumferentially Inhomogeneous Sliding Interface in Plane Elastostatics. *J. Appl. Mech.* 65, pp.30-38.
- Ru, C. Q., Schiavone, P. and Mioduchowski, A., 1999, Uniformity of Stresses within a Three-Phase Elliptic Inclusion in Anti-Plane Shear. *Journal of Elasticity* 52, pp.121-128.
- Schmauder, S., Muller, W.H. and McMeeking, R.M., 1992, Residual Stresses at Interfaces in Fiber Reinforced Composites. *Residual Stresses-III* Science and

Technology, H. Fujiwara, T. Abe and K. Tanaka Eds., pp. 589-594, Elsevier Applied Science, London.

- Shen, H., Schiavone, P, Ru, C. Q. & Mioduchowski, A., 1999a, An Elliptic Inclusion with Imperfect Interface in Anti-Plane Shear. *International Journal of Solids and Structures*. (Accepted for publication).
- Shen, H., Schiavone, P, Ru, C. Q. & Mioduchowski, A., 1999b, Stress Analysis of an Elliptic Inclusion with Imperfect Interface in Plane Elasticity. (Submitted).
- Shen, H., Schiavone, P, Ru, C. Q. & Mioduchowski, A., 1999c, Interfacial Thermal Stress Analysis of an Elliptic Inclusion with a Compliant Interphase Layer in Plane Elasticity. (Submitted).
- Shen, H., Schiavone, P., Ru, C. Q. and Mioduchowski, A., 1999d, Analysis of Internal Stress in an Elliptic Inclusion with Imperfect Interface in Plane Elasticity. *Mathematics and Mechanics of Solids*. (Accepted for publication).
- Shen, H., Schiavone, P, Ru, C. Q. & Mioduchowski, A. 1999e, Effects of a Compliant Interphase Layer on Thermal Stresses within an Elliptic Inhomogeneity in an Elastic Medium. *Journal of Applied Mathematics and Physics (ZAMP)*(Accepted for publication).
- Shen, H., Schiavone, P, Ru, C. Q. & Mioduchowski, A., On the Approximate Solution of an Elliptic Inclusion with Imperfect Interface in Anti-Plane Shear, *The 17th Canadian Congress of Applied Mechanics*, Hamilton, Canada, May 30 - June 3, 1999.
- Shen, H., Schiavone, P, Ru, C. Q. & Mioduchowski, A., Stress Analysis of an Elliptic Inclusion with Imperfect Interface Embedded in an Infinite Elastic Medium, 6th

International Conference of IMSE, Banff, Alberta, Canada, 12-15 June 2000.

- Shen, Y-L., 1998, Stresses, Deformation, and Void Nucleation in Locally Debonded Metal Interconnects. *J. Appl. Phys.* 84, pp.5525-5530.
- Shull, A.L. and Spaepen, F., 1996, Measurements of Stress During Vapor Deposition of Copper and Silver Thin Films and Multilayers. *J. Appl. Phys.* 80, pp.6243-6256.
- Sottos, N.R., McCullough, R.L. and Scott, W.R., 1992, The Influence of Interphase Regions on Local Thermal Displacements in Composites. *Composites Science and Technology*, Vol.44, pp.319-322.
- Spaepen, F. and Shull, A.L., 1996, *Current Opinion in Solid State & Materials Science* 1, 678.
- Stagni, L. 1991, Elastic Field Perturbation by an Elliptic Inhomogeneity with a Sliding Interface. *Journal of Applied Mathematics and Physics (ZAMP)* Vol. 42, pp. 811-819.
- Sudak, L. J., Ru, C. Q., Schiavone, P. and Mioduchowski, A., 1999, A Circular Inclusion with Inhomogeneously Imperfect Interface in Plane Elasticity. *J. of Elasticity*, Vol. 55, pp. 19-41
- Theocaris, P.S. and Phillippidis, T.P., 1985, Theoretical Evaluation of the Extent of the Mesophase in Particulate and Fibrous Composites. *Journal of Reinforced Plastics Composites*, Vol.4, pp.173-185.
- Thompson, C.V. and Carel, R., 1996, Stress and Grain Growth in Thin Films. *J. Mech. Phys. Solids.* 44, pp.657-673.
- Thouless, M.D., Gupta, J. and Harper, J.M.E., 1996, Stress Development and Relaxation in Copper Films During Thermal Cycling. *J. Mater. Res.* 8, pp.1845-1852.

- Timoshenko, S.P. and Goodier, J.N., 1970, *Theory of Elasticity*, 3rd Ed., McGraw-Hill Book Co., New York.
- Vaidyanathan, S. and Kouris, D., 1992, Effects of an Elliptical Inhomogeneous Inclusion with a Slipping Interface on the Elastic Field of a Concentrated Moment. *ASME Journal of Applied Mechanics*, Vol.59, pp.780-782.
- Venkatraman, R., Bravman J.C., Nix, W.D. and Davies, P.W., 1990, Mechanical Properties and Microstructural Characterization of Al-0.5%Cu Thin Films. *J. Electronic Mater.* 19, pp.1231-1237.
- Walpole, T.J., 1978, A Coated Inclusion in an Elastic Medium. *Proceedings of The Cambridge Philosophical Society*, Vol.83, pp.495-506.
- Wheeler, L.T., 1996, Maximum principles in classical elasticity in *Mathematical problems in elasticity*, pp.157-185, edited by Remigio Russo. World Scientific Publishing Co Pte Ltd.
- Wikström, A., Gudmundson, P. and Suresh, S., 1999, Thermoelastic Analysis of Periodic Thin Lines Deposited on a Substrate. *J. Mech. Phys. Solids*. 47, pp.1113-1130.
- Williamson, R.L., Rabin, B.H. and Drake, J.T., 1993, Finite Element Analysis of Thermal Residual Stresses at Graded Ceramic-Metal Interfaces.Part I. Model Description and Geometrical Effects. *J. Appl. Phys.* 74, pp.1310-1320.
- Wu, C. C., Kahn, M. and Moy W., 1996, Piezoelectric Ceramics with Functional Gradients:a New Application in Material Design . *J.Am. Ceram. Soc.* 79, pp.809-812.

Yeo, I.-S., Anderson, S. G., Ho, P. S. and Hu, C.K., 1995, Characteristics of Thermal Stresses in Al(Cu) Fine Lines. II. Passivated Line Structures. *J. Appl. Phys.* 78, pp.953-961.

Zielinski, E.M., Vinic, R.P. and Bravman, J.C., 1994, Effects of Barrier Layer and Annealing on Abnormal Grain Growth in Copper Thin Films. *J. Appl. Phys.* 76, pp. 4516-4523.

APPENDIX

INFINITE SERIES REPRESENTATION FOR THE EXPRESSION $\sqrt{1+b^* \sin^2 \theta}$

In order to solve the equation (2.20) in Chapter 2 using infinite series, it is necessary to find a series representation for the expression $\sqrt{1+b^* \sin^2 \theta}$. To this end, note that for any integer k ,

$$\begin{aligned} \int_0^{2\pi} \sqrt{1+b^* \sin^2 \theta} \sin k\theta d\theta &= 0, \\ \int_0^{2\pi} \sqrt{1+b^* \sin^2 \theta} \cos(2k+1)\theta d\theta &= 0. \end{aligned} \tag{A1}$$

Thus,

$$\begin{aligned} \int_0^{2\pi} \sqrt{1+b^* \sin^2 \theta} \cos[2(k+1)\theta] d\theta &= \int_0^{2\pi} \sqrt{1+b^* \sin^2 \theta} [\cos(2k\theta) \cos(2\theta) - \sin(2k\theta) \sin(2\theta)] d\theta = \\ \int_0^{2\pi} \sqrt{1+b^* \sin^2 \theta} \cos(2k\theta) \cos(2\theta) d\theta &+ \frac{4k}{3b^*} \int_0^{2\pi} \sqrt{1+b^* \sin^2 \theta} [1+b^* \sin^2 \theta] \cos(2k\theta) d\theta = \\ \frac{1}{2} \left(1 - \frac{2k}{3}\right) \int_0^{2\pi} \sqrt{1+b^* \sin^2 \theta} [\cos[2(k+1)\theta] + \cos[2(k-1)\theta]] d\theta &+ \frac{2k(2+b^*)}{3b^*} \int_0^{2\pi} \sqrt{1+b^* \sin^2 \theta} \cos(2k\theta) d\theta \end{aligned} \tag{A2}$$

If we define

$$I_{2k} \equiv \frac{1}{2\pi} \int_0^{2\pi} \sqrt{1+b^* \sin^2 \theta} \cos(2k\theta) d\theta \quad (\text{A3})$$

we have $I_{2k} = I_{-2k}$ and

$$\left(\frac{1}{2} + \frac{k}{3}\right) I_{2(k+1)} = \left(\frac{1}{2} - \frac{k}{3}\right) I_{2(k-1)} + \frac{2k(2+b^*)}{3b^*} I_{2k} \quad (\text{A4})$$

Next, writing

$$\sqrt{1+b^* \sin^2 \theta} = \sum_{k=0}^{\infty} I_{2k} (e^{i2k\theta} + e^{-i2k\theta}). \quad (\text{A5})$$

we note that, for large k , the right-hand side of (A5) approaches a geometric series. To find the ratio of this geometric series, let us assume that for large k ,

$$\frac{I_{2(k+1)}}{I_{2k}} = \eta.$$

Also, for large k , Eq. (A4) can be reduced to:

$$I_{2(k+1)} = -I_{2(k-1)} + \frac{2(2+b^*)}{b^*} I_{2k}.$$

Consequently,

$$\eta^2 + 1 - 2\frac{2+b^*}{b^*} \eta = 0 \quad (\text{A6})$$

Noting the expressions for b^* and R^* in Eqs. (7) and (12), we have

$$\eta = \frac{2+b^*}{b^*} - \sqrt{\left(\frac{2+b^*}{b^*}\right)^2 - 1} = \frac{1}{R^{*2}} < 1 \quad (\text{A7})$$

which implies that the geometric series is convergent. We can now rewrite (A5) as:

$$\sqrt{1+b^* \sin^2 \theta} = \sum_{k=0}^{M-1} I_{2k} (e^{i2k\theta} + e^{-i2k\theta}) + \sum_{k=0}^{\infty} I_{2(M+k)} [e^{i2(M+k)\theta} + e^{-i2(M+k)\theta}]$$

and consider the second term on the right-hand side as a geometric series (approximately).

Thus

$$\begin{aligned} \sqrt{1+b^* \sin^2 \theta} &\cong \sum_{k=0}^{M-1} I_{2k} (e^{i2k\theta} + e^{-i2k\theta}) + I_{2M} \left[\frac{e^{i2M\theta}}{1-\eta e^{i2\theta}} + \frac{e^{-i2M\theta}}{1-\eta e^{-i2\theta}} \right] = \\ &\sum_{k=0}^{M-1} I_{2k} (e^{i2k\theta} + e^{-i2k\theta}) + I_{2M} \frac{e^{i2M\theta} + e^{-i2M\theta} - \eta [e^{i2(M-1)\theta} + e^{i2(1-M)\theta}]}{1 + \frac{1}{R^{*4}} - \frac{1}{R^{*2}} (e^{i2\theta} + e^{-i2\theta})} \end{aligned} \quad (\text{A8})$$

The expression (A8) is sufficiently accurate for a given suitably large number M .